NASA CONTRACTOR REPORT 177487

VSAERO Analysis of Tip Planforms for the Free-Tip Rotor

D. M. Martin
P. E. Fortin

CONTRACT NCC 2-175
June 1988

NASA

NASA CONTRACTOR REPORT 177487

VSAERO Analysis of Tip Planforms for the Free-Tip Rotor

D. M. Martin
P. E. Fortin

The University of Kansas Center
for Research, Inc.
Lawrence, Kansas

Prepared for
Ames Research Center
under Contract NCC 2-175
June 1988

National Aeronautics and
Space Administration

Ames Research Center
Moffett Field, California 94035

ABSTRACT

This report presents the results of a numerical analysis of two interacting lifting surfaces separated in the spanwise direction by a narrow gap. The configuration consists of a semispan wing with the last 32% of the span structurally separated from the inboard section. The angle of attack of the outboard section is set independently from that of the inboard section. In the present study, the three-dimensional panel code VSAERO is used to perform the analysis. Computed values of tip surface lift and pitching moment coefficients are correlated with experimental data to determine the proper appraoch to model the gap region between the surfaces. Pitching moment data for various tip planforms are also presented to show how the variation of tip pitching moment with angle of attack may be increased easily in incompressible flow. Calculated three-dimensional characteristics in compressible flow at Mach numbers of 0.5 and 0.7 are presented for new tip planform designs. An analysis of sectional aerodynamic center shift as a function of Mach number is also included for a representative tip planform. It is also shown that the induced drag of the tip surface is reduced for negative incidence angles relative to the inboard section. The results indicate that this local drag reduction overcomes the associated increase in wing induced drag at high wing lift coefficients.

TABLE OF CONTENTS

TABLE OF CONTENTS, continued

LIST OF FIGURES

LIST OF FIGURES, continued

LIST OF FIGURES, continued

LIST OF TABLES

LIST OF SYMBOLS

Symbol	Definition	Units
A	Aspect ratio	
AREA	Panel area	
B_{JK}, C_{JK}	Perturbation velocity potential influence coefficients	
$\bar{c}$	Mean geometric chord	
c_{INB}	Inboard wing chord	
c	Local chord length	
c_{ℓ_a}	Sectional lift due to local angle of attack	
Δc	Distance between tip aerodynamic center and pitch axis	
C_{D_T}	Tip drag coefficient	(tip lift)/qS_t
C_{L_T}	Tip lift coefficient	(tip lift)/qS_t
$(C_{L_\alpha})_T$	Tip lift curve slope	deg^{-1}
C_{m_T}	Tip pitching moment coefficient about the pitch shaft axis (0.25c of inboard section)	(tip pitching moment)/$qS_t\bar{c}$ or (tip pitching moment)/$qS_t c_{INB}$
$C_{m_{ac}}$	Pitching moment coefficient about the aerodynamic center	
C_{D_W}	Semi-span wing drag coefficient	(wing drag)/qS_W
C_{L_W}	Semi-span wing lift coefficient	(wing lift)/qS_W
$(C_{m_\alpha})_T$	Tip pitching moment variation with angle of attack	deg^{-1}
C_ℓ	Sectional lift coefficient	(L)/qc
C_{d_i}	Sectional induced drag coefficient	D_i/qc
C_p	Pressure coefficient	

LIST OF SYMBOLS, continued

Symbol	Definition	Units
D_i	Sectional induced drag	lbs/unit span length
k_α	Aerodynamic spring rate	lbs ft/deg
L	Sectional lift	lbs/unit span length
M_∞	Free-stream Mach number	V_∞/(speed of sound)
M_{LOCAL}	Mach number calculated at panel center	V_{LOCAL}/(speed of sound)
N	Number of panels	
q	Dynamic pressure, $1/2\rho V_\infty^2$	lbs/ft^2
R	Blade radius	ft
Re#	Reynolds number (based on c_{INB})	
r	Distance between a point in the flow field and element dS or dW	
S_t, S_{REF}	Tip reference area	ft^2
S_W	Semi-span wing reference area	ft^2
S_{WET}	Wetted area	ft^2
v	Perturbation velocity	
V	Velocity vector	
V_∞	Free-stream velocity	ft/sec
V_{LOCAL}	Local velocity calculated at panel center	ft/sec
W	Wake surface	
x_{ac}	Sectional aerodynamic center location	
X_{AC}	Lifting surface aerodynamic center location (measured from L.E. of inboard wing)	ft
Y/(B/2)	Normalized span coordinate	
t/c	Thickness ratio	

LIST OF SYMBOLS, continued

Symbol	Definition	Units
Greek Symbols		
α_T	Tip angle of attack	deg
α_W	Semi-span wing angle of attack at structural discontinuity	deg
$\Delta\alpha$	Change in angle of attack due to downwash	
δ^*	Boundary layer displacement thickness	
$\Lambda_{c/4}$	Sweep angle of the quarter-chord line	deg
Λ_{LE}	Sweep angle of the leading edge	deg
γ	Vorticity vector density	
$\Delta\theta$	Tip incidence angle relative to inboard section	deg
Ω	RPM	rev/min
λ	Taper ratio	
ψ	Azimuth angle	deg
μ	Doublet singularity density	
	Advance ratio $V/\Omega R$	
Φ	Velocity potential	
ϕ	Perturbation velocity potential	
ρ	Density	lbm/ft^3
σ	Source singularity density	

1. INTRODUCTION

1.1 FREE-TIP CONCEPT PROJECT STATUS

The free-tip rotor concept has been the subject of a considerable amount of research in the past three years. Its main purpose is to improve rotor performance and reduce vibration. The free-tip is structurally decoupled from the inboard portion of the blade and allowed to pitch about an axis located at the quarter chord of the inboard blade (Figure 1.1); a positive control moment, opposing the negative moment due to lift, is applied to the tip via the pitch shaft. As the blade rotates around the azimuth, the tip weathervanes about an equilibrium position, thus yielding finite lift.

Since helicopter forward flight is characterized by large radial and azimuthal variations in blade loading, the relatively uniform lift produced by the free-tip should improve the overall blade lift-over-drag ratio (L/D). This is achieved by eliminating the negative tip lift on the advancing side usually associated with flight at high advance ratios. Since the amplitude of the lift oscillations should also be reduced, the free-tip equipped rotor will have improved vibration characteristics.

To date, the aerodynamic characteristics of free-tip configurations have been studied experimentally and analytically. In early 1982, an investigation of tip planform influence on the aerodynamic loading of an unswept wing was conducted in the

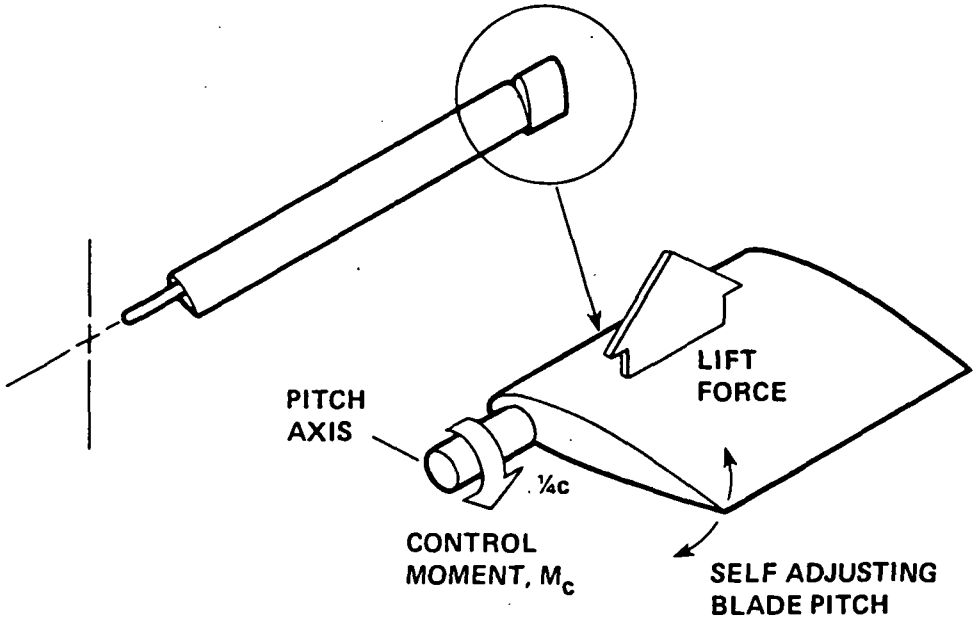

Figure 1.1: Free-tip configuration

NASA 7x10-foot wind tunnel (Reference 1). Several tip configurations were tested and analyzed; this led to the selection of a tip geometry which yielded the desired aerodynamic characteristics. The next phase in the experimental program, which took place in November 1983 (Reference 2), consisted of the testing of a small-scale free-tip rotor. Each of the four blades was fitted with a free-tip which was attached to the inboard portion at the 1/8 chord point (Figure 1.2). The tip planform geometry was based on the results of the 1982 semi-span test. The passive controller generated a nose-up pitching moment which varied with rotor RPM. In the course of this test, the free-tip's response was measured for advance ratios from 0.1 to 0.397, and some performance gains were observed. Another semi-span test was conducted in January 1985: the spanwise variation of wing loading was measured by computing the circulation at various spanwise stations from Laser Doppler Velocimeter data. Flow visualization studies were also performed to determine the geometry and behavior of the strong vortex which is shed at the tip attachment point. A formal report on this latest wind tunnel investigation is still pending. The ongoing analytical effort mainly consists of analyzing the free-tip concept using advanced computer codes.

1.2 FREE-TIP RESPONSE

At this stage in the experimental and analytical study of free-tip performance, the aerodynamic criterion used to measure tip

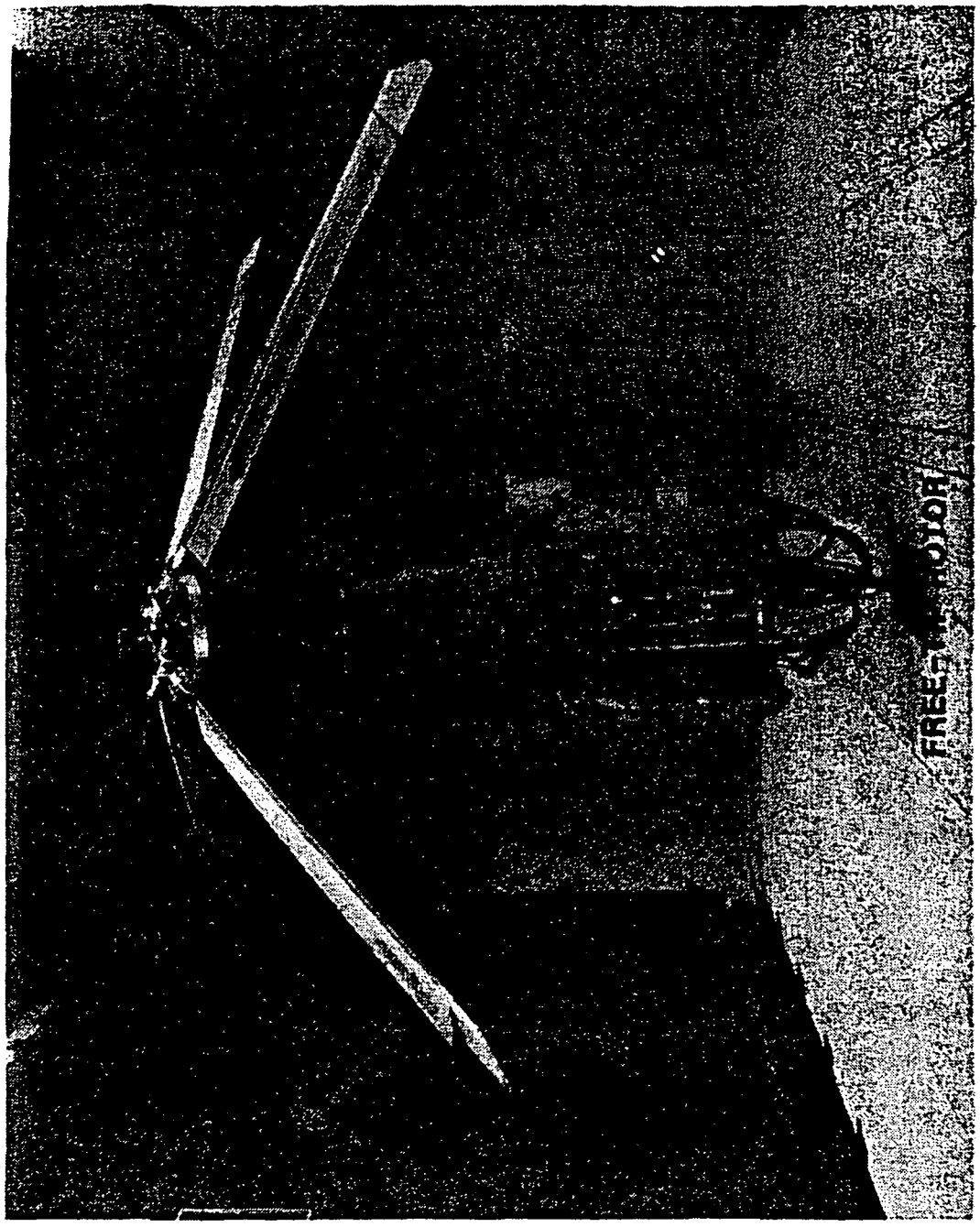

Figure 1.2: Free-tip-equipped rotor in wind tunnel

response is the pitching moment derivative $(C_{m_\alpha})_T$. The magnitude of this parameter is strongly dependent on the offset between the aerodynamic center of the tip planform and the pitch axis. If the tip is swept back, the aerodynamic center is moved aft; with the lift acting at the tip aerodynamic center, the total aerodynamic moment (excluding the controller moment and drag force) about the pitch axis may be written (Figure 1.3)

$$M_A = k_\alpha \alpha = [(C_{L_\alpha})_T \alpha q S_{tip}]\Delta c + C_{m_{ac}} q S_{tip} \bar{c} \tag{1.1}$$

where k_α is the resultant aerodynamic spring rate and Δc is the offset between the pitch axis and the aerodynamic center and is usually negative. Note that α here is measured from the zero-lift line. The aerodynamic spring rate, in pounds-feet per degree of angle of attack, may thus be expressed as

$$k_\alpha = [(C_{L_\alpha})_T q S_{tip}]\Delta c + C_{m_{ac}} q S_{tip} \bar{c}/\alpha \tag{1.2}$$

The pitching moment derivative $(C_{m_\alpha})_T$ is usually expressed in terms of an arbitrarily selected reference point (which for the free-tip is the shaft pitch axis),

$$(C_{m_\alpha})_T = (C_{L_\alpha})_T \left(\frac{X_{REF} - X_{AC}}{\bar{c}}\right) = (C_{L_\alpha})_T \Delta c/\bar{c} \tag{1.3}$$

then Equation (1.2) may be rewritten:

$$k_\alpha = [(C_{m_\alpha})_T + C_{m_{ac}}/\alpha] q S_{tip} \bar{c} \tag{1.4}$$

In Reference 3 it is shown that k_α appears explicitly in the equations of motion of the free-tip. As one of the parameters in

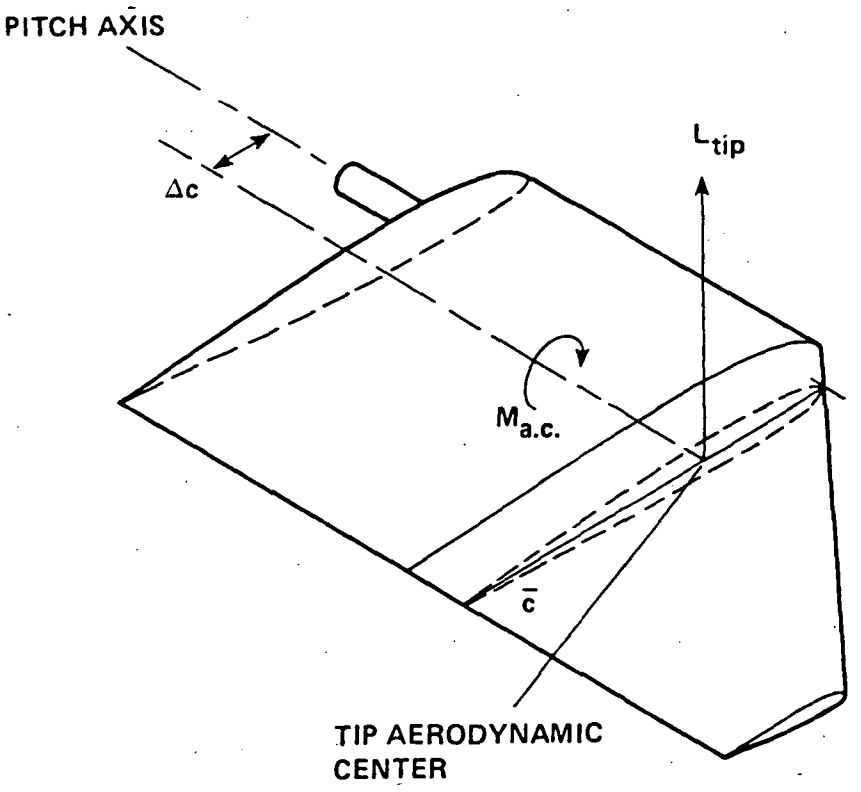

Figure 1.3: Aerodynamic force and moment acting on the free tip

the coefficient of the pitch degree of freedom (first order term), k_α also appears in the expression for undamped natural frequency. Clearly, from Equation (1.4) and its relationship to natural frequency, the derivative $(C_{m_\alpha})_T$ has a significant impact on the response of the free-tip in steady flow and is thus used as the primary design parameter in this study.

1.3 USE OF THE PANEL CODE VSAERO

Because of the technical difficulties associated with the acquisition of tip lift and pitching moment data from an actual rotor in a wind tunnel, much of the aerodynamic data accumulated so far were obtained from tests of fixed semi-span wings with structurally decoupled tips. The tips were not allowed to pitch freely but were set at specified incidence angles with respect to the inboard section. The aerodynamic characteristics of the tip (C_{L_T}, C_{m_T}, and C_{D_T}) were then obtained from force and moment data measured by a balance at the tip junction.

Obviously, to obtain the best possible prediction of free-tip aerodynamic parameters, it is necessary to account for the induced effects of the inboard wing/blade on the tip. Since the loading of a helicopter blade is generally higher at the tip (because of the radial variation of dynamic pressure), the semi-span configuration, with its near half-elliptical spanwise loading distribution, does not adequately represent the physical problem. Therefore, the crucial assumption which has been made in the past and continues to

apply in the present study is that there exists a relationship between the aerodynamic characteristics of a decoupled wing tip in a semi-span configuration and those of a free tip installed on a rotating helicopter blade in forward flight.

As a result of this assumption, analytical tools which were originally developed for the study of fixed-wing configurations may be used to predict the parameters of interest for free-tip applications. The computer program VSAERO, a code designed for calculating the subsonic aerodynamic characteristics of arbitrary configurations, lends itself well to this task. The program allows for the modeling of separate lifting surfaces within a configuration and accounts for the aerodynamic interaction between them. Wake relaxation can also be accomplished by automatic updating of the orientation of wake panels through an iterative process (see Figure 1.4). The potential flow solution is also coupled with a boundary layer routine; in subsequent viscous/potential iterations, the potential flow boundary conditions are modified by a source transpiration technique. Corrections for subcritical compressibility effects are also possible; as will be discussed later, this feature was used in the present analysis.

Although the code provides a method to define regions of separated flow for the computation of nonlinear effects, this capability was not used. For the range of incidence angles in which the free tip typically operates, the flow separates on the lower surface. Several attempts were made to "stitch" the wake along a

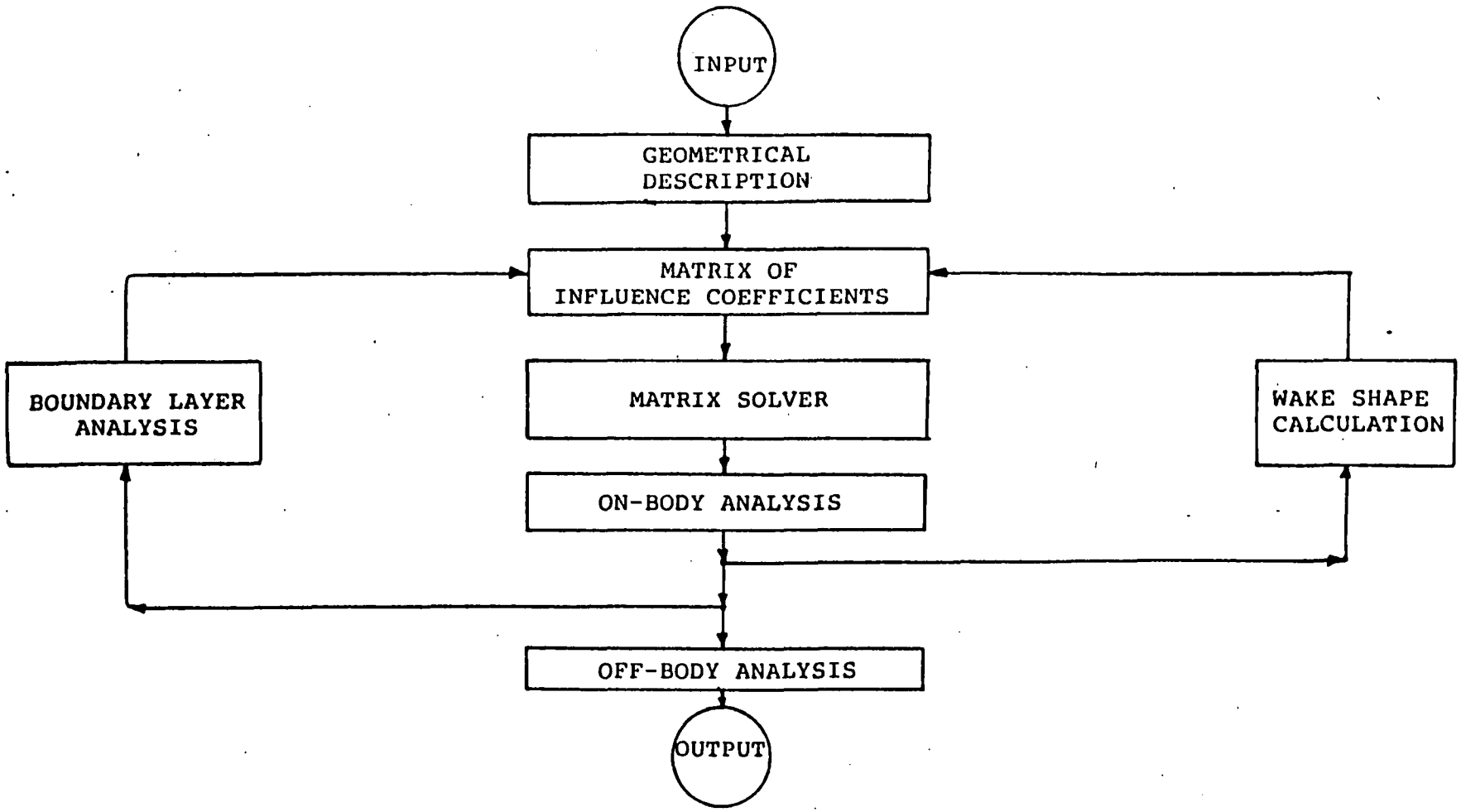

Figure 1.4: VSAERO program global flowchart

separation line defined from boundary layer data, but the computed aerodynamic parameters were highly unrealistic. This feature of VSAERO is still in the development phase at Analytical Methods, Inc., the originator of the program.

1.4 OBJECTIVES OF THE CURRENT STUDY

The objectives of the current study were twofold. First, the VSAERO program was validated for this application by comparing the aerodynamic parameters obtained from various modeling methods with the experimental data of Reference 1. This code was selected because it offered a wide range of possibilities in panel density selection, component identification and modeling, and number of wake shape and viscous/potential iterations.

Second, a new family of tip planforms was designed and analyzed. This was required to increase the magnitude of $(C_{m_\alpha})_T$ of the baseline configuration, and thus achieve better response of the tip to angle-of-attack variations. A steeper pitching moment slope is obtained by increasing the sweep angle of the leading edges: this moves the aerodynamic center aft, increasing the moment arm to the pitch axis. Although a target range of -0.012/deg for $(C_{m_\alpha})_T$ was originally selected, intermediate geometries are also required, since most of the terms which play an important role in the free-tip equations of motion have not been set for a final design yet. These include, for example, the free-tip inertia about the pitch axis and the restoring moment applied by the controller. The aerodynamic

characteristics of the new planforms will serve as an initial data base for future free-tip designs. The lift and pitching moment behavior of the new tips and the semi-span wing drag characteristics due to each configuration were also investigated.

The basic geometry used in this analysis is that of the fixed-wing semi-span configuration described in Reference 1.

2. CORRELATION STUDIES USING VSAERO

This section describes the approach used to model the semi-span wing and tip using VSAERO. The predicted lift, pitching moment and drag of two tip planforms are compared to experimental data; these correlations are analyzed in detail to determine the best modeling method for the design and analysis of new tip planforms.

The theoretical formulation of the VSAERO code is beyond the scope of this report. However, a summary of the analytical development of the program may be found in Appendix A. A more comprehensive description of the solution procedure is given in Reference 4.

2.1 PRELIMINARY CONSIDERATIONS

Before proceeding with the analysis of any configuration with a program of this nature, it is necessary to select the optimum number of body and wake panels along with the required number of wake shape and viscous/potential iterations. The configuration which was considered to determine these parameters consisted of two distinct, separate surfaces with the tip moderately swept (Reference 1); in previous studies, this particular modeling approach was preferred because it closely resembled the actual configuration.

The method which was applied to determine the best panel arrangement is relatively simple. First, a full-cosine distribution was selected for chordwise panel spacing: this results in a higher

panel density at the trailing and leading edges and is desirable for good chordwise loading prediction. A half-cosine distribution defining the spanwise regions was selected for the inboard blade and the inboard and outboard halves of the free tip. This approach generates more panels in the vicinity of the structural discontinuity and the outboard extremity of the free tip which are regions of large spanwise loading gradients for certain tip incidences. Once these parameters were set, the smallest number of panels was determined by increasing their number progressively until convergence of C_L and C_m values for both lifting surfaces was achieved.

The final combination therefore consists of 15 chordwise divisions (on both the upper and lower surfaces) for all airfoil sections defined in the configuration; the inboard blade is divided into 7 spanwise columns while the tip is divided into 6 similar regions. The body surface therefore consists of 495 panels, as shown in Figure 2.1. This number includes 15 vertical panels closing each of the tips of both components at the gap. As will be seen later, this approach was reevaluated in the correlation studies. There are 75 vertical panels on the most outboard tip section.

The spanwise wake panel distribution is automatically set by the selected number of wing panel columns; i.e., each column of wing panels sheds one column of wake panels. The streamwise number of divisions in the wake was set to 20, with a higher panel density at

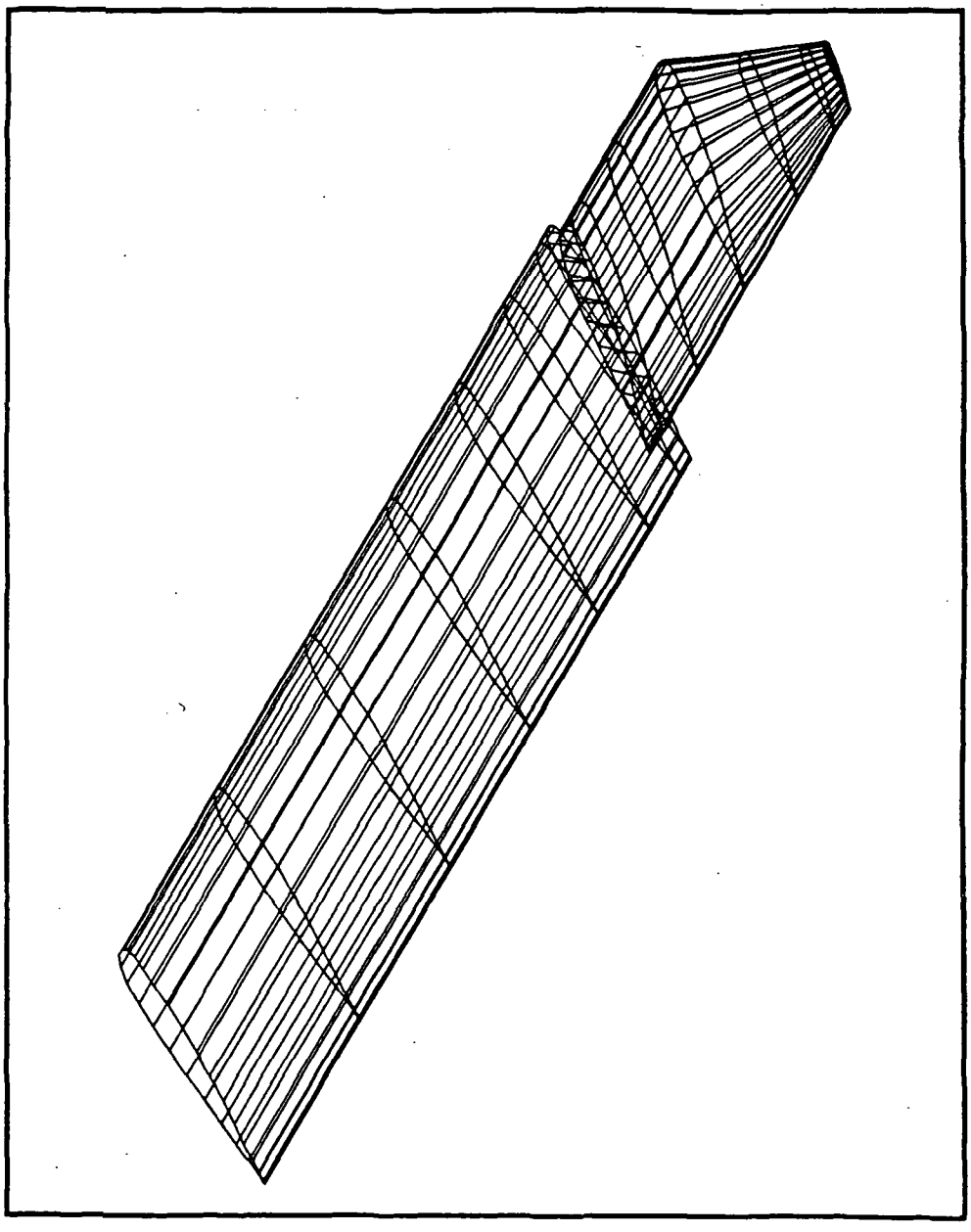

Figure 2.1 (a): Semi-span wing configuration with TIP 1A

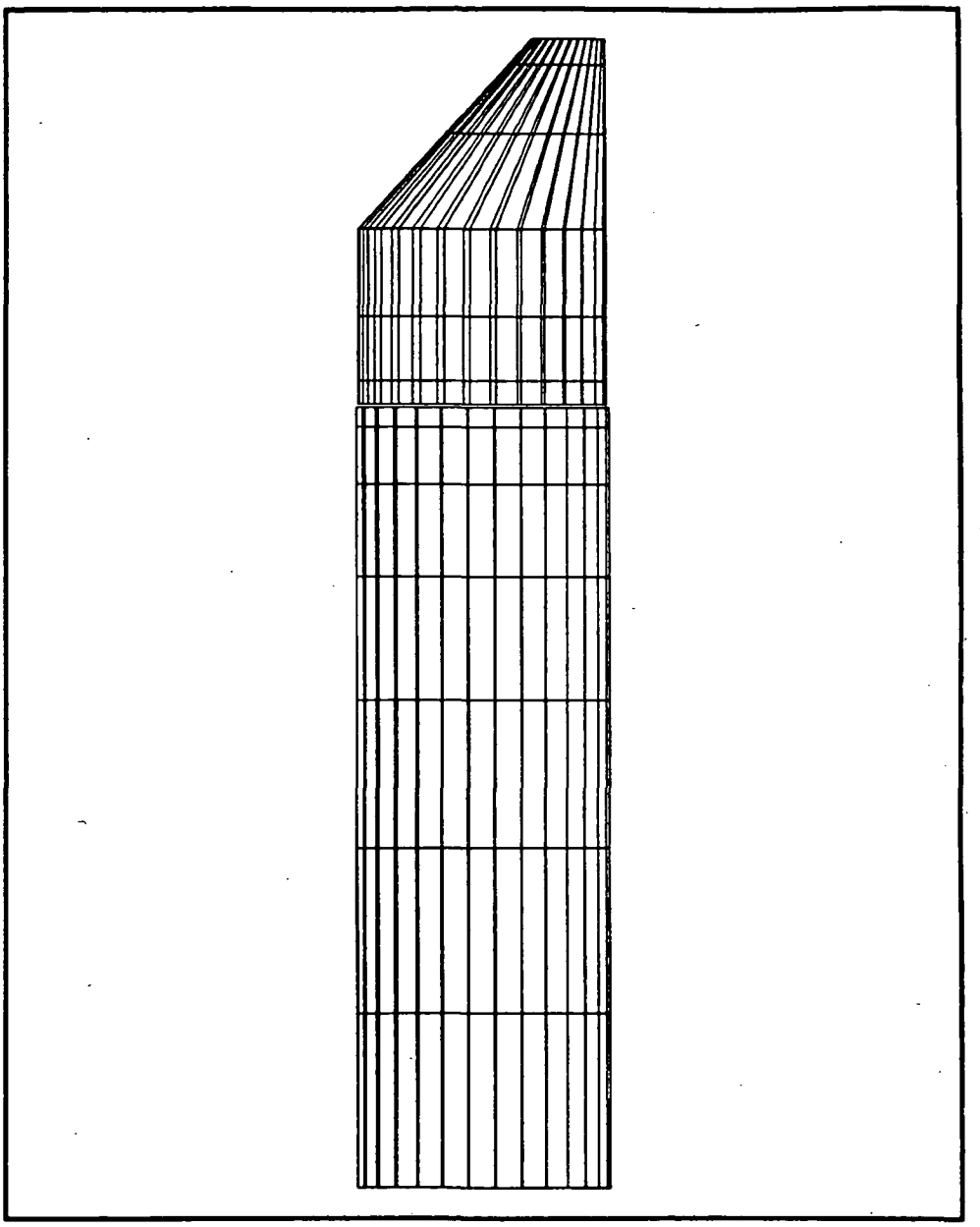

Figure 2.1 (b): Semi-span wing configuration with TIP 1A (top view)

the wing trailing edge. The total number of wake panels therefore amounts to 260 (13 columns x 20 divisions, Figure 2.2). However, since the upstream edge of the wake was defined (by the present user) slightly behind the quarter chord line, some wake panels overlap the body and are not shown. The upstream edge was selected at this location because it was originally intended to stitch the flow separation line. Unfortunately, the use of this option was not successful, due to lack of information and limited user experience. Therefore, for all cases compiled in this report, separation was assumed to take place at the trailing edge. Even if some wake panels are tentatively defined upstream of the trailing edge by the user, the code will correct automatically if trailing-edge separation is selected later in the wake geometry definition. For this reason, only 182 wake panels are actually needed, as shown in Figure 2.2. The downstream edge of the wake is located roughly 7.5 chord lengths behind the trailing edge.

Generally, the solution converged for a small number of viscous/potential iterations. Since only the right-hand sides of the system of linear equations to be solved by the code (see Appendix A, Equation A.14) are affected by the source transpiration values returned from the boundary layer routine, specifying viscous/potential iterations does not result in prohibitive CPU costs. In the present application, three such iterations were considered to be adequate. When the wake relaxation loop is executed, the wake panels are repositioned so that their streamwise edges are aligned with the local calculated flow direction.

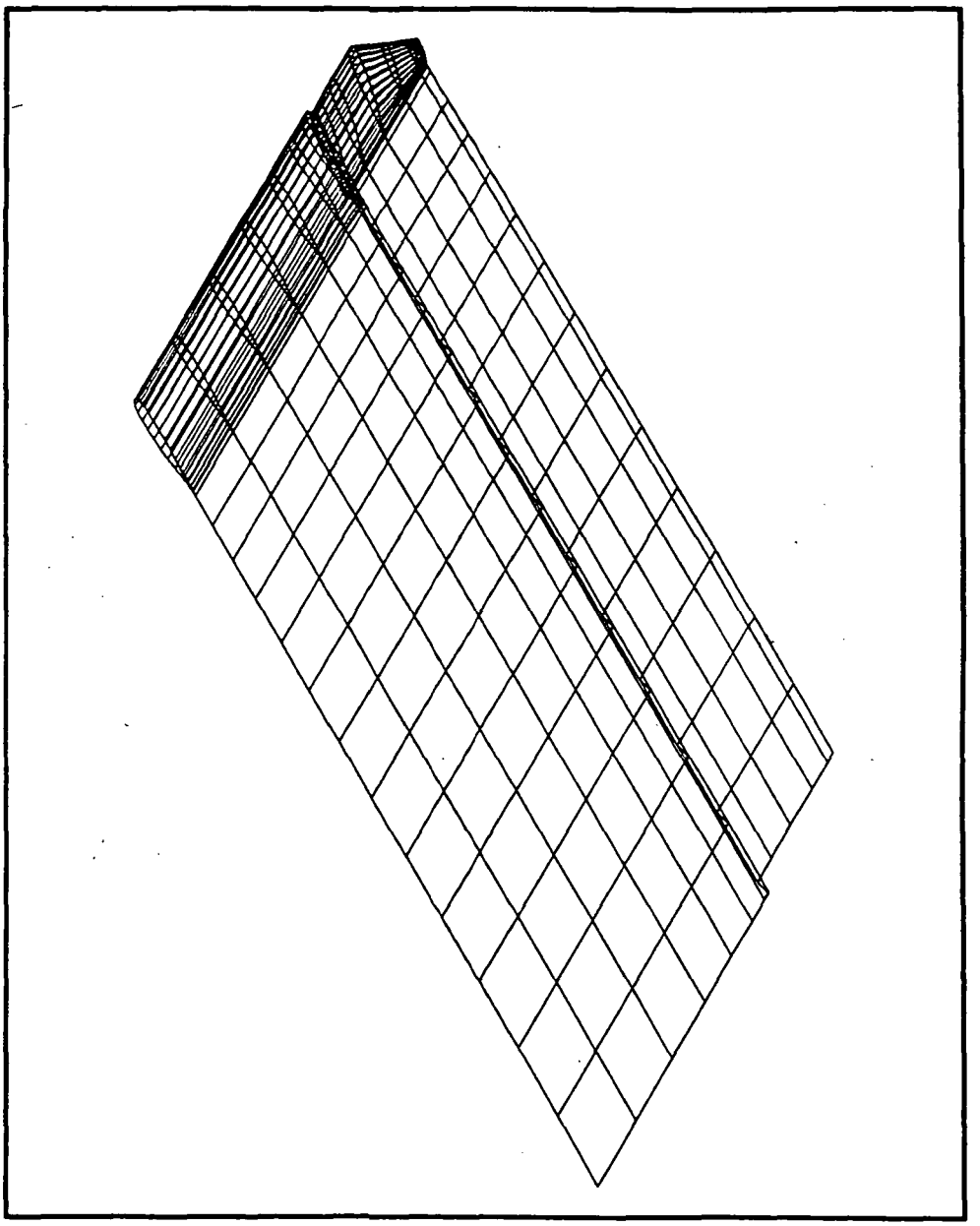

Figure 2.2 (a): Semi-span wing and tip wake panels

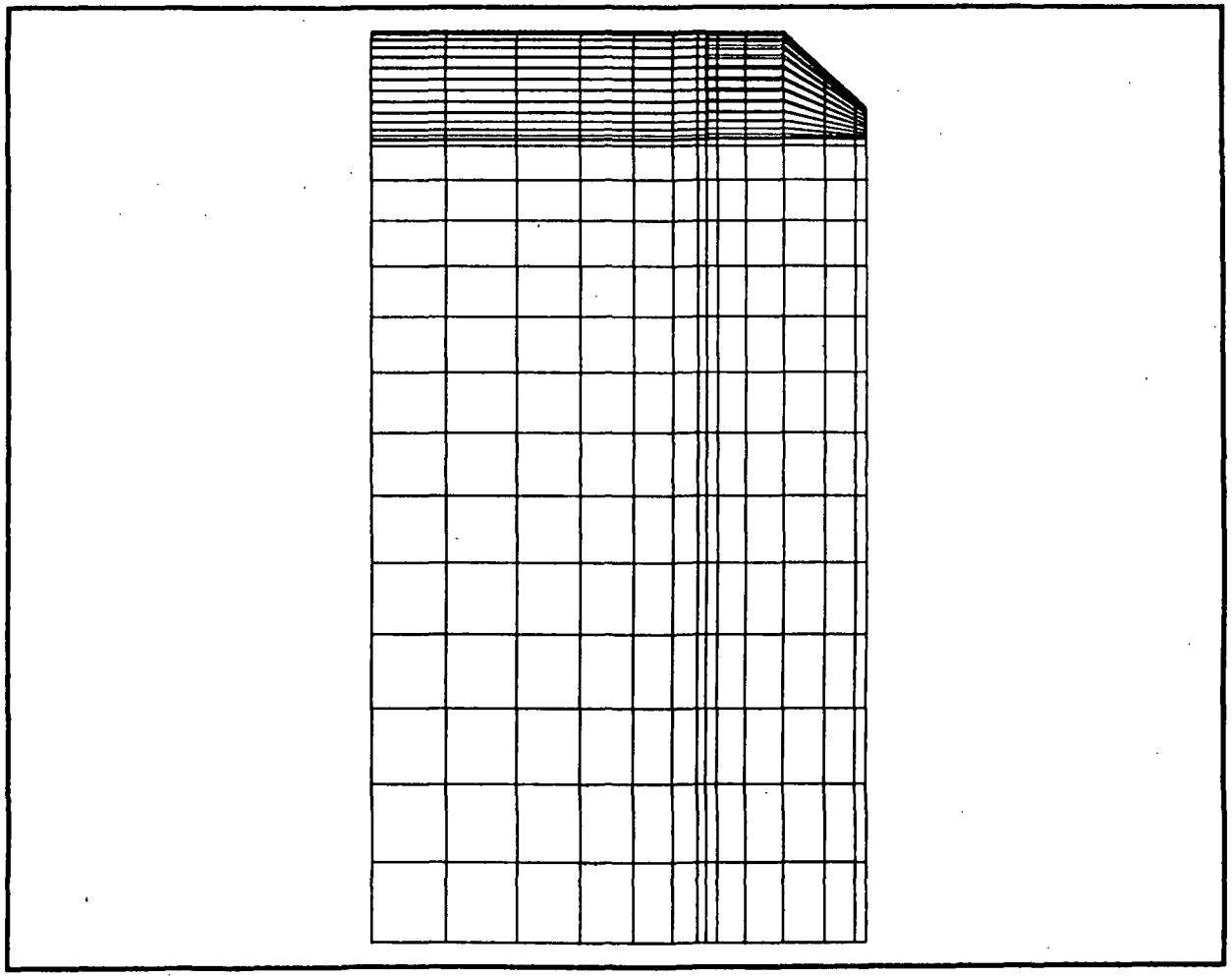

Figure 2.2 (b): Semi-span wing and tip wake panels (top view)

Equations (A.14) also illustrate the fact that wake shape iterations require that the wake influence coefficients be recomputed, increasing the required CPU time. Therefore, one wake shape iteration per viscous/potential iteration was used as a compromise to reduce job processing times.

Two integral boundary-layer routines are available in the VSAERO program. The first is based on the computation of boundary-layer characteristics along external surface streamlines. The procedure accounts for surface curvature and streamline convergence/divergence under the assumption of local axisymmetric flow. In earlier studies, when the leading edges of the free-tip were only moderately swept, the procedure was acceptable. However, Reference 4 shows that this 2-D method could break down in regions of high crossflow. Recent investigations with swept tips have confirmed this finding. In cases where some regions of separated flow (however small) were encountered, the computed local skin friction drag contribution was large and negative. In view of this problem, the second boundary-layer routine, which includes a crossflow model, was used for the analysis of the new configurations. The user prescribes a series of chordwise strips across the wing surfaces where the analysis is desired.

The preceding figures (2.1 and 2.2) illustrate the final body and wake panel distributions which were used for the correlation of tip lift, drag, and pitching moment. The wind tunnel walls and test section were not modeled for the correlation phase of this study.

2.2 VSAERO CORRELATION WITH WIND TUNNEL EXPERIMENT

The main purpose of this phase of the research is to obtain the best possible correlation of C_{L_T} and C_{m_T} with experimental results. Also, an investigation of the tip's drag polars will be carried out. First, it is necessary to define the tip incidence relative to the inboard blade as

$$\Delta\theta = \alpha_T - \alpha_W \tag{2.1}$$

where the angle of attack in the tests of Reference 1 was measured relative to the tunnel floor. In this numerical application, α_T and α_W are measured from the x axis of the global coordinate system (which is located at the quarter chord of the section at the plane of symmetry); the free-stream velocity vector is parallel to this axis. From the rotor test results of Reference 2, the $\Delta\theta$ of the tip is usually negative for all azimuthal positions of the blade; however, in the semi-span wing experimental results of Reference 1, the $\Delta\theta$'s were limited to values of +5.0, 0.0, and -5.0 degrees. Since the data of Reference 2 represent more recent findings on free-tip behavior in forward flight, it was decided to limit the correlation to the only negative value of $\Delta\theta$ for which experimental data are available, i.e. $\Delta\theta = -5°$.

The airfoil section used for all free-tip designs discussed in this report is the V23010-1.58, a modified version of the NACA 23010 section. Its most noticeable feature is the drooped leading edge region. The twist distribution of the inboard wing is nonlinear,

with a maximum variation of 0.321 degrees from the root to the beginning of the tip section. The free-tip planforms considered have all been designed without twist. More information on the V23010-1.58 airfoil and on the semi-span twist distribution is contained in Reference 1. For the correlations that follow, two configurations taken from Reference 1 were modeled using VSAERO. The planform parameters appear in the following table:

Table 2.1: Geometric Parameters for TIP 1A and TIP 1B

	Λ_{LE} (deg)	$\Lambda_{c/4}$ (deg)	λ	c_{INB} (m)	$\bar{c}$ (m)	S_t (m^2)
TIP 1A	42	35	0.3	0.208	0.170	0.0532
TIP 1B	48	45	0.6	0.208	0.187	0.0683

Both tip planforms were analyzed for correlation of lift, drag, and pitching moment. In this chapter, the computed values of pitching moment coefficient are normalized by the mean geometric chord of the tip surface ($\bar{c}$).

2.2.1 Lift and Pitching Moment Correlation

Three different methods were used to model the structural discontinuity between the outboard surface and the inboard section:

- two separate components, closed tips
- two separate components, open tips
- single continuous surface, with a step change in incidence at the tip junction

Figures 2.3 and 2.4 illustrate the tip paneling arrangement for the first method, which initially seemed to be the most logical approach. The two surfaces are separated by a gap of roughly 3 mm; observe that both the inboard section tip and most inboard extremity of the free-tip have been paneled. This is the most distinctive feature of this particular approach. The results obtained from VSAERO are plotted against experimental data in Figure 2.5.

To obtain these data, the angle of attack of the entire configuration (wing and tip) was varied with $\Delta\theta = -5°$ held constant as discussed earlier. The results indicate that the predicted tip lift is nonlinear for the entire range of α_T under consideration. This effect is believed to be related to potential flow effects in the gap region. Since the boundary-layer method which accounts for crossflow effects was used in this study, viscous effects could not be modeled in the gap between the surfaces. Therefore, the fluid flows through the narrow gap and around the corners created by the end cap panels and upper and lower surface panels. This results in high local velocities and large values of C_p on the panels adjacent to the gap. Another possible factor in this problem could be that of control point/panel edge proximity. Since a doublet panel is equivalent to a quadrilateral vortex ring, control points on the end cap panels are close to the upper and lower surface panel edges for certain values of $\Delta\theta$. This effect may lead to local numerical problems in the solution. It is clear that no pitching moment correlation can be obtained using this approach.

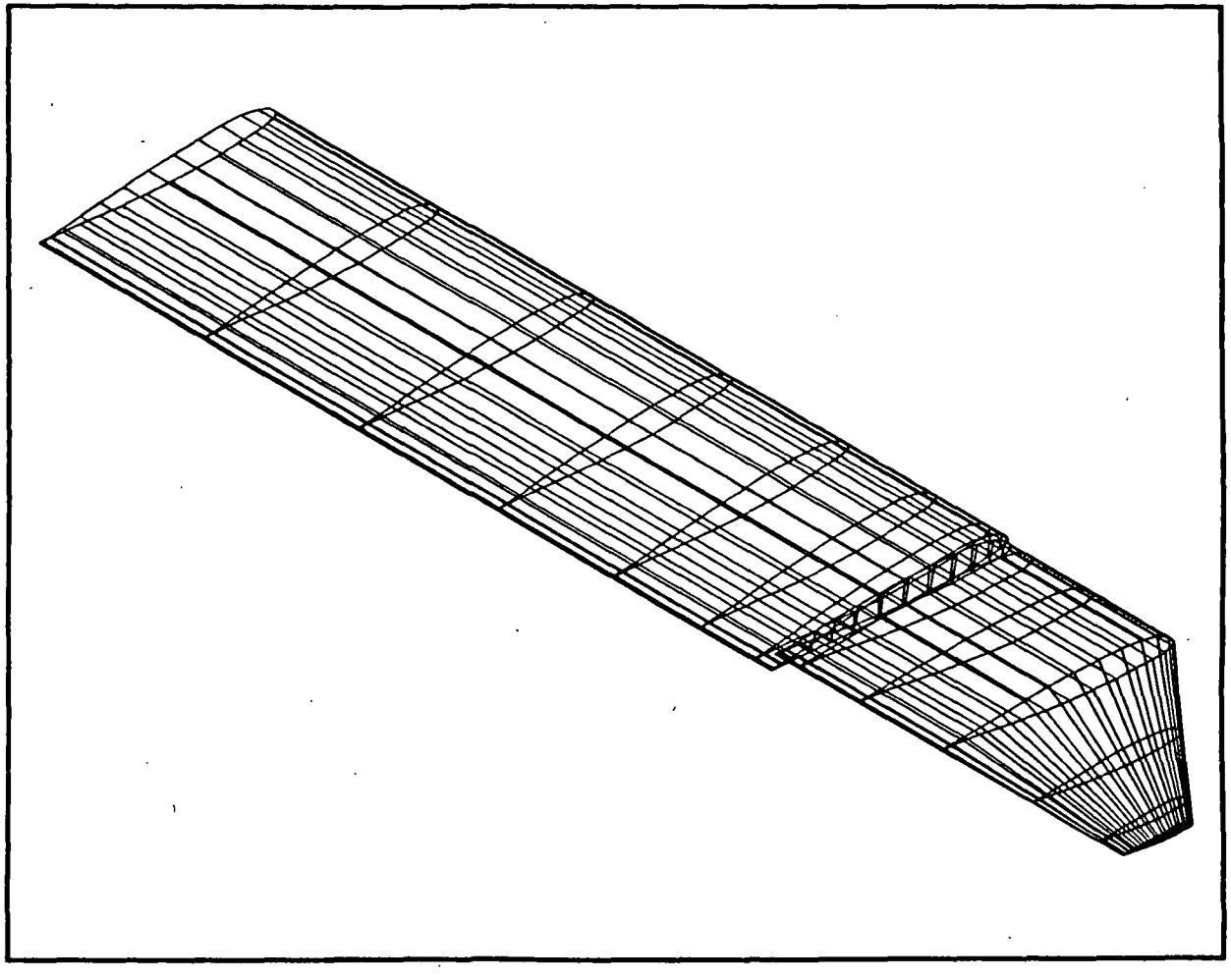

Figure 2.3: Semi-span wing and tip modeled as separate components

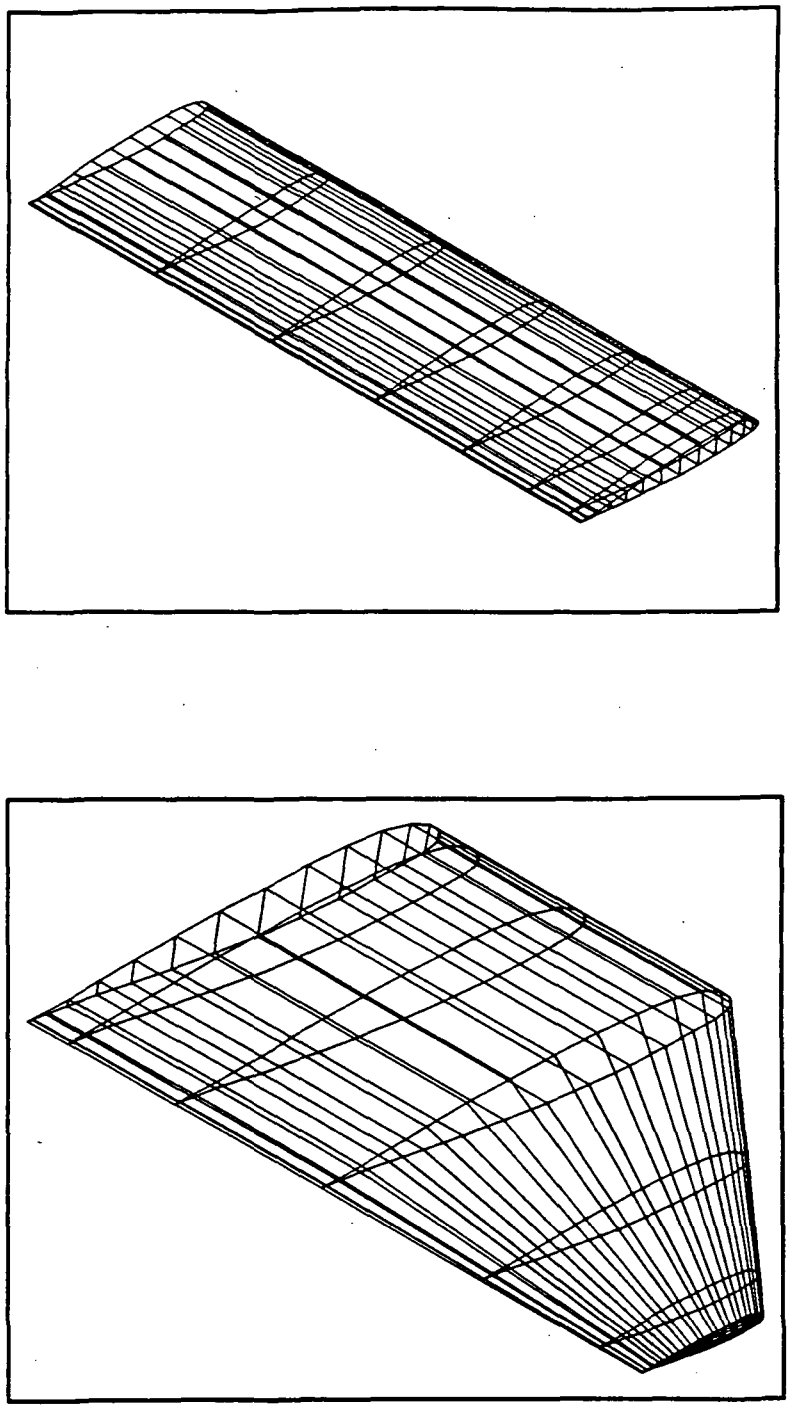

Figure 2.4: Inboard and outboard sections showning panels closing tips

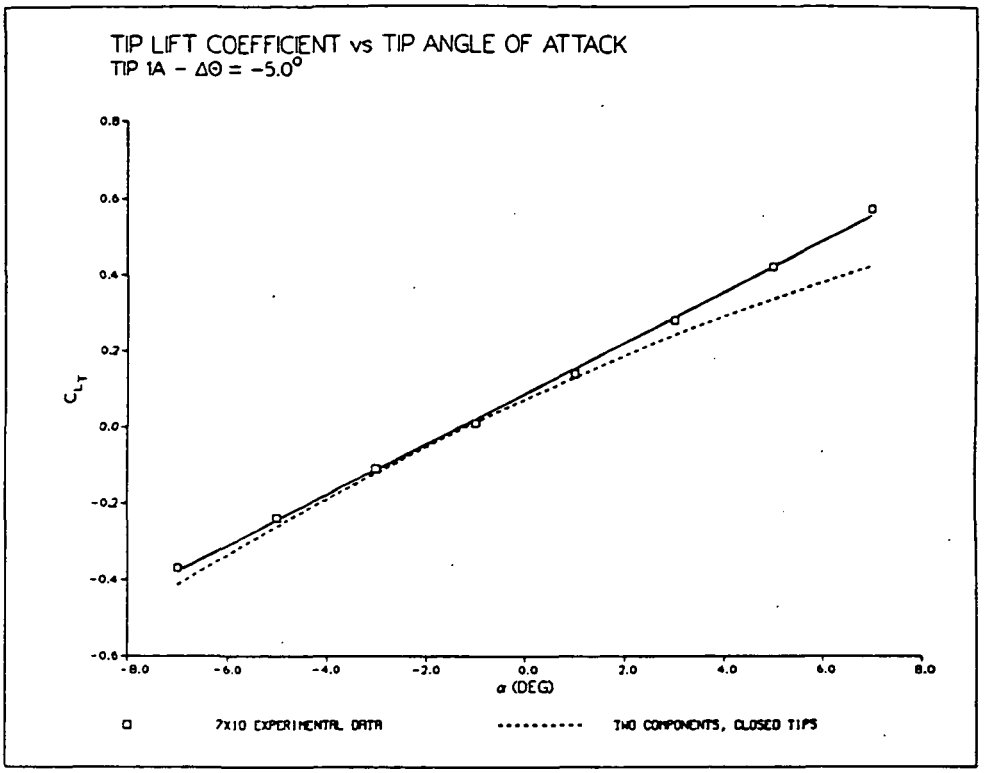

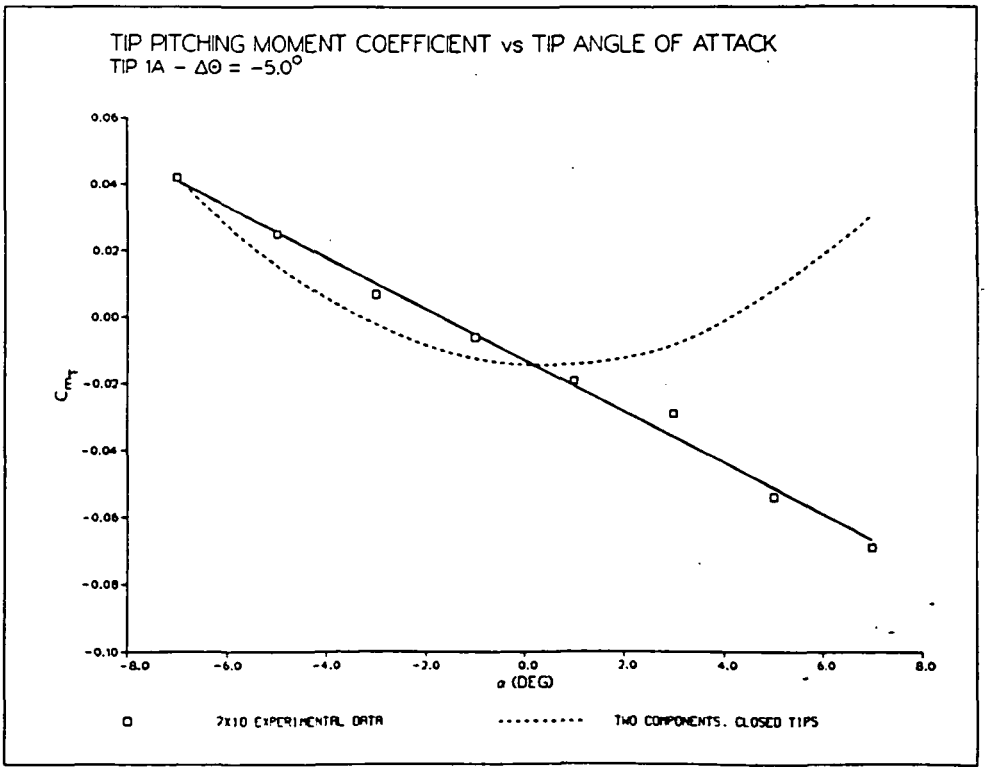

Figure 2.5: Tip lift and pitching moment variation with angle of attack; separate components, closed tips

The next step consisted of removing the panels on the wing and tip walls forming the gap, while maintaining the finite distance between the two surfaces. According to Reference 4, this type of approach is not allowed, since some "leakage" of the internal flow potential will occur. This will also prevent the boundary conditions from being satisfied over the entire surface and internal volume; but if the end caps are small, the effect on the integrated force and moment coefficients should be minimal. Figure 2.6 shows a substantial improvement in the prediction of lift with this new approach. A major improvement is also noted in the pitching moment curve, where the standard linear behavior is now apparent. However, the predicted theoretical slope is more positive than the experimental value.

Since the integrated tip lift prediction is excellent using this approach, the C_{m_T} data suggest an error in the prediction of the tip surface aerodynamic center location, X_{AC}. Calculation of X_{AC} by taking the ratio of $(C_{m_\alpha})_T$ to $(C_{L_\alpha})_T$ shows that the value obtained from VSAERO results falls short by 14.6% of the experimental value. VSAERO thus predicts X_{AC} to be closer to the leading edge, thus resulting in a smaller value of $(C_{m_\alpha})_T$ than for the experimental data. As will be seen later, this error in X_{AC} prediction is not unique to method 2 (no end cap panels). It is difficult to determine the reason for errors in X_{AC} prediction. One possible cause may be related to the assumption that no separation takes place over the tip surface for the range of α_T studied. If

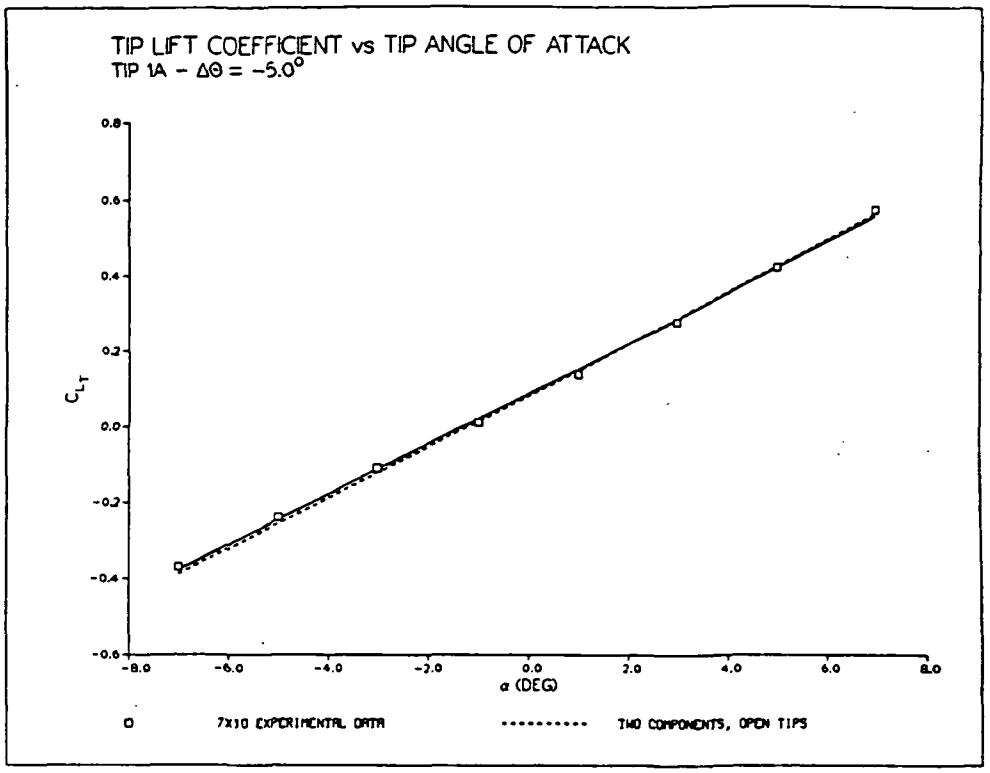

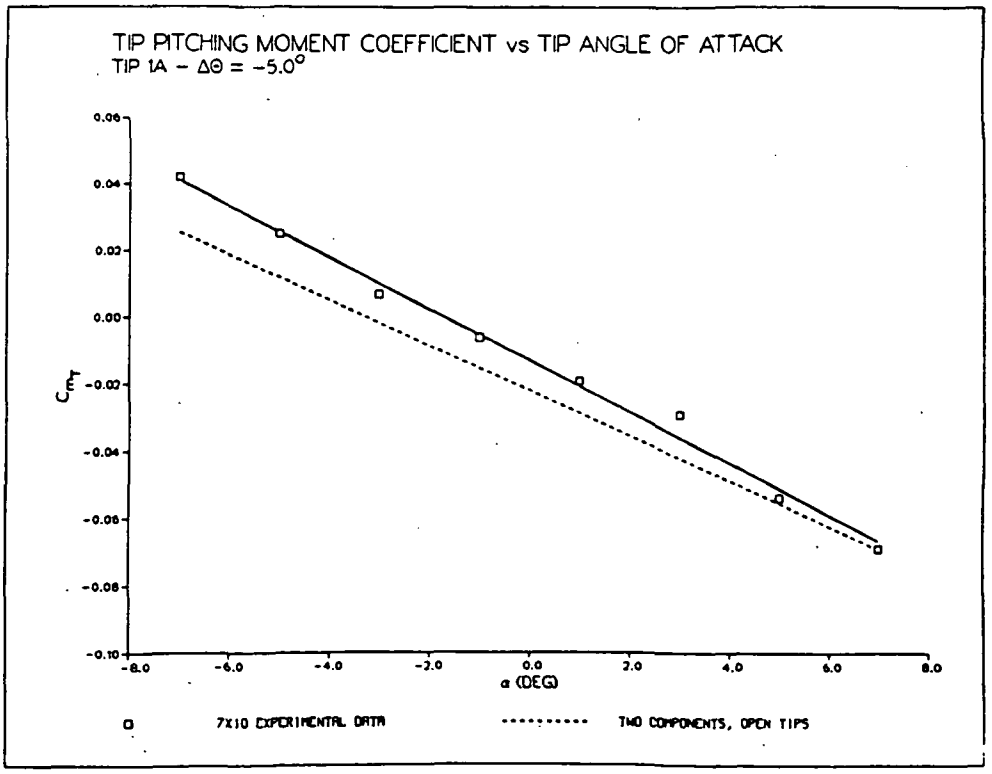

Figure 2.6: Tip lift and pitching moment variation with angle of attack; separate components, open tips

separation did occur in the actual wind tunnel tests at higher values of α_T, the code could not predict with great accuracy the surface pressure in the separated region given the attached flow model used. Clearly, the improvements in C_{L_T} and C_{m_T} vs α_T observed in Figure 2.6 as compared to the results of Figure 2.5 are related to the removal of panels from different components facing each other across the gap. Also, as will be shown in Section 2.2.3, the skin friction drag component is consistently underpredicted by the version of VSAERO available at NASA Ames. Some error thus results in the computation of C_{m_T}, since drag contributes to a small extent to pitching moment (see Appendix A, Equations A.21 and A.25). The limitations described here indicate that satisfactory prediction of both C_{L_T} and C_{m_T} using the same modeling technique is difficult to achieve. Despite this, the third modeling method was investigated. In this approach, the configuration consists of a single continuous surface. Figure 2.7 shows that the inboard wing and tip section are linked by a common section made up of panels which are stretched into a near vertical position. Figure 2.8 illustrates the resulting C_{L_T} and C_{m_T} curves compared to the experimental data and the open-tips method results.

The overprediction of lift can be attributed to the presence of flow singularities on the panels spanning the gap. Since a continuous wake was defined for the entire span in this modeling method, the Kutta condition was imposed at the trailing edges of the panels across the gap. Because of this condition, the solution

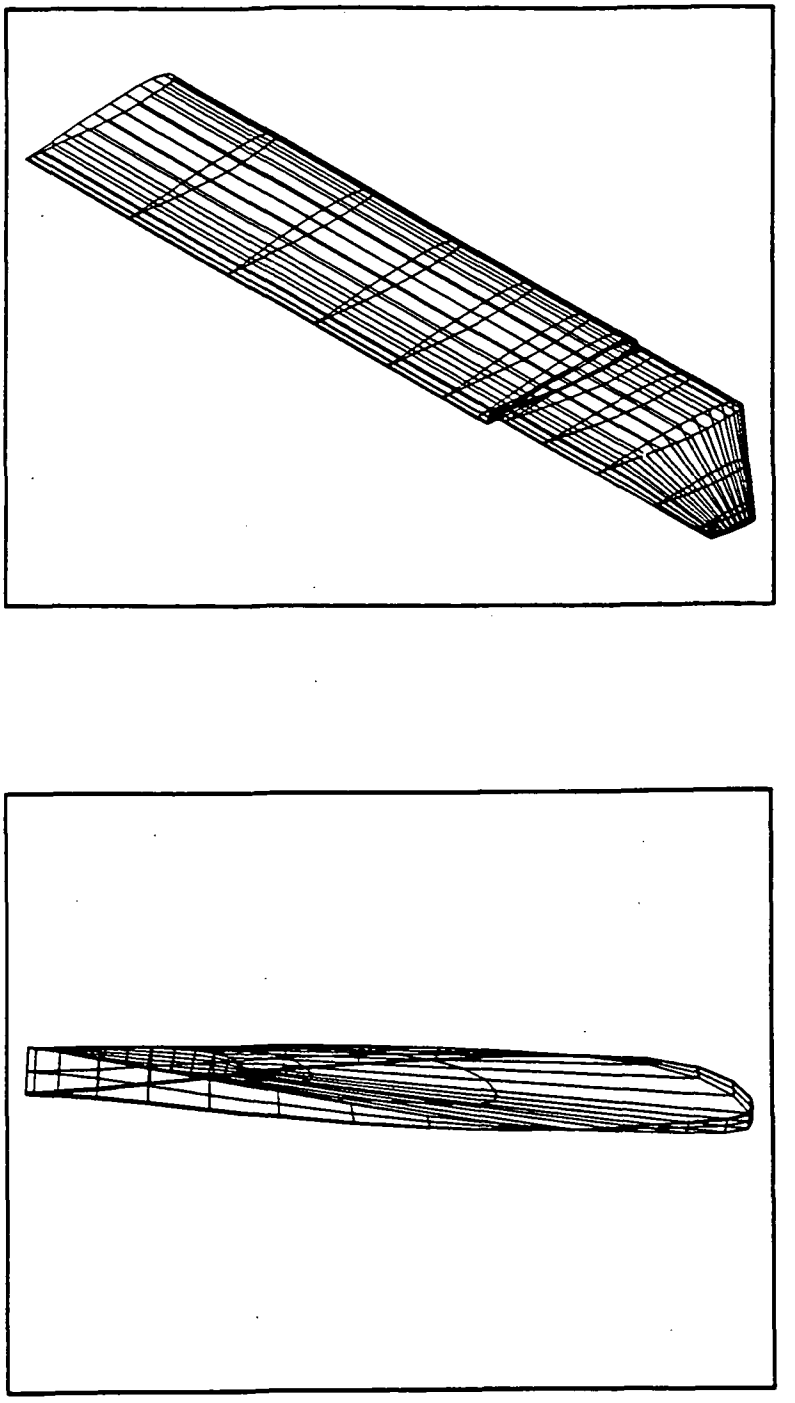

Figure 2.7: Semi-span wing and tip modeled as a continuous component with step change in incidence

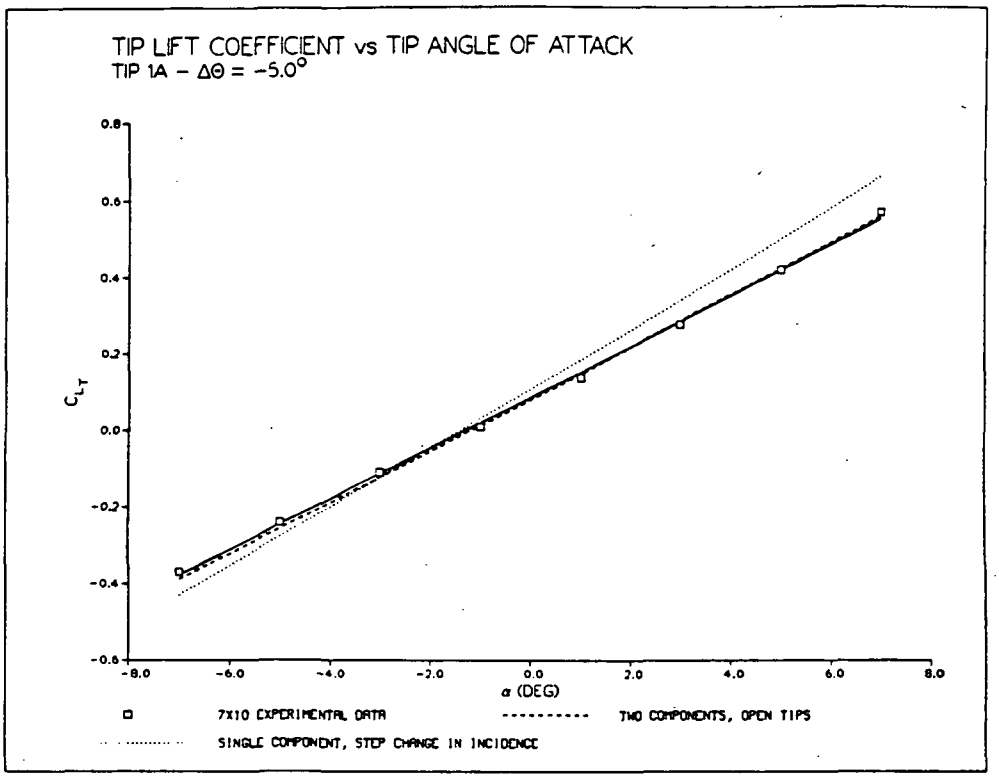

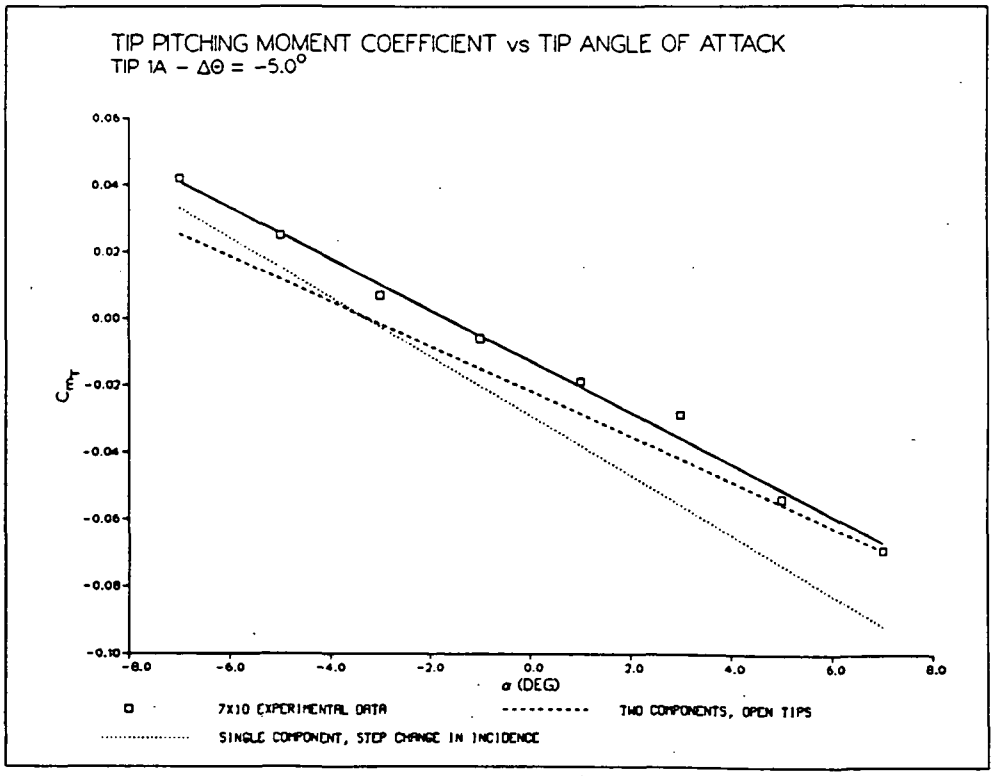

Figure 2.8: Tip lift and pitching moment variation with angle of attack--TIP 1A

yielded doublet strengths in this area which were roughly of the same magnitude as those located on the adjacent lifting surfaces. These flow singularities induce velocities which alter the angle of attack distribution at the tip, thus resulting in an overprediction of lift. Although the resultant force normal to these panels produces some lift, its contribution was not added to the tip lift. The pitching moment curve is also steeper than that obtained from experimental results. This indicates that the overprediction of lift overcomes the error in X_{AC} to yield higher magnitudes of pitching moment.

Figure 2.9 shows the variation of tip pitching moment with tip lift. The underpredicted slope obtained from the open-tips method can again be attributed to the error in X_{AC} prediction. As expected, this plot also confirms that VSAERO does not predict the zero-lift pitching moment accurately, thus resulting in a vertical offset of the curve compared to experimental results. Note the excellent slope correlation associated with the step change in incidence method.

To verify the trends observed in lift and pitching moment variation for TIP 1A, a comparison of the characteristics of TIP 1B (Figure 2.10) with experimental data was carried out. Notice that TIP 1B has a higher sweep angle, and the aerodynamic center is farther aft than for TIP 1A. The variation of lift and pitching moment coefficients with angle of attack are shown in Figure 2.11. The same basic trends observed for TIP 1A also prevail in this

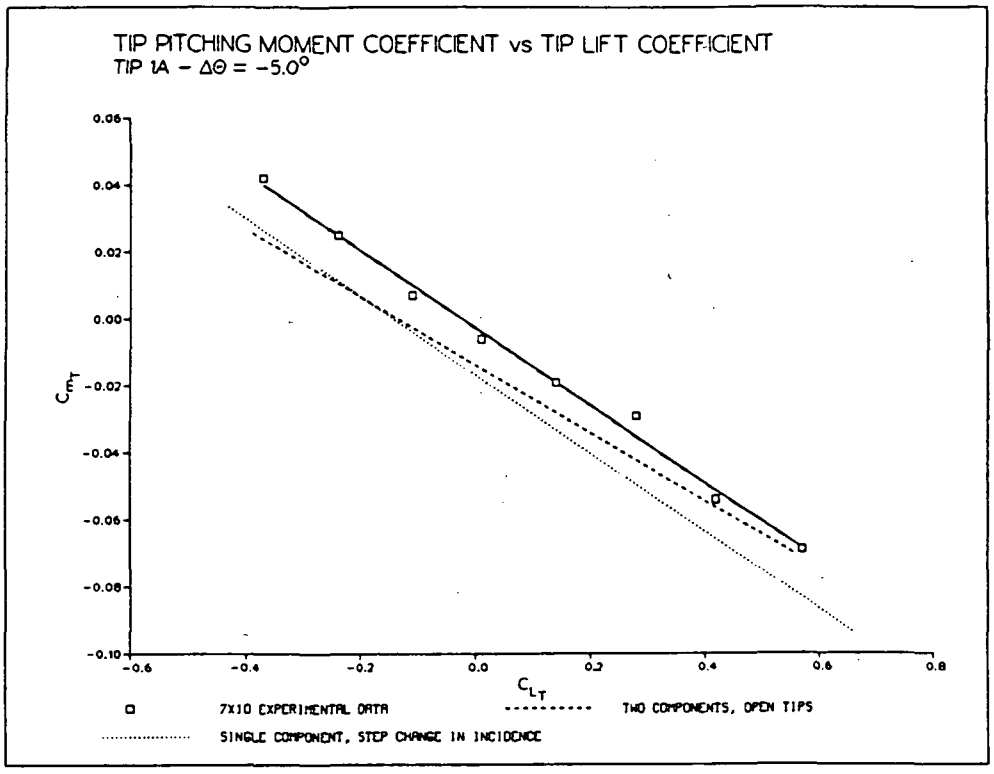

Figure 2.9: Tip pitching variation with lift--TIP 1A

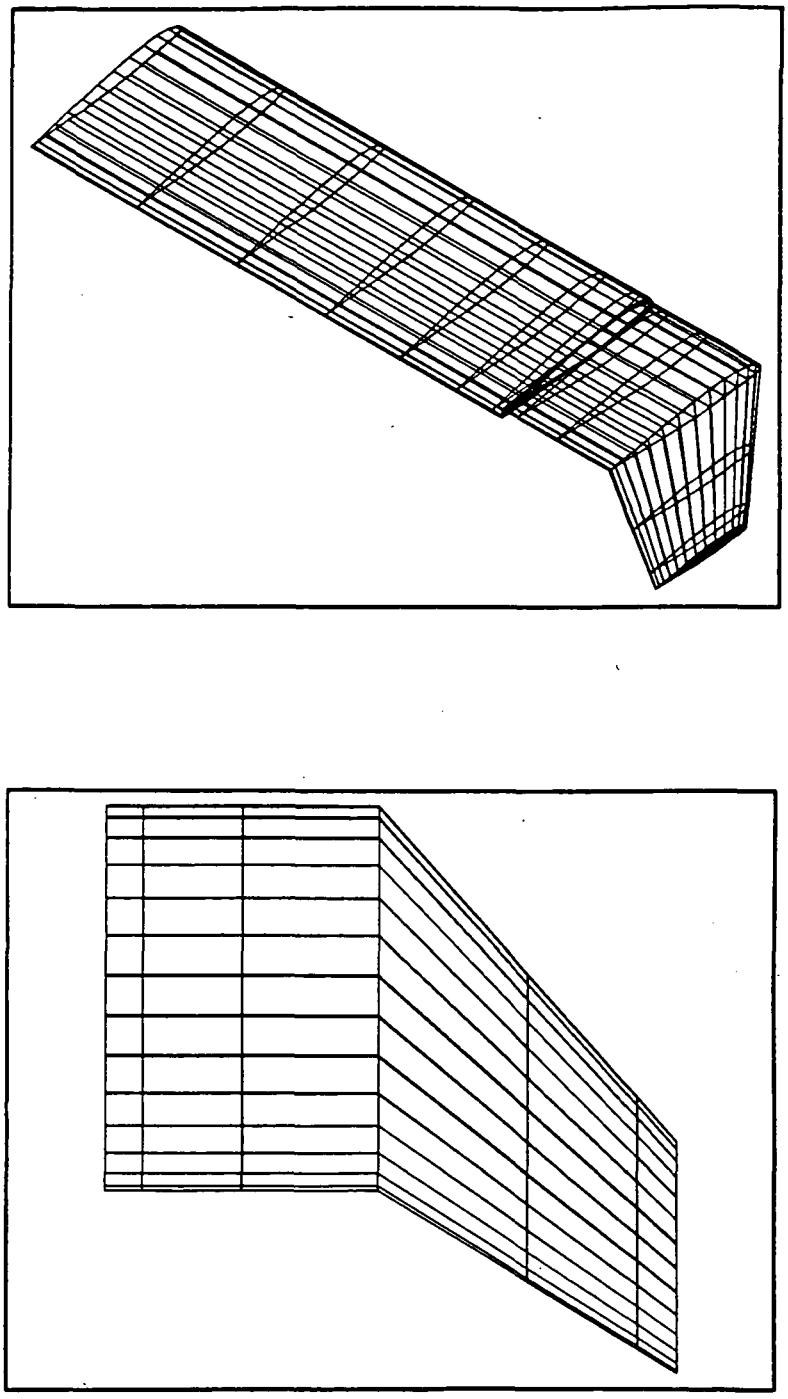

Figure 2.10: Semi-span wing configuration with TIP 1B

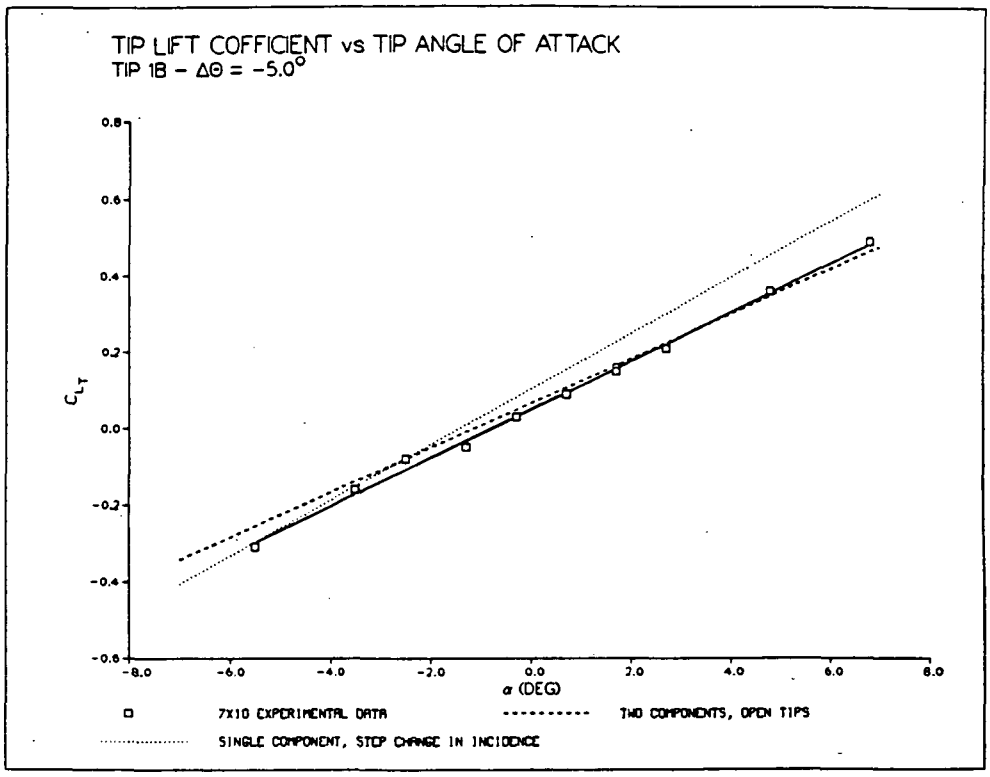

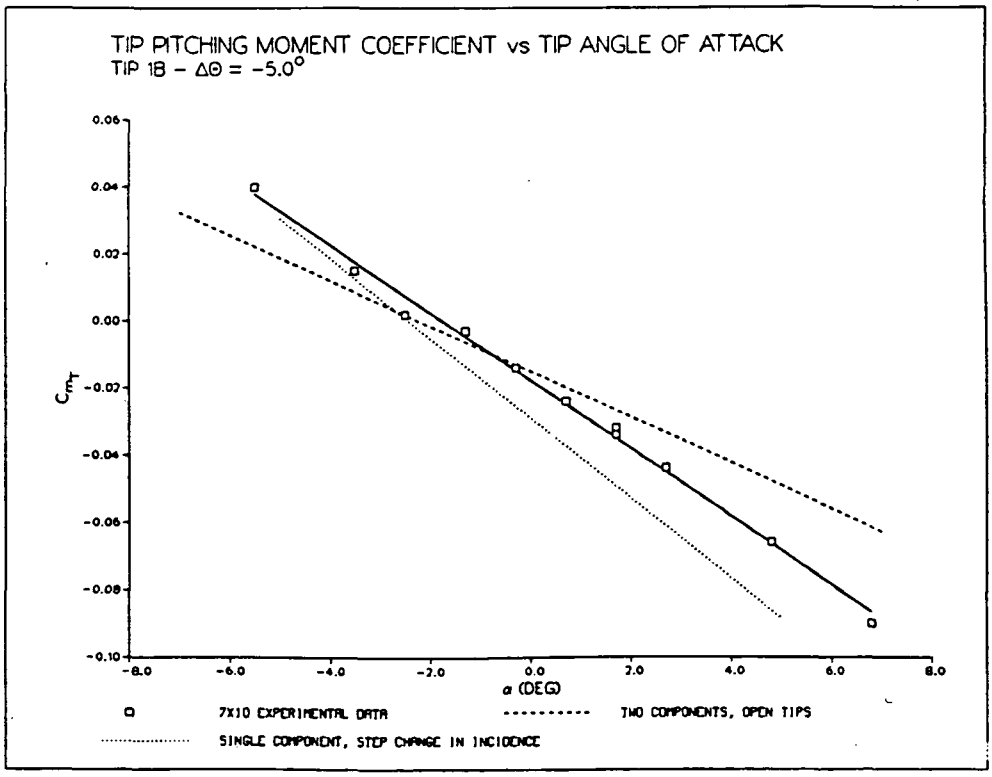

Figure 2.11: Tip lift and pitching moment variation with angle of attack--TIP 1B

case. Although the lift prediction is more accurate with the open-tips method, it is slightly underpredicted. Because of the higher quarter chord sweep angle of this tip planform, it is likely that larger regions of separated flow will occur at high angles of attack, as compared to TIP 1A. This would result in higher levels of pressure drag. The underpredicted magnitudes of C_{L_T} along with the error in X_{AC} location, poor skin friction and pressure drag predictions, probably all acount for the degradation of the pitching moment correlation observed here for the open-tips method.

Once again, the step change in incidence yields slightly higher lift and pitching moment variations with angle of attack. Figure 2.12 also confirms the previous conclusion concerning the dC_{m_T}/dC_{L_T} slope: the single-component method yields the best correlation. Note that since the lift is overpredicted in the C_{L_T} vs α_T curve (Figure 2.11), it is reasonable to assume that the good correlation shown in Figure 2.12 for the step change in incidence approach (i.e., almost matching slopes) is due to a combination of the overprediction of lift in the positive C_{L_T} range (negative C_{m_T}) and a resultant X_{AC} closer to the pitch axis than would be obtained experimentally. As mentioned previously, the overprediction of lift is related to the induced velocities at the tip. In spite of these problems, the data of Figures 2.8, 2.9, 2.11, and 2.12 show that the continuous component with step change in incidence yields the best prediction of pitching moment slope. For the range of sweep angles investigated, the correlations show that a maximum error of roughly

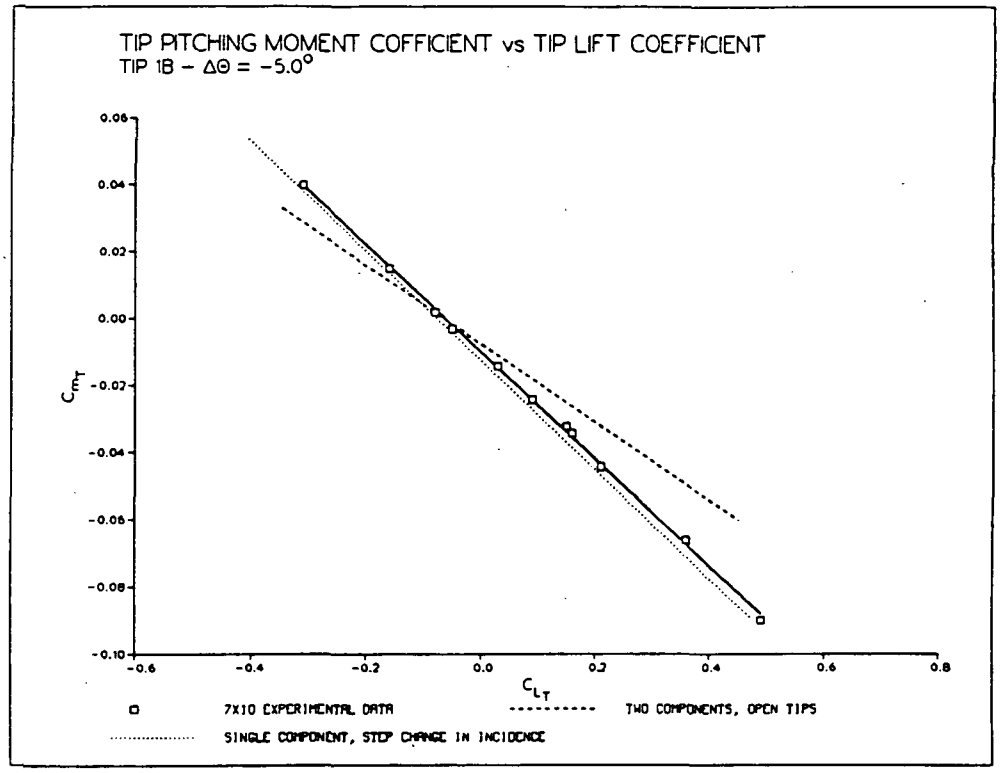

Figure 2.12: Tip pitching moment variation with lift--TIP 1B

10-15% can be expected in $dC_{m_T}/d\alpha_T$ as compared to the experimental value.

2.2.2 Spanwise Loading Correlation

To analyze the correlations of the previous sections in further detail, a study of the spanwise variation of sectional lift coefficient was carried out. Experimental data obtained from a wind tunnel test of the same configuration under consideration here were obtained from Reference 6. Flowfield velocities were measured using a Laser Doppler Velocimeter apparatus. The circulation at specified span stations was calculated by integration of these velocities along closed paths. The comparisons presented here are for TIP 1A.

The VSAERO data were obtained at 12 spanwise stations for the inboard wing and at 10 stations in the tip region. The numerically predicted values of sectional lift were normalized using the inboard wing chord. Figure 2.13 illustrates the correlation of these data with experimental values for $\Delta\theta = 0.7°$, and $-4.3°$. Results obtained from the three modeling methods discussed in the previous section are shown. The inboard wing angle of attack is 6.6° for all four cases; the structural discontinuity is located at Y/(B/2) = 0.676. Figure 2.13 clearly shows the singular behavior at the structural discontinuity when the closed-tips method is used. As explained in Section 2.2.1, this is caused by potential flow effects and/or control point/panel edge proximity. For positive values of tip lift coefficient, it is seen that the step change in incidence method

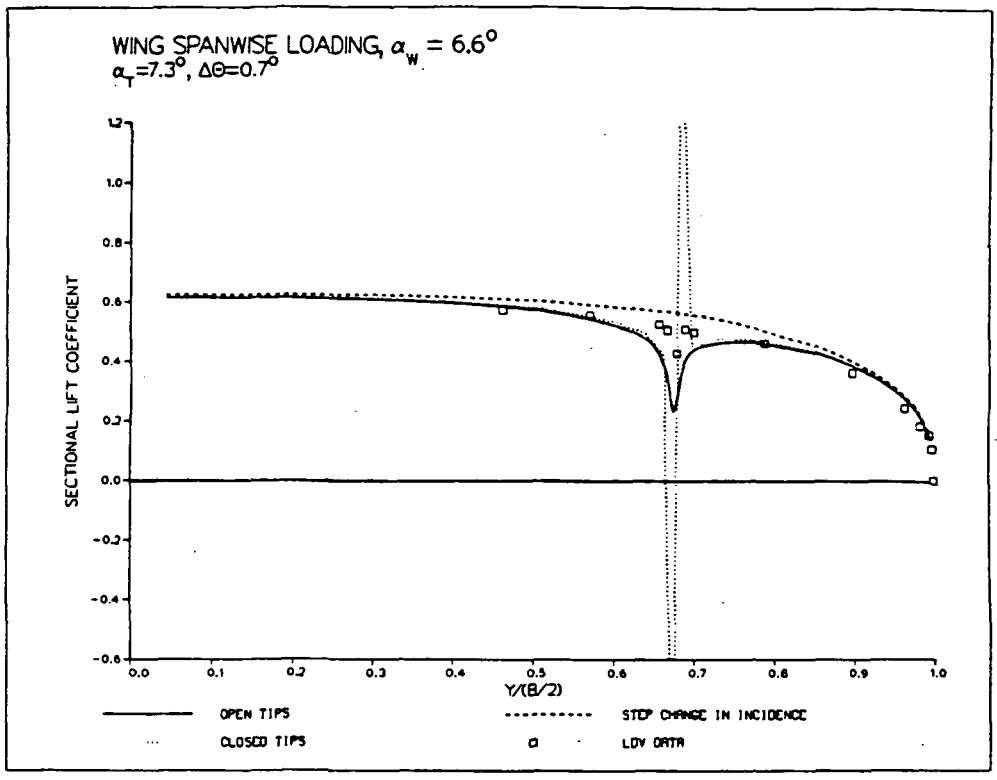

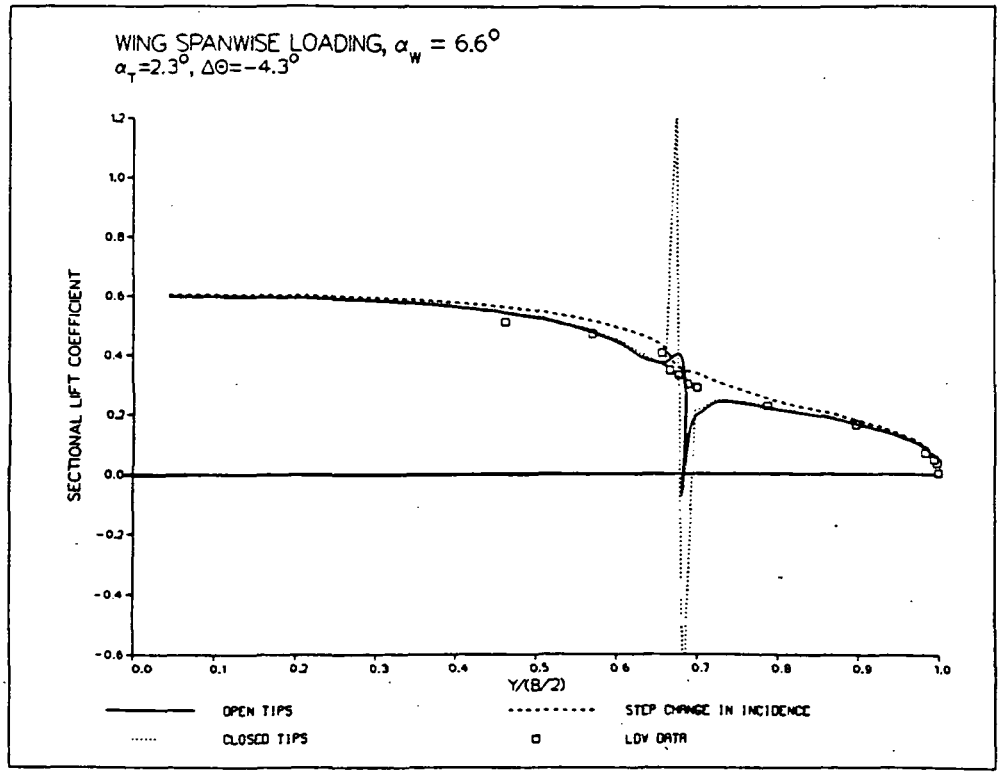

Figure 2.13: Spanwise loading correlation, $\Delta\theta$ = 0.70°, -4.3°

overpredicts the sectional lift, resulting in higher values of C_{L_T} as shown in Figures 2.8 and 2.11. The sudden spanwise drop in C_L for method 2 at Y/(B/2) = 0.68 is related to the structural discontinuity there. Since there is no surface to support a load and no singularity distribution over the gap, the lift must go to zero. These plots confirm that despite the marginal degree of correlation in the region near the gap, the open-tips method yields the best integrated tip lift coefficient for this lower range of $\Delta\theta$.

Figure 2.14 ($\Delta\theta$ = -8.7° and -12.4°) shows that as the incidence angle of the tip relative to the inboard wing increases, the singularity peaks at the gap decrease in magnitude. In fact, it appears that for large values of $\Delta\theta$, the closed-tips method would yield the best prediction of tip lift (Figure 2.14, $\Delta\theta$ = -12.4°). Overall, the step change in incidence method, selected for pitching moment prediction (Section 2.2), usually yields a more positive tip lift prediction than measured experimentally.

2.2.3 Drag Correlation

The purpose of this section is to evaluate the drag estimation capability of VSAERO. This is necessary to acquire an appreciation for drag related data and associated discussions presented throughout this report.

In the present application of the program (assuming attached flow for all lift coefficients), the code predicts the drag due to lift and the skin friction drag. Unfortunately, the version of

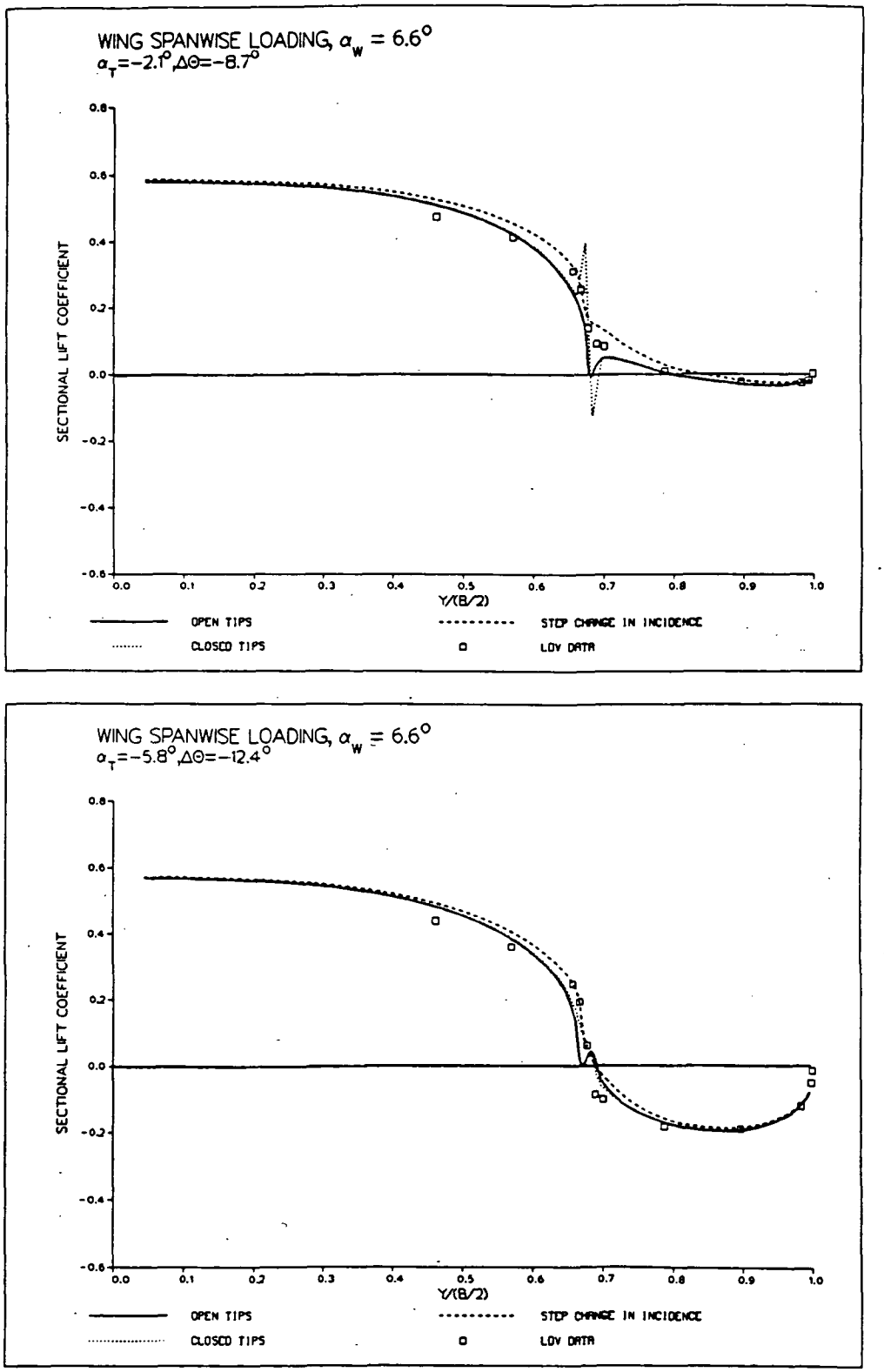

Figure 2.14: Spanwise loading correlation, $\Delta\theta$ = 8.7°, -12.4°

VSAERO available at NASA Ames during the spring of 1986 only printed out the skin friction drag as computed from the first iteration; this parameter was not updated in subsequent iterations.

Figure 2.15 shows the free-tip drag polars from VSAERO data only, experimental data, and a combination of VSAERO drag due to lift and skin friction drag predicted empirically. The configuration was modeled here as a continuous component with a step change in incidence angle at the tip. Observe from Figure 2.15 that the drag calculated by VSAERO only is highly underpredicted. As discussed in Section 2.2.1, this is believed to have a small effect on the correlation of pitching moment. The empirical relation used is based on the flat plate analogy and is given by (Reference 7) as

$$C_{D_{SF}} = C_F[1 + L(t/c) + 100\ (t/c)^4]R_{LS}S_{WET}/S_{REF} \qquad (2.2)$$

For the particular airfoil section used, L = 2.0 (maximum thickness point is not located beyond x/c = 0.30), and $R_{LS} \cong 1.0$ in incompressible flow. Fully developed turbulent flow was assumed. Figure 2.16 shows the same drag polars but with the configuration modeled as two separate components with open tips at the gap between the surfaces. Although this method seems to predict the lift characteristics with better accuracy, a comparison of Figures 2.15 and 2.16 indicates only a slight improvement in the drag variation with lift correlation. This improvement is more apparent for the TIP 1B polar at positive lift coefficients.

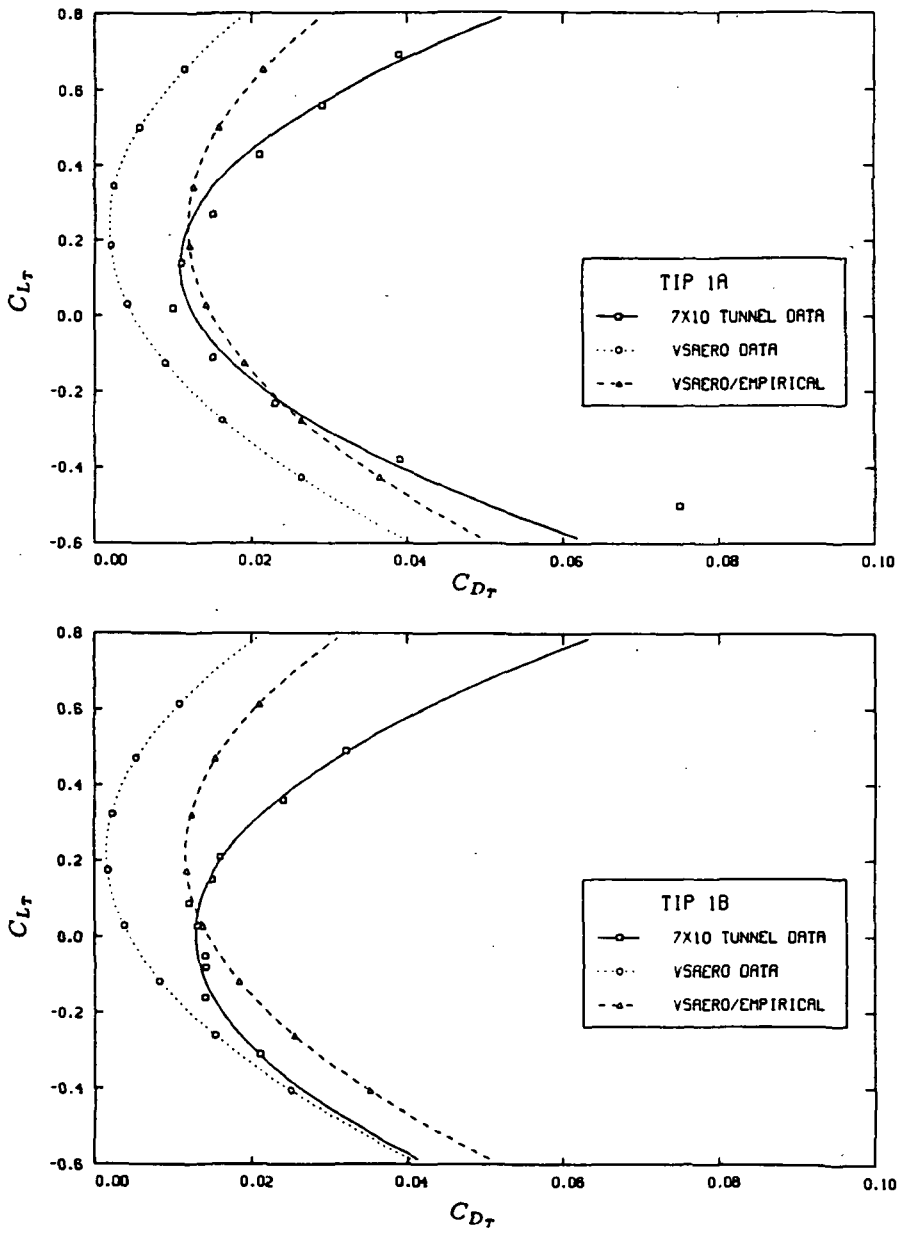

Re# = 0.867 million

Figure 2.15: Drag polar comparisons--single component, step change in incidence, $\Delta\theta = -5°$

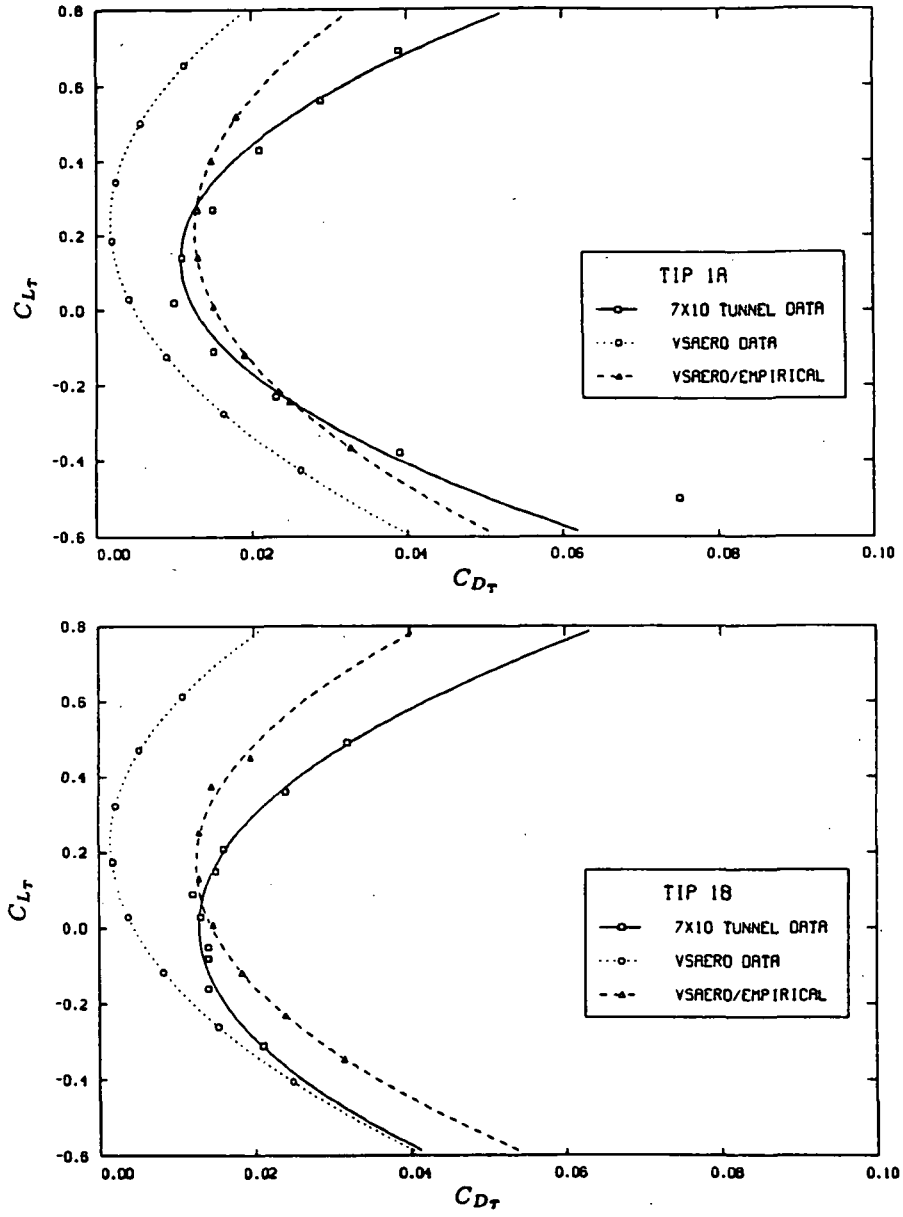

Reℓ = 0.867 million

Figure 2.16: Drag polar comparisons--separate components, open tips, $\Delta\theta$ = -5°

Obviously, the version of VSAERO which was used does not have the capability to predict total drag accurately. It is seen that when the empirically obtained drag component is added to the induced drag, the minimum drag values for both tips are in good agreement. Also notice that the shape of the two curves is essentially the same, but the tip C_L's at which minimum drag occurs do not correlate well: VSAERO seems to overpredict the minimum drag C_L in both cases. This could be related to interference effects which are not properly accounted for in the VSAERO model. Also, the empirical expression (Equation 2.2) is valid only for small incidence angles, thereby introducing more error at high angles of attack.

For obvious reasons, it was decided at this point that only the drag resulting from the streamwise component of the pressure coefficient acting on the panel area (i.e. drag due to lift) should be used from VSAERO output. In subsequent computations of total drag, the skin friction component computed by the empirical relationship will be added to the non-skin friction contribution of VSAERO.

As an illustration of this approach, consider the variation of total tip drag with lift coefficient squared. Figure 2.17 shows this relationship for both TIP 1A and TIP 1B. In both cases, the tip at negative incidence actually produces less drag than the undeflected tip ($\Delta\theta = 0.0$). This confirms the hypothesis of Reference 2, which stated that the upwash caused by the vortex shed at the wing/tip junction reduces the streamwise component of normal

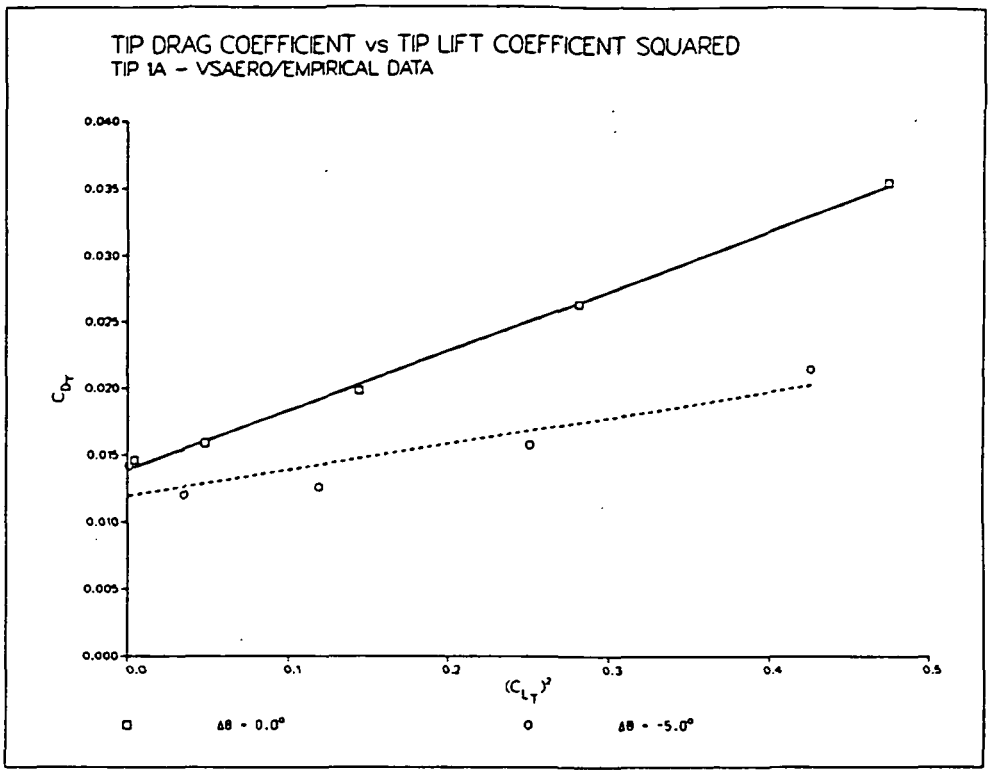

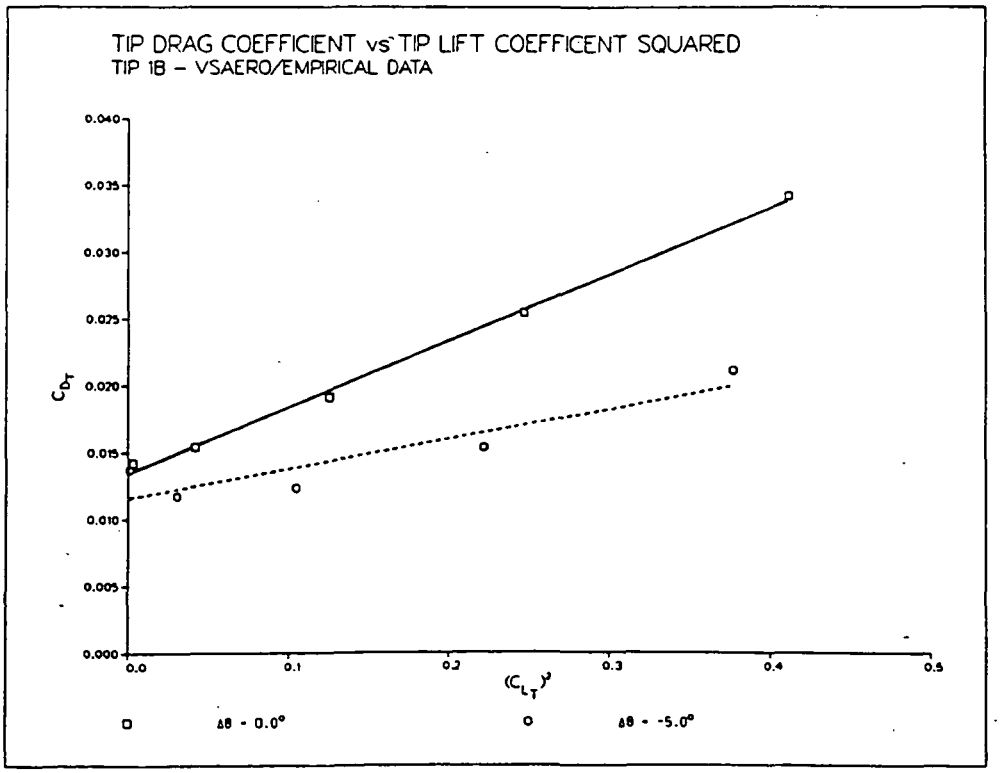

Figure 2.17: Variation of tip drag with lift--TIP 1A and TIP 1B

force at spanwise stations closest to the tip vortex, thereby reducing the total induced drag of the tip. This is one of the beneficial features of the free-tip concept and should result in a drop in the rotary wing power requirement. Note also that the predicted zero-lift C_D for both $\Delta\theta$s is the same, further supporting this theory.

2.3 VELOCITY VECTOR PLOTS

As shown by Equation (A.18) in Appendix A, the velocity at any point in the flow field may be computed by the VSAERO program. The user specifies points in 3-D space at which the velocity and pressure coefficient are to be calculated. With the three velocity components known at the specified points, a plotting routine can be used to obtain vector plots showing the projection of the resultant total velocity in a given plane. This approach can be used to visualize the development of tip vortices and determine the relative magnitude of the velocities induced by vortex flows. As will be shown in Chapter 3, the velocities induced by three-dimensional effects contribute to drag reduction in certain cases. Vector plot results could also be used in conjunction with experimental techniques for visualization of flow conditions.

The method consists of specifying "Velocity Scan Planes" which intersect the two surfaces under consideration and are perpendicular to the free stream velocity direction. In this case, eight planes were selected to analyze the flow over TIP 1A. The first plane is

located immediately ahead of the leading edge while the last is roughly one-third of a chord length behind the trailing edge. Figure 2.18 shows the location of the eight equally spaced planes. Note that they overlap the structural discontinuity of the semi-span wing and the outboard tip, which are the primary regions of interest. A total of 400 grid points were generated. Figure 2.18 also depicts the two cases which will be discussed.

Figure 2.19 shows the projected velocity vectors in the y-z plane for $\alpha_W = 12.0°$ and $\alpha_T = 2.0°$. The structural discontinuity is located at y = 65.02 cm, and the outboard tip at y = 95.77 cm. From the initial perturbations at the leading edge to the region aft of the trailing edge, the velocity vectors calculated from the distribution of singularities on the body and wake illustrate the development of the inboard and outboard vortices. Although the lifting surfaces are interacting, two distinct tip vortices are shed at the structural discontinuity; this has been confirmed by flow visualization studies performed during the January 1985 test. With both surfaces generating positive lift, the circulation in the tip vortices of both surfaces will be of opposite sign. The interaction of these two vortices depends on the respective loading of each surface. For example, when $\alpha_W = 12.0°$ and $\alpha_T = 2.0°$, the inboard wing tip vortex dominates the flow field around and aft of the gap (Figures 2.19, planes #6-#8). However, its effect on the outboard surface is reduced slightly due to the vortex of opposite strength shed by that surface.

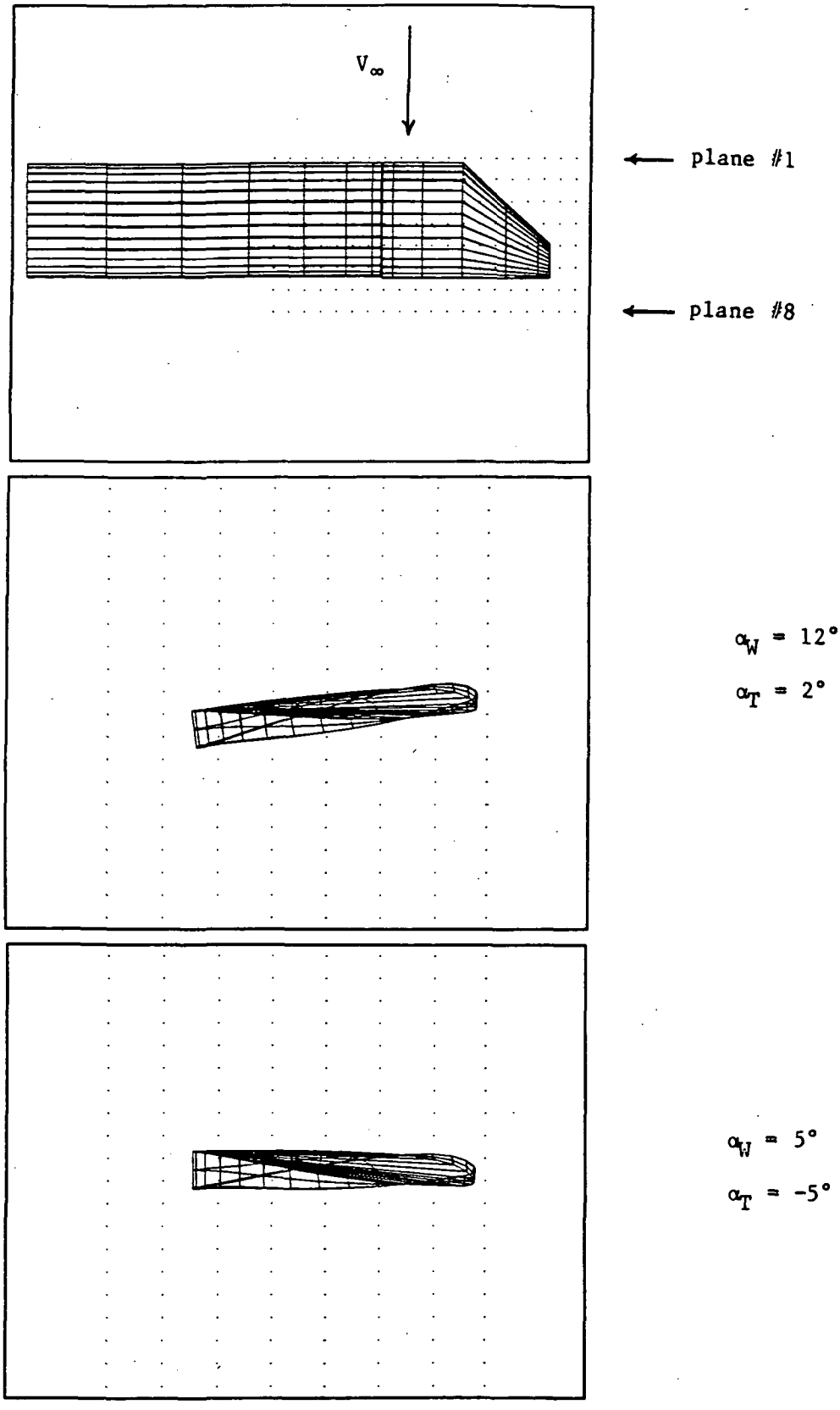

Figure 2.18: Velocity scan plane locations

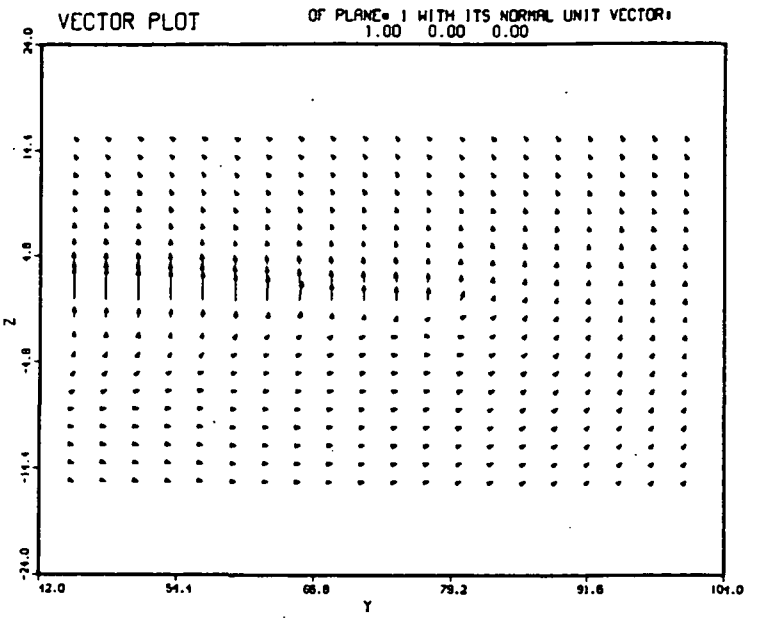

plane #1

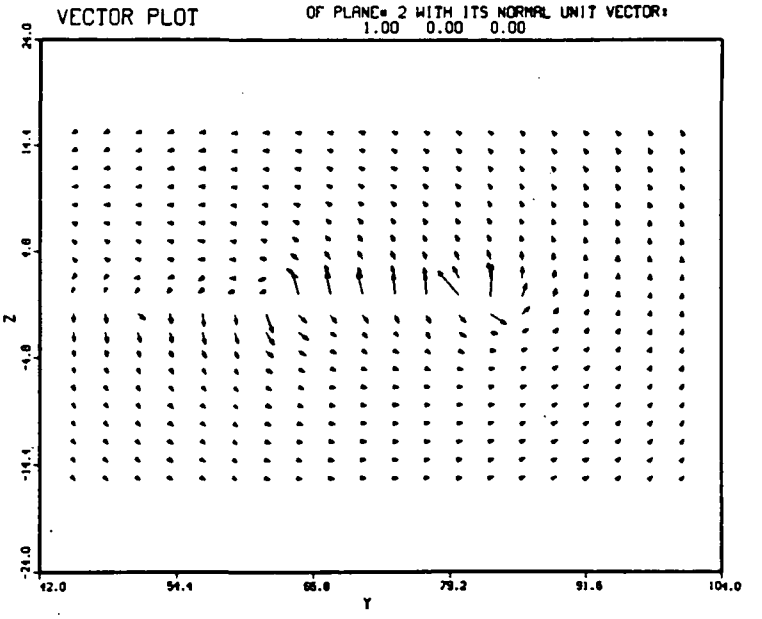

plane #2

Figure 2.19: Vector plots for TIP 1A, $\alpha_W = 12°$, $\alpha_T = 2°$ (continues)

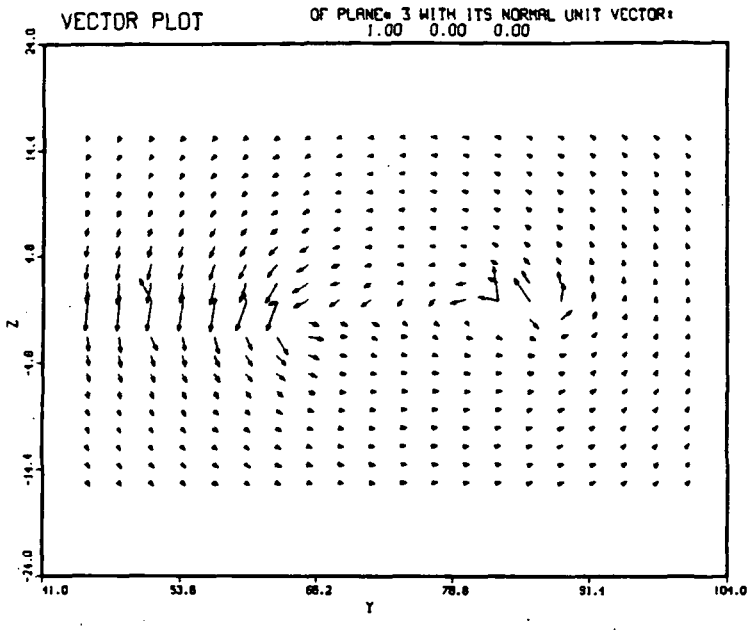

plane #3

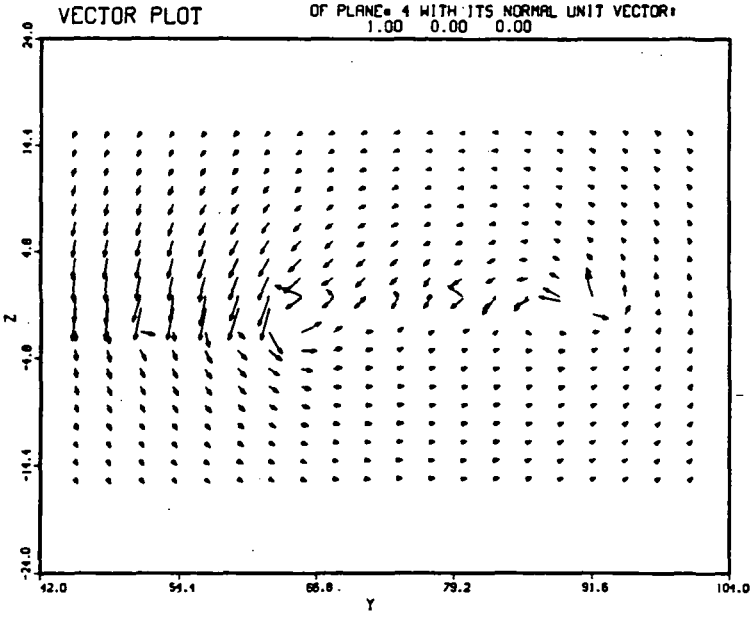

plane #4

Figure 2.19: Vector plots for TIP 1A, $\alpha_W = 12°$, $\alpha_T = 2°$ (continues)

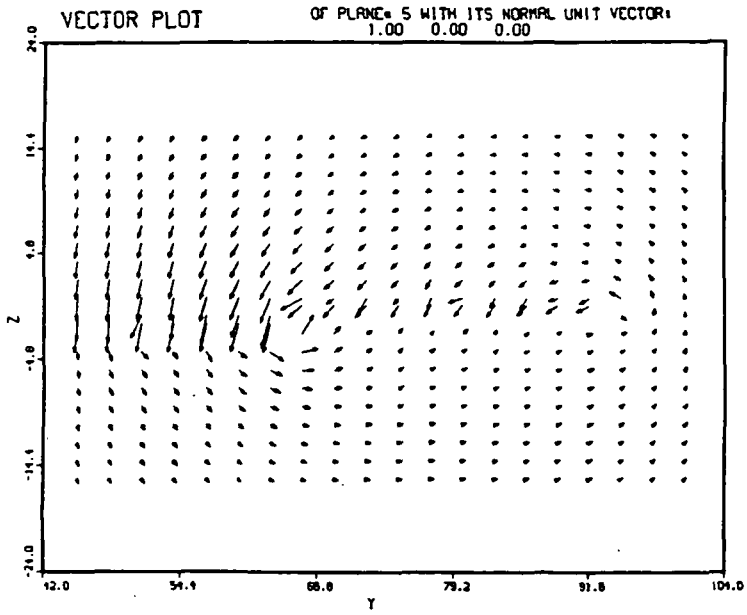

plane #5

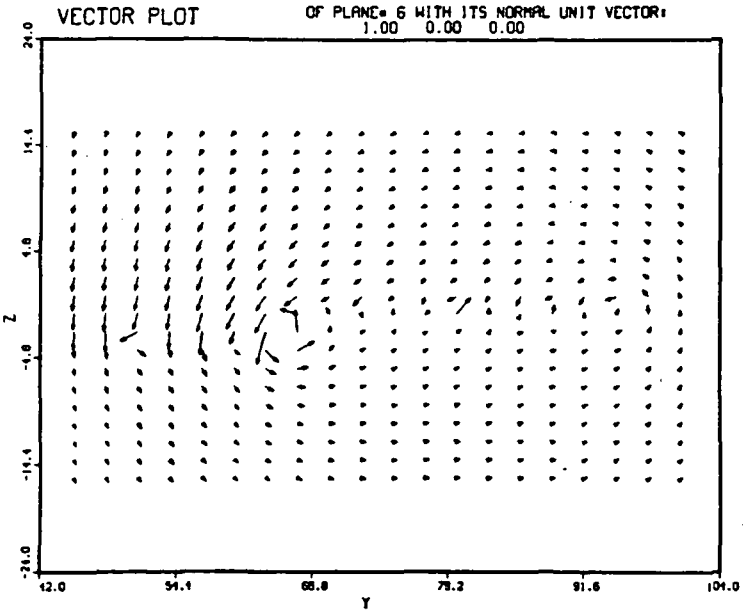

plane #6

Figure 2.19: Vector plots for TIP 1A, $\alpha_W = 12°$, $\alpha_T = 2°$ (continues)

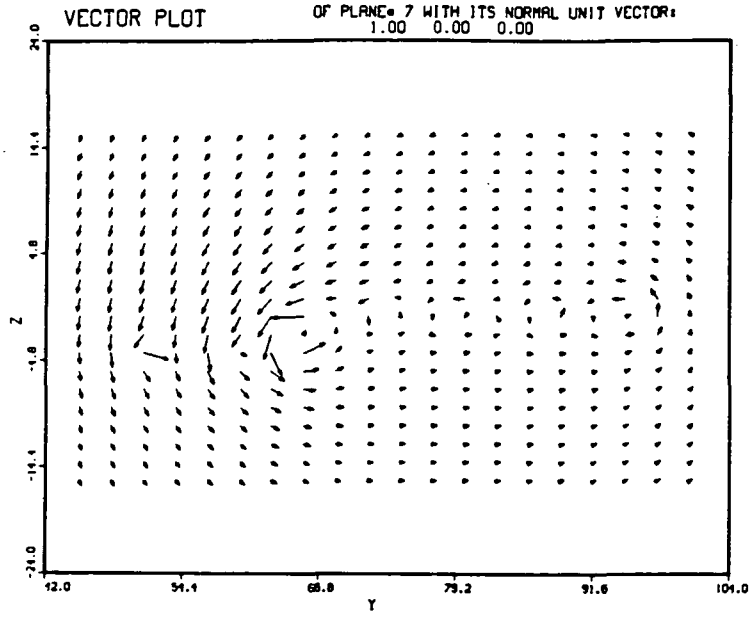

plane #7

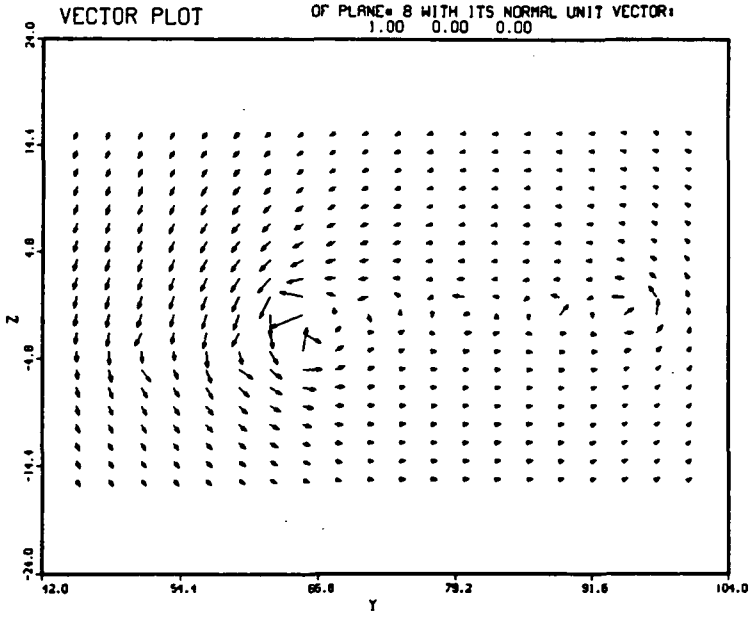

plane #8

Figure 2.19: Vector plots for TIP 1A, $\alpha_W = 12°$, $\alpha_T = 2°$ (concluded)

In the second case (Figure 2.20), the outboard tip section is producing negative lift, thus accounting for the clockwise direction of the circulation in the most outboard vortex (at y ≈ 95.8 cm). At the structural discontinuity though, the vortices will merge together, since the circulation in both of these is of the same sign. This is confirmed by the large magnitudes of the induced velocities at the lower surface of the outboard section (Figure 2.20, planes #4-#6, to the right of y = 65.02). These induced effects will be discussed more thoroughly in Section 3.3.1.

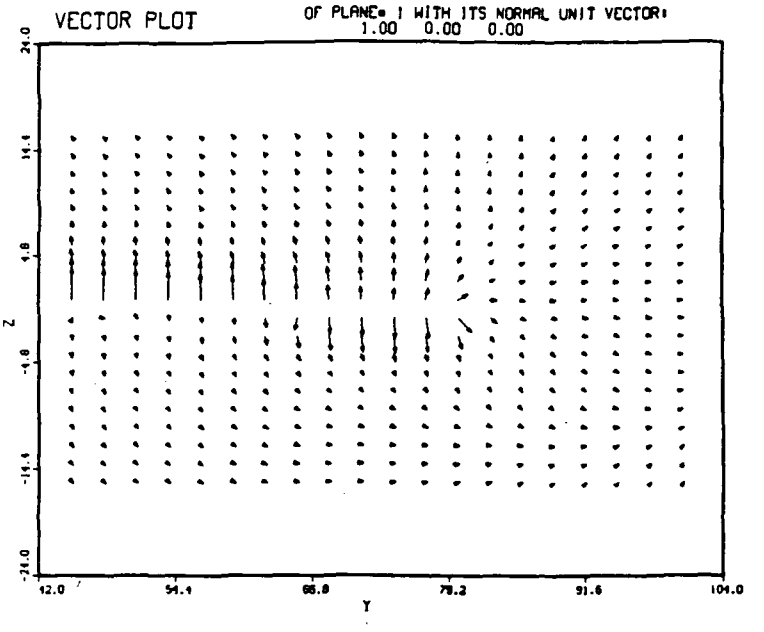

plane #1

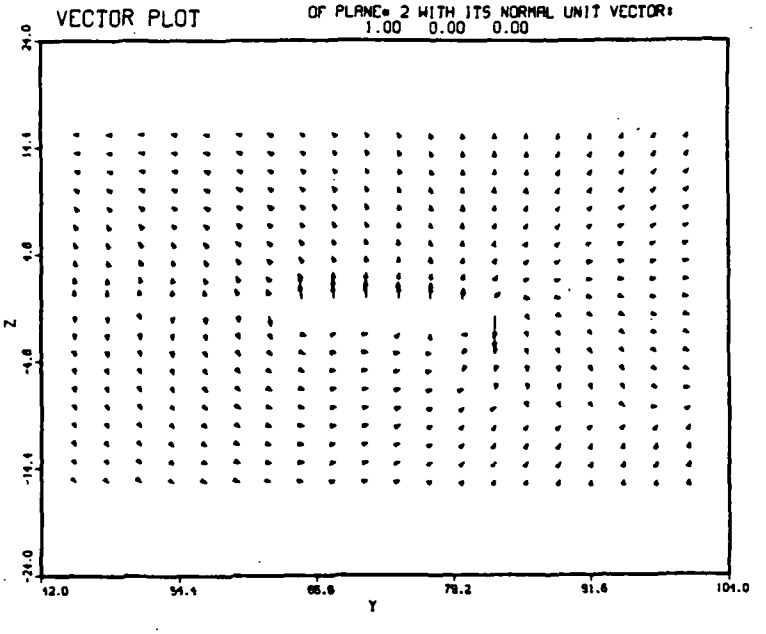

plane #2

Figure 2.20: Vector plots for TIP 1A, $\alpha_W = 5°$, $\alpha_T = -5°$ (continues)

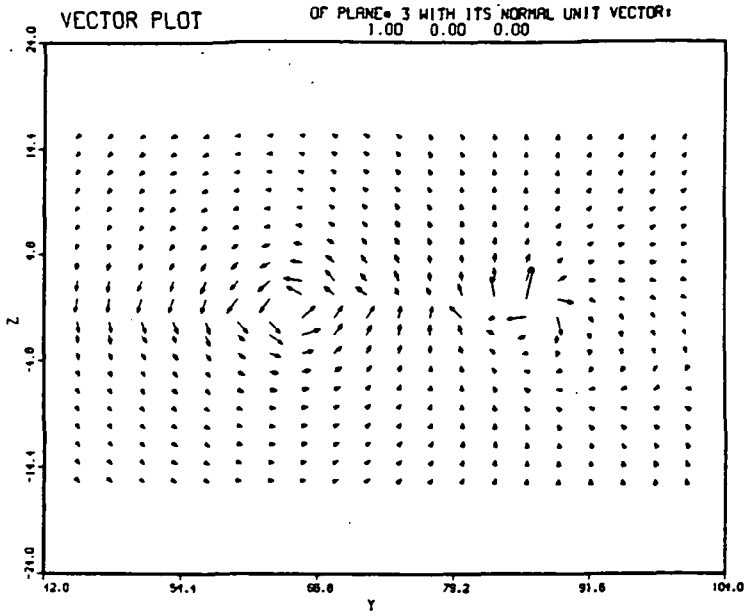

plane #3

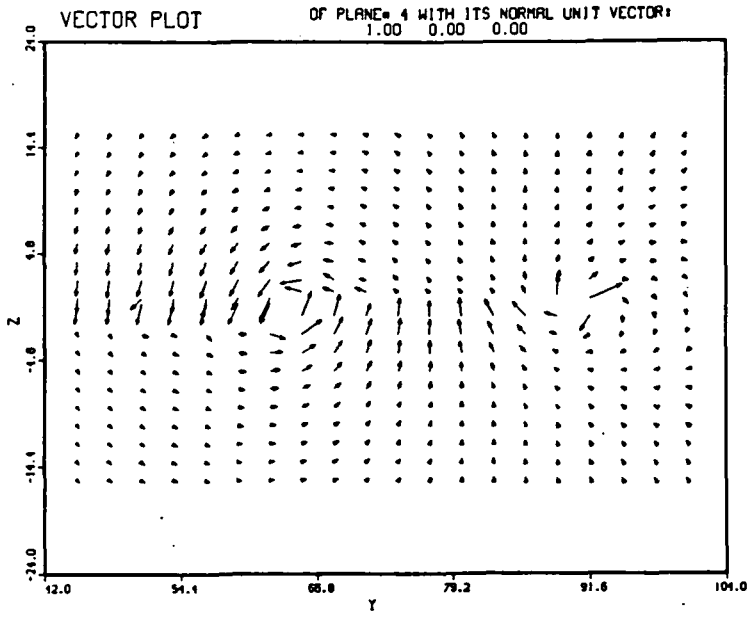

plane #4

Figure 2.20: Vector plots for TIP 1A, $\alpha_W = 5°$, $\alpha_T = -5°$ (continued)

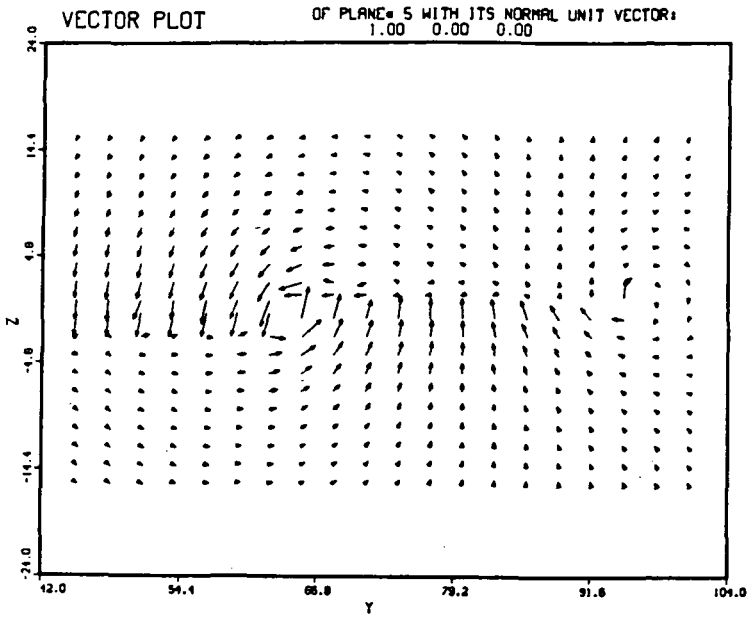

plane #5

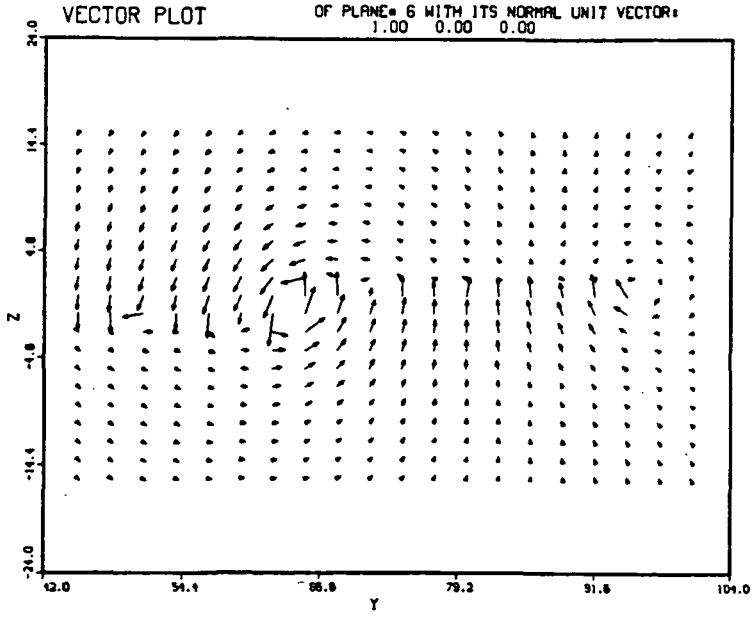

plane #6

Figure 2.20: Vector plots for TIP 1A, $\alpha_W = 5°$, $\alpha_T = -5°$ (continued)

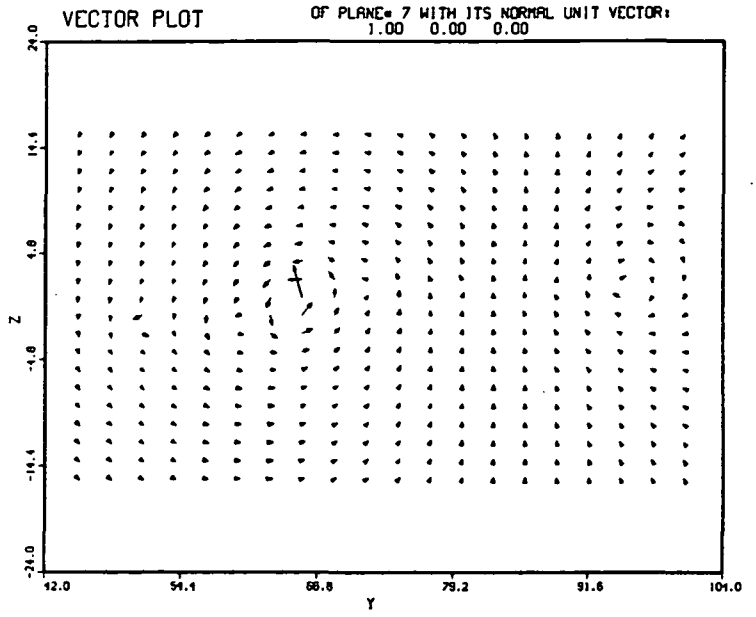

plane #7

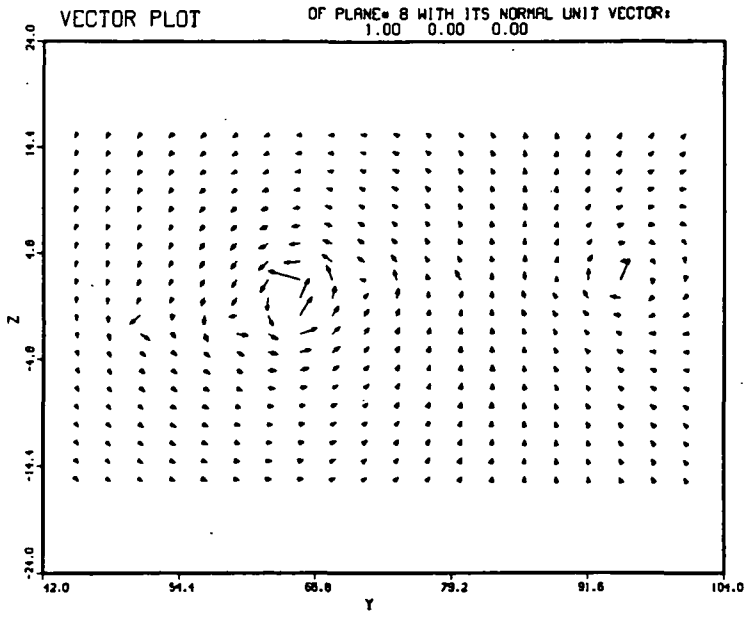

plane #8

Figure 2.20: Vector plots for TIP 1A, $\alpha_W = 5°$, $\alpha_T = -5°$ (concluded)

3. ANALYSIS OF NEW TIP PLANFORMS

The major objective of this phase of the research is to design and analyze new tip planform shapes for the free-tip. The emphasis in this process is on moving the aerodynamic center aft to improve the response of the free-tip to angle-of-attack variations. These new tip shapes are all related through a common inboard half. The quarter chord sweep angles as well as the taper ratios of the tips were varied, leading to the desired aerodynamic effects. The free-tip performance characteristics to be investigated are:

- pitching moment variation with angle of attack
- compressibility effects on C_{L_T} and C_{m_T} for representative subcritical Mach numbers
- sectional and surface aerodynamic center shift at high subsonic Mach numbers
- tip planform drag and its effect on the semi-span wing drag polars.

In this chapter, the computed values of C_{m_T} are normalized by the inboard wing chord (c_{INB}). As in Chapter 2, the moment reference point is the tip pitch axis, which coincides with the inboard wing quarter-chord line.

3.1 PITCHING MOMENT VARIATION OF THE NEW PLANFORMS

Table 3.1 lists the basic geometric characteristics of the new tip planforms. The details of the geometry are illustrated in

Table 3.1: Geometric Parameters of the New Tip Planforms

Note: c_{INB} = 20.80 cm (constant for all tips)
b_t = 2 × 15.373 = 30.746 cm (for all tips)

BASELINE

TIP 2

S_t = 521.987 cm^2
Outboard $\Lambda_{c/4}$ = 42°
λ = 0.26
Λ_{LE} = 10°; 50°
Λ_{TE} = 10°; 10°

TIP 3

S_t = 521.66 cm^2
Outboard $\Lambda_{c/4}$ = 37°
λ = 0.26
Λ_{LE} = 10°; 45°
Λ_{TE} = 10°; 0°

TIP 4

S_t = 521.52 cm^2
Outboard $\Lambda_{c/4}$ = 30°
λ = 0.26
Λ_{LE} = 10°; 40°
Λ_{TE} = 10°; -9.0°

TIP 5

S_t = 556.78 cm^2
Outboard $\Lambda_{c/4}$ = 28°
λ = 0.48
Λ_{LE} = 10°; 35°
Λ_{TE} = 10°; 0°

TIP 6

S_t = 537.913 cm^2
Outboard $\Lambda_{c/4}$ = 26°
λ = 0.36
Λ_{LE} = 10°; 35°
Λ_{TE} = 10°; -9.0°

Figure 3.1. The new tips are compared here to the old baseline configuration described in Chapter 2 (TIP 1A). A new baseline configuration [TIP 2, Figure 3.1(a)], which establishes the foundation on which the new planforms are based, was designed strictly on the requirement to increase the slope of the C_{m_T} vs α_T curve. Since the inertia properties of the free-tip and the torque output of the passive controller are unknown at this time (these are some of the parameters along with $(C_{m_\alpha})_T$ which appear in the equations of motion of the tip, Reference 3), tips with intermediate values of $(C_{m_\alpha})_T$ were designed. These might be useful to optimize future designs once all the relevant response characteristics are known. The incompressible pitching moment behavior of the new tips is compared to that of the old baseline configuration (TIP 1A) in Figure 3.2.

As may be observed, increasing the sweep angles and moving the aerodynamic center aft has clearly resulted in a negative increase in $(C_{m_\alpha})_T$. This obviously improves the response of the new tips to variations in local angle of attack or inflow. Table 3.2 lists the magnitudes of $(C_{m_\alpha})_T$ for the tips of Figure 3.2.

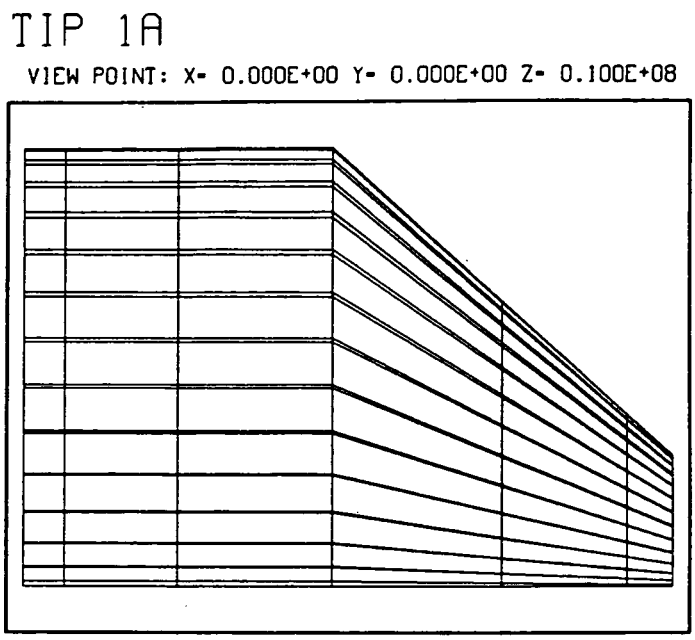

Old Baseline

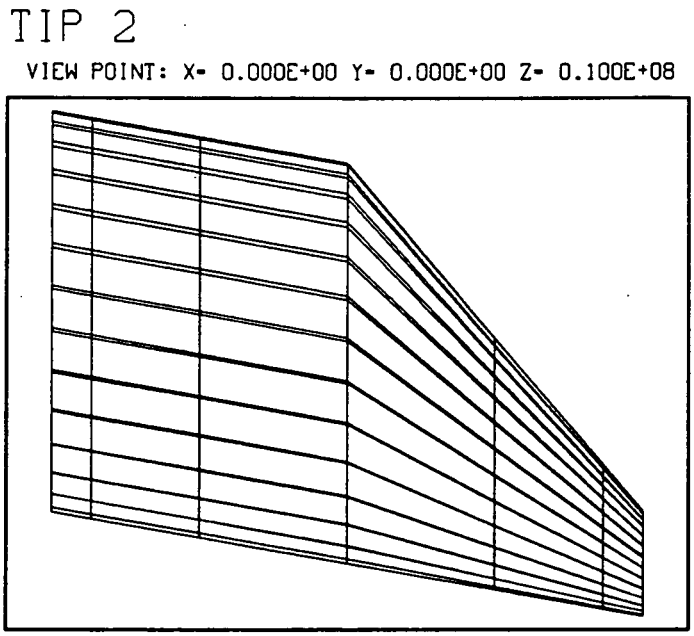

New Baseline

Figure 3.1: New tip planforms (continues)

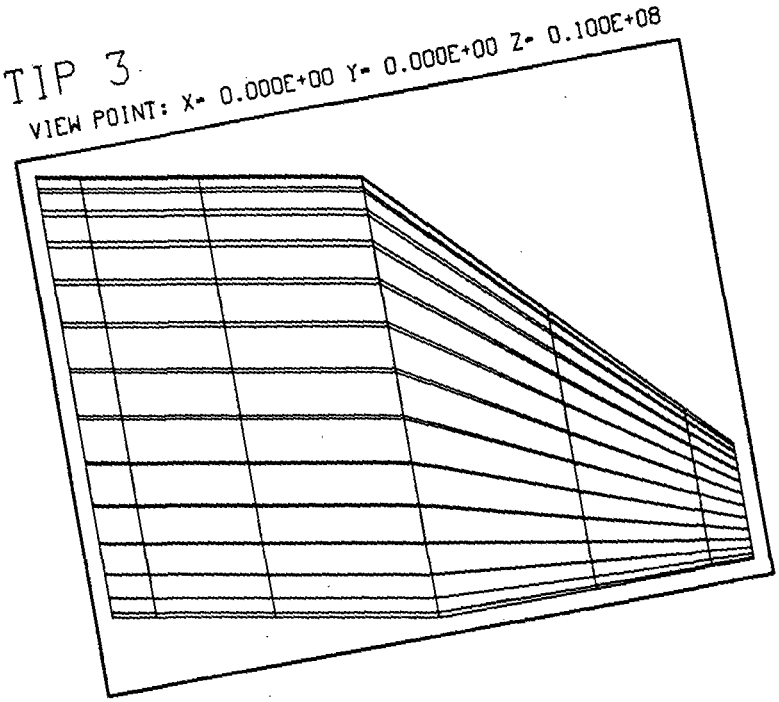

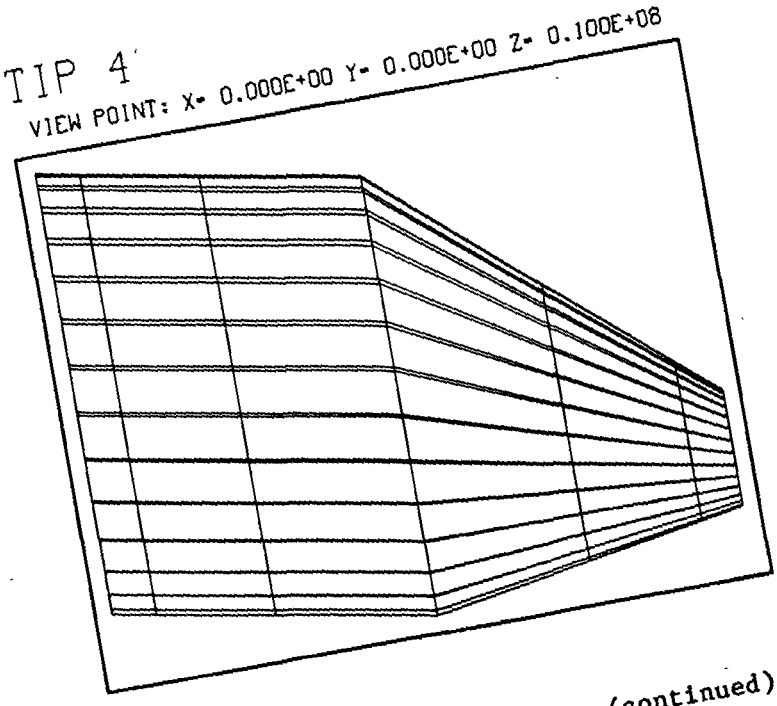

Figure 3.1: New tip planforms (continued)

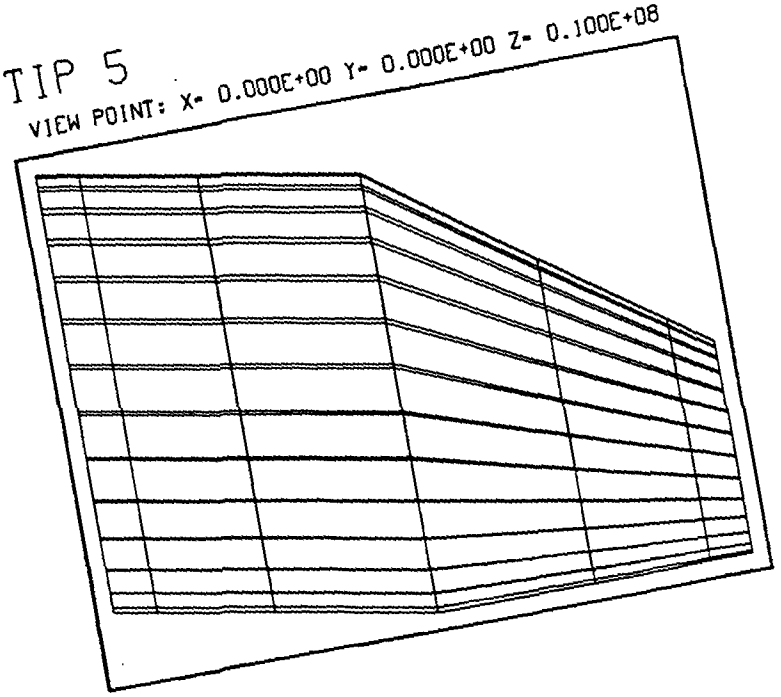

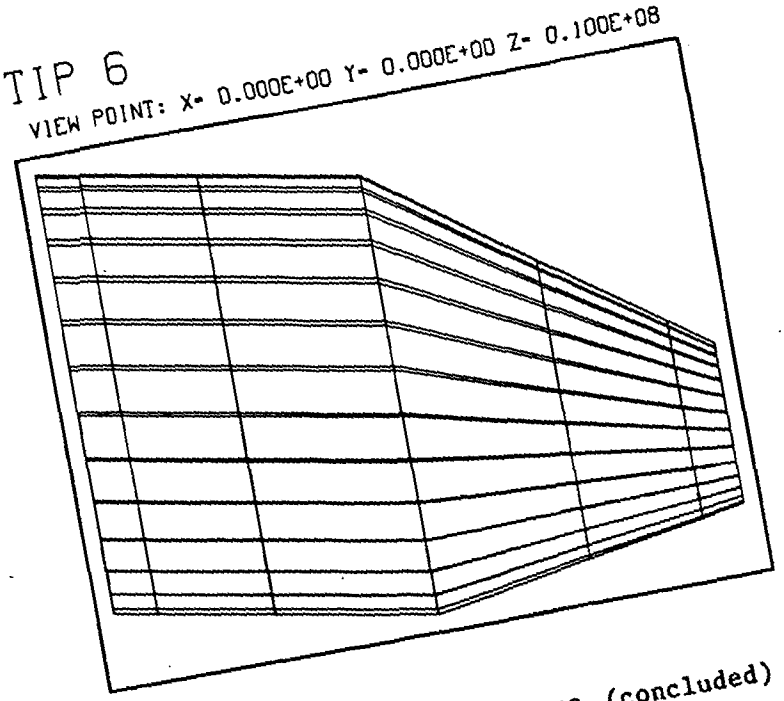

Figure 3.1: New tip planforms (concluded)

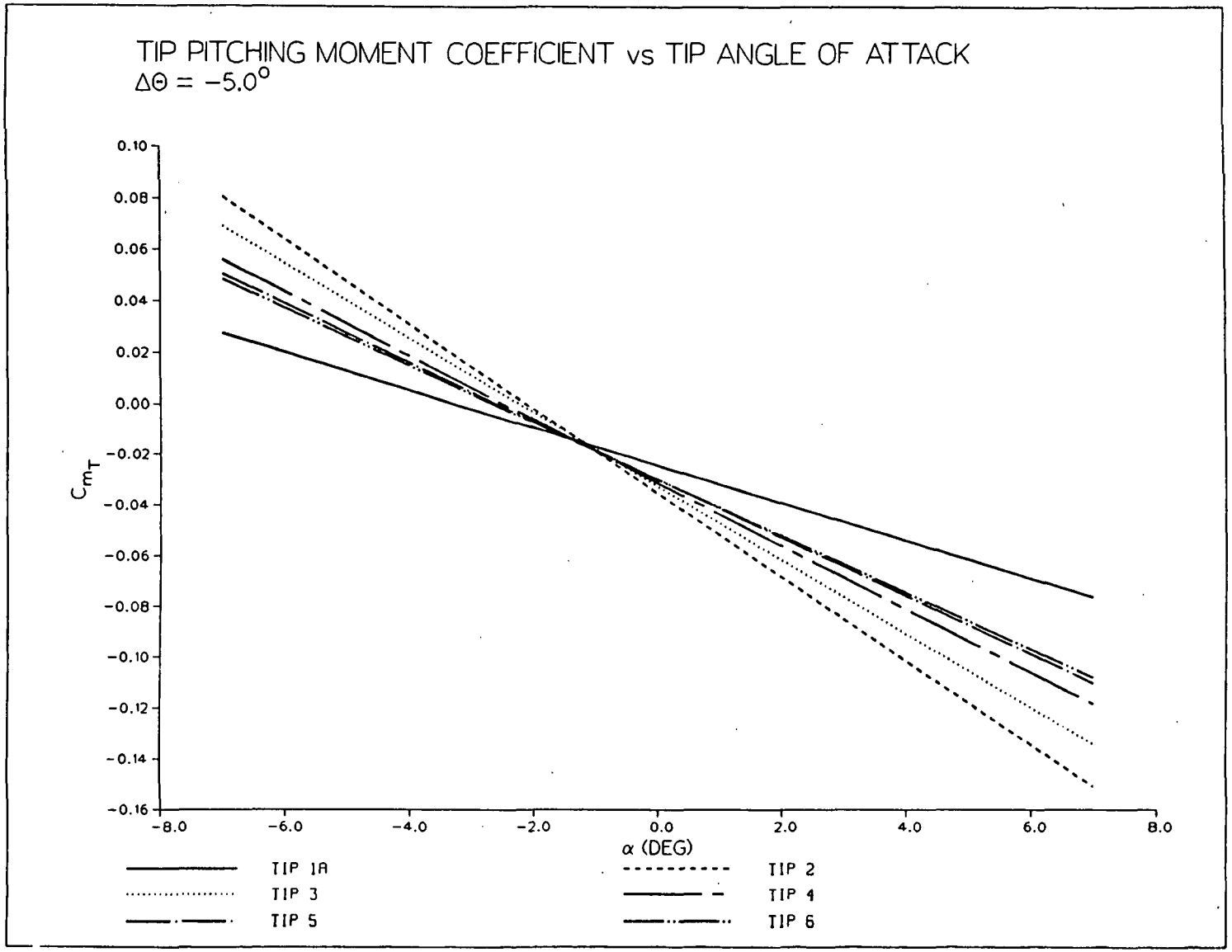

Figure 3.2: Comparison of pitching moment variation with angle of attack for new tip planforms

Table 3.2: Variation of Pitching Moment with Angle of Attack for New Free-Tip Planforms

Tip #	$(C_{m_\alpha})_T$ (deg^{-1})
1A (old baseline)	-0.0073
2 (new baseline)	-0.0165
3	-0.0145
4	-0.0125
5	-0.0115
6	-0.0111

It is seen that from the old baseline configuration to TIP 2, a 125% increase in $(C_{m_\alpha})_T$ has been achieved. Also, tips 3 through 6 provide a good range of intermediate values of this parameter. As stated earlier, these could be used for future designs. Because of the small difference in $(C_{m_\alpha})_T$ between tips 5 and 6, the former will be dropped from the analyses that follow in this report.

3.2 COMPRESSIBILITY EFFECTS

3.2.1 Prediction of Tip Lift and Pitching Moment Data

The installation of free-tips on the rotor blades of a helicopter should result in power and vibration reductions in forward flight. The highest tip Mach numbers are encountered at high advance ratios. It is therefore necessary to investigate the

performance of the decoupled tip of a semi-span wing at high Mach numbers, since prevailing compressibility effects will alter the aerodynamic characteristics of the tip. Unfortunately, the VSAERO program is a subsonic code and may therefore be used only for a combination of onset velocities and lift coefficients which do not produce shocks over the surface of the tip.

If the free-stream Mach number were increased above this range, shocks could form on the body upon local deceleration to subsonic flow. When the flow becomes supersonic locally and normal shocks form, flow separation is primarily due to the large adverse (and steep) pressure gradients associated with these shocks, and Reynolds number effects become secondary. VSAERO cannot predict this form of separation phenomena, since it cannot predict the formation of the shock itself; therefore, it is desirable to avoid these critical onset conditions. Note that for free-stream Mach numbers above the shock-free limit, VSAERO still yields continuous chordwise pressure distributions; but because flow separation is not predicted, the lift coefficients resulting from chordwise integration of C_p are overpredicted.

The method used in the code to account for compressibility effects is straightforward. After the pressure coefficient at the panel center has been determined for incompressible flow (see Appendix A, Equation A.22), it is corrected using a simple compressibility factor. For the cases discussed in this chapter, the Karman-Tsien option in the program was used. This relation is given by

$$(C_p)_{M_\infty} = \frac{(C_p)_{M_\infty=0}}{(1 - M_\infty^2)^{1/2} + [(M_\infty^2/[1 + (1 - M_\infty^2)^{1/2}])(C_p)_{M_\infty=0}]/2} \tag{3.1}$$

Note that for low M_∞, this expression is equivalent to the Prandtl-Glauert factor. Once the C_p at each panel has been corrected for compressibility, the chordwise and spanwise summations are carried out in the manner described in Appendix A.

In the study of shock-free compressibility effects, a realistic range of Mach number and tip C_L needs to be investigated. Figure 3.3, taken from Reference 2, illustrates the range of $\Delta\theta$ as a function of azimuth angle obtained from the first experimental test of a rotor equipped with free-tips. The largest contrast in aerodynamic effects for a helicopter in forward flight is found by comparing the $\psi = 90°$ (advancing side, highest tip Mach number) with the $\psi = 270°$ (retreating side, lowest tip Mach number). For this analysis, it will be assumed that at $\psi = 90°$, the pitch angle of the inboard blade at the structural discontinuity (R = 0.9) varies between 0° and 4°. At the $\psi = 270°$ position, the local pitch angle is assumed to vary between 10° and 12°. These are representative of the blade pitch at this radial location for typical advance ratios (Reference 8). Therefore, if these incidence angles are used for the semi-span wing inboard section, the equivalent tip angles of attack may be obtained from the $\Delta\theta$ values of Figure 3.3.

As discussed earlier, if a subsonic code such as VSAERO is used in this analysis, it is necessary to remain below free-stream Mach numbers and tip C_L's which lead to the formation of shocks. Two

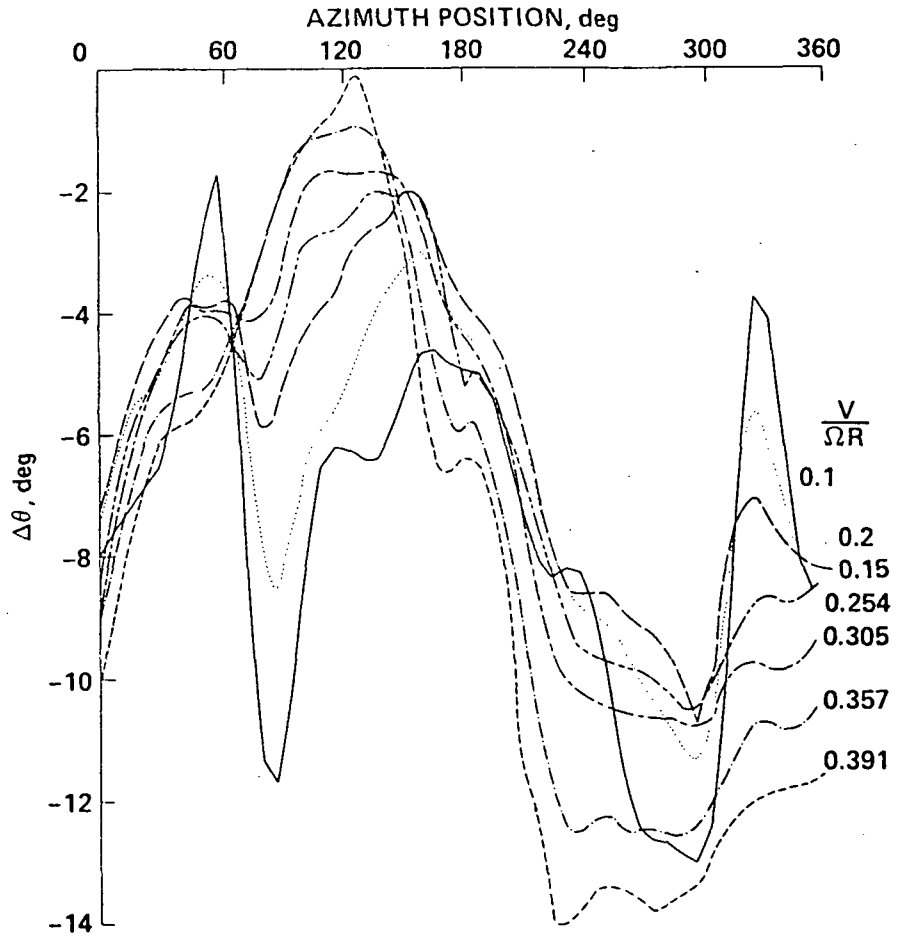

Figure 3.3: Variation of $\Delta\theta$ as a function of azimuth position and advance ratio (taken from Reference 2)

sources of data were used to ensure that compression shocks did not occur. The first consisted of checking the local Mach number on the upper and lower surfaces of the tip as predicted by VSAERO. The code computes the Mach number at panel centers as a function of corrected C_p values (for compressibility) and free-stream Mach number. The second involved the use of 2-D experimental data (Reference 9). For specified values of M_∞ and C_{ℓ_T}, these data were used to avoid lift coefficients in the nonlinear range. In an attempt to compare the differences between typical advancing and retreating side values of tip Mach number for a small-scale rotor, two cases were considered, $M_\infty = 0.49$ and $M_\infty = 0.70$. The method used to generate the values of C_{L_T} and C_{m_T} is described in Appendix B.

After several attempts in identifying the highest possible combinations of M_∞ and C_{L_T}, it was found that the critical case occurred at $M_\infty = 0.49$ on the inboard portion of the semi-span wing. At $M_\infty = 0.49$, there still is a good safety margin away from nonlinear effects for the tip region. The final combination of parameters which yield the shock-free flow over the entire semi-span wing at $M_\infty = 0.70$ and $M_\infty = 0.49$ are listed in Table 3.3.

Table 3.3: Combinations of Pitch Angles for Shock-Free Flow at the Selected Free-Stream Onset Velocities

Advancing side: $M_\infty = 0.70$
$0.0 < \alpha_W < 4.0$, $\alpha_T = -8.0°, -5.0°, -2.0°$
Retreating side: $M_\infty = 0.49$
$8.0 < \alpha_W < 12.0$, $\alpha_T = -14.0°, -11.0°, -8.0°$

Note that the test RPM and geometry of the rotor used in the tests of Reference 2 were used to evaluate the related Mach numbers in the tip region on the advancing and retreating sides. Tip Mach numbers of 0.70 and 0.49 correspond to an advance ratio of $\mu = 0.176$ for the small-scale rotor in the wind tunnel. Since only the critical cases (with respect to VSAERO capabilities) were of interest in this study, Mach numbers which would correspond to lower values of μ were not considered. Also, it was found later that the limits of Table 3.3 did not change with respect to the various tip planforms considered; therefore, these incidence angles are valid for all of the planforms of Figure 3.1 at the pre-selected limit Mach numbers ($M_\infty = 0.70, 0.49$).

Despite the precautions listed in the previous paragraphs, flow separation can still occur due to Reynolds number effects. Since previous attempts to stitch the wake on the lower surface of the tip failed, the separation line was specified at the trailing edge for all cases. If values of C_{L_T} and C_{m_T} in the nonlinear range (i.e. with partially separated flow) had been sought, an exhaustive iterative procedure would have been initiated. This would have required accurate specification of the predicted separation line, based on output from the boundary layer routine. The data completed for cases where separated flow is observed thus result from a first estimate only. These were not obtained from converged solutions, and are presented to verify trends only. The predicted values of C_{L_T} and C_{m_T} for the conditions listed in Table 3.3 are tabulated in Appendix C.

Table 3.4 lists the low angle of attack lift and pitching moment slopes for tips 2, 3, 4, and 6 calculated from the data in Appendix C. Only values of C_{L_T} and C_{m_T} which fell in the linear range were used to estimate C_{L_α} and C_{m_α} of the tip. These are compared to the computed values in incompressible flow. The following observations can be made:

First, note that the incompressible lift curve slopes $(C_{L_\alpha})_T$ are higher than would be expected for such a low aspect ratio lifting surface ($A_T \approx 1.80$). This is consistent with the results obtained for the step change in incidence method (see Section 2.2.1) which was used here to obtain better $(C_{m_\alpha})_T$ predictions. Increases in $(C_{L_\alpha})_T$ more closely agree with the Prandtl-Glauert factor for $M_\infty = 0.49$. The larger deviation at $M_\infty = 0.70$ is expected, since experimental data show that the Prandtl-Glauert law may overpredict C_{L_α} at higher subsonic Mah numbers (Reference 10).

Comparison of the % increase in $(C_{m_\alpha})_T$ from $M_\infty = 0$ to 0.49 and from $M_\infty = 0.49$ to 0.7 shows that compressibility effects are more pronounced on the pitching moment slope $(C_{m_\alpha})_T$ at $M_\infty = 0.70$. This can be partially attributed to the aft shift in aerodynamic center with Mach number. When the total moment is computed, the resultant lift acting at the A.C. has increased due to compressibility, but so has the moment arm to the reference point (the shaft pitch axis in this case). However, at $M_\infty = 0.49$, $(C_{m_\alpha})_T$ does not increase as much. In fact, the increase closely follows that of the tip lift curve slope, $(C_{L_\alpha})_T$, indicating that no shift in the A.C. has

Table 3.4: Compressible Lift and Pitching Moment Slopes (Linear Range)

Note: (1) Average values for three $\Delta\theta$s are listed (see Appendix C).

(2) At $M_\infty = 0.70$, Prandtl-Glauert factor: 1.40. Re# = 3.39×10^6

At $M_\infty = 0.49$, Prandtl-Glauert factor: 1.15. Re# = 2.42×10^6

		$(C_{L_\alpha})_T$ (deg^{-1})	Increase from $M_\infty = 0.0$	$(C_{m_\alpha})_T$ (deg^{-1})	Increase from $M_\infty = 0.0$	$\frac{\Delta c}{c_{INB}} = \frac{(C_{m_\alpha})_T}{(C_{L_\alpha})_T}$
TIP 2	M = 0.0	0.0796	--	-0.0165	--	0.207
	M = 0.49	0.0947	19.0%	-0.0192	16.4%	0.203
	M = 0.70	0.1031	29.5%	-0.0242	46.7%	0.235
TIP 3	M = 0.0	0.0822	--	-0.0145	--	0.176
	M = 0.49	0.0954	16.1%	-0.0168	15.9%	0.176
	M = 0.70	0.1047	27.4%	-0.0211	45.5%	0.202
TIP 4	M = 0.0	0.0791	--	-0.0125	--	0.158
	M = 0.49	0.0940	18.8%	-0.0149	19.2%	0.159
	M = 0.70	0.1034	30.7%	-0.0182	45.6%	0.176
TIP 6	M = 0.0	0.0781	--	-0.0111	--	0.142
	M = 0.49	0.0919	17.7%	-0.0127	14.4%	0.138
	M = 0.70	0.1021	30.7%	-0.0166	49.5%	0.163

occurred. This is confirmed by the A.C. locations on the right hand column of Table 3.4 calculated from the lift and pitching moment slopes. When $M_\infty \approx 0.50$, the position of the A.C. is still very close to its incompressible location. As will be shown in the next section, the sectional A.C. moves aft somewhere between $M_\infty = 0.5$ and $M_\infty = 0.7$.

Because of the difference in $(C_{m_\alpha})_T$, a large difference in tip response between the $\psi = 90°$ and $\psi = 270°$ azimuthal positions can be expected. The average increase for the four tips is 26% at $\mu = 0.176$, for a small-scale rotor (Reference 2).

No particular tip seems to have a larger increase in $(C_{m_\alpha})_T$ (compared to the incompressible case) than another at the same Mach number. The percentages in increase of $(C_{m_\alpha})_T$ are all within about 5% of each other. Any variations in the increase of this parameter may be related to uncertainties associated with slope estimation.

3.2.2 Sectional Aerodynamic Center Shift

The sectional aerodynamic center location is computed by using a relation derived from the sum of the moments about an arbitrary point on the section chord. With the reference point at the quarter chord of the section and since by definition, $dC_{m_{ac}}/d\alpha = 0$, the following expression can be obtained:

$$x_{ac}/c = 0.25 - dC_m/dC_\ell|_{0.25c} \qquad (3.2)$$

Since the VSAERO program computes the sectional lift and pitching moment about the quarter chord at each user-defined spanwise column, the slope $dC_m/dC_\ell|_{0.25c}$ can be easily obtained for a specified Mach number. The results for Mach numbers up to M_∞ = 0.80 are shown in Figure 3.4. Using TIP 6 as an example, the computations were carried out at the two span stations indicated at the top of the figure. To maintain shock-free flow, only values of sectional lift coefficient between 0.10 and 0.25 were used to compute x_{ac}/c. Although the flows here are highly three-dimensional, qualitative comparisons with 2-D experimental results can be made. The data of Figure 3.5, taken from Reference 9, illustrate the shift in aerodynamic center as a function of free stream Mach number for the V23010 airfoil. At both span locations, the trends of Figure 3.4 are similar to those observed in Figure 3.5. The forward travel of the A.C. around M_∞ = 0.60 to 0.65 is not as significant as observed from the experimental data ($\approx$ 3.4% of the chord); however, the Mach number at which the A.C. begins its aft shift matches the 2-D value quite well. Due to the limitations of the theoretical model, which is incapable of predicting shocks and their effects on pressure distribution, the data predicted by VSAERO are unreliable beyond M_∞ = 0.72.

Figure 3.4 also confirms that the computed results are in agreement with the theory of finite aspect ratio wings. The following relation, taken from Reference 11, yields the sectional aerodynamic center location for an assumed wing loading function:

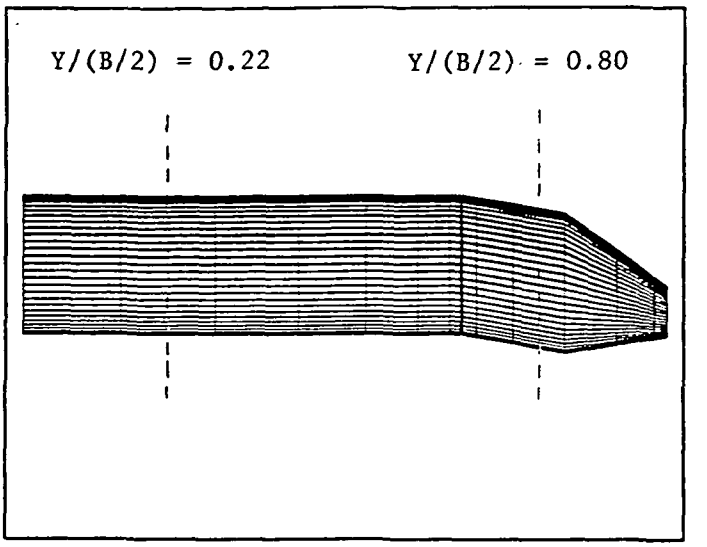

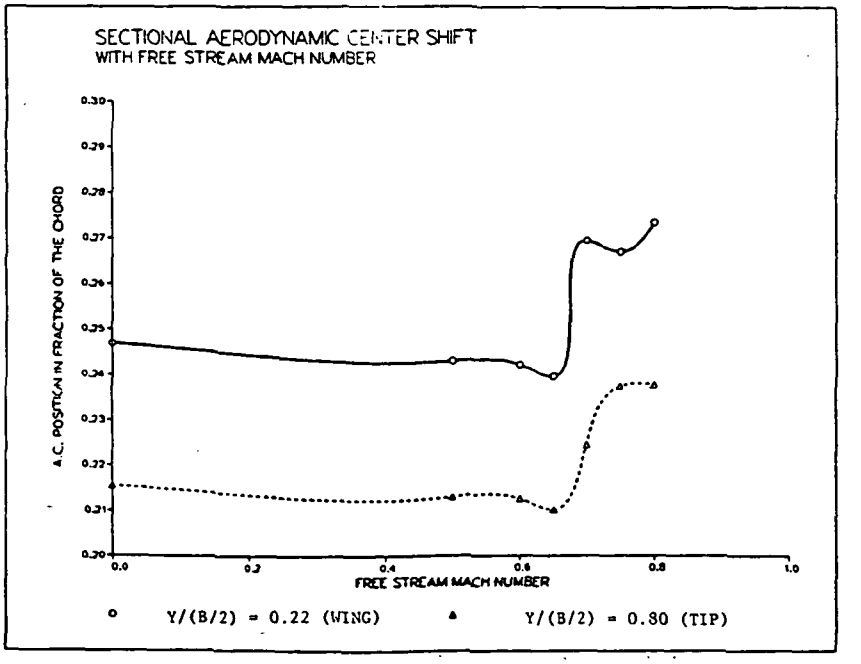

Figure 3.4: Compressibility effects on sectional aerodynamic center location, V23010 airfoil--VSAERO data

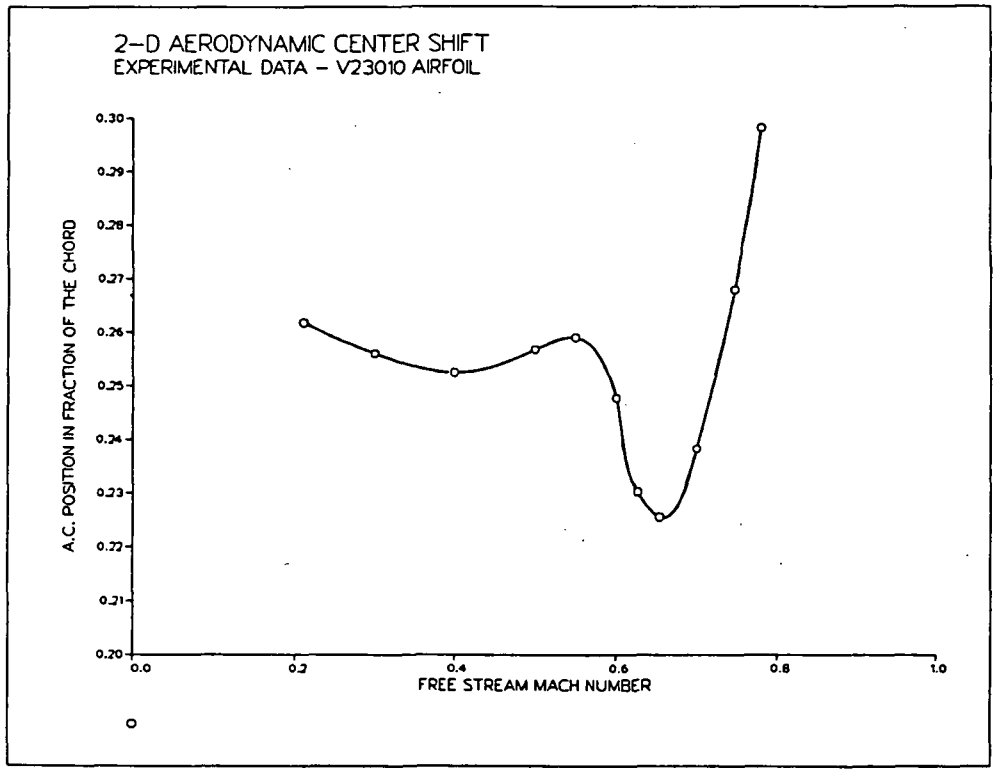

Figure 3.5: Compressibility effects on aerodynamic center location, V23010 airfoil--experimental data taken from Reference 9

$$x_{ac}/c = 1/2(1 - n) \qquad (3.3)$$

The parameter "n" is a function of aspect ratio: the value n = 1/2 represents the limit $A \to \infty$, and the limit $n \to 1$ represents the case where A = 0. As the data from Figure 3.4 for $M_\infty = 0$ indicate, the sectional A.C. of the inboard wing is in the vicinity of the quarter chord. Because symmetry about the wing root was assumed in this case, the inboard portion behaves as a high aspect ratio wing, and the predicted A.C. location in incompressible flow is in good agreement with Equation (3.3). The theory also predicts that for low aspect ratio wings, the sectional A.C. moves towards the leading edge. The computed data at $M_\infty = 0$ confirm that this occurs here also, because of the three-dimensionality of the flow in the tip region.

Figure 3.6 illustrates sectional chordwise pressure distributions at $M_\infty = 0.0$, 0.6, and 0.7. Note that these C_p distributions are plotted for the same sectional lift coefficient; the span stations correspond to those where the aerodynamic center locations were evaluated. The shifts in aerodynamic center location observed in Figure 3.4 between $M_\infty = 0.0$ and $M_\infty = 0.70$ are of the order of 1-2% of the chord length. This finding is correlated by the data of Figure 3.5 at $M_\infty = 0.60$ and 0.70, where the peak C_p values have moved aft slightly. This can be observed also by comparing the steep negative increases in C_p at the leading edge. These portions of the curves for $M_\infty = 0.60$ and 0.70 are aft of the solid line (incompressible flow). Since the sectional C_ℓ is

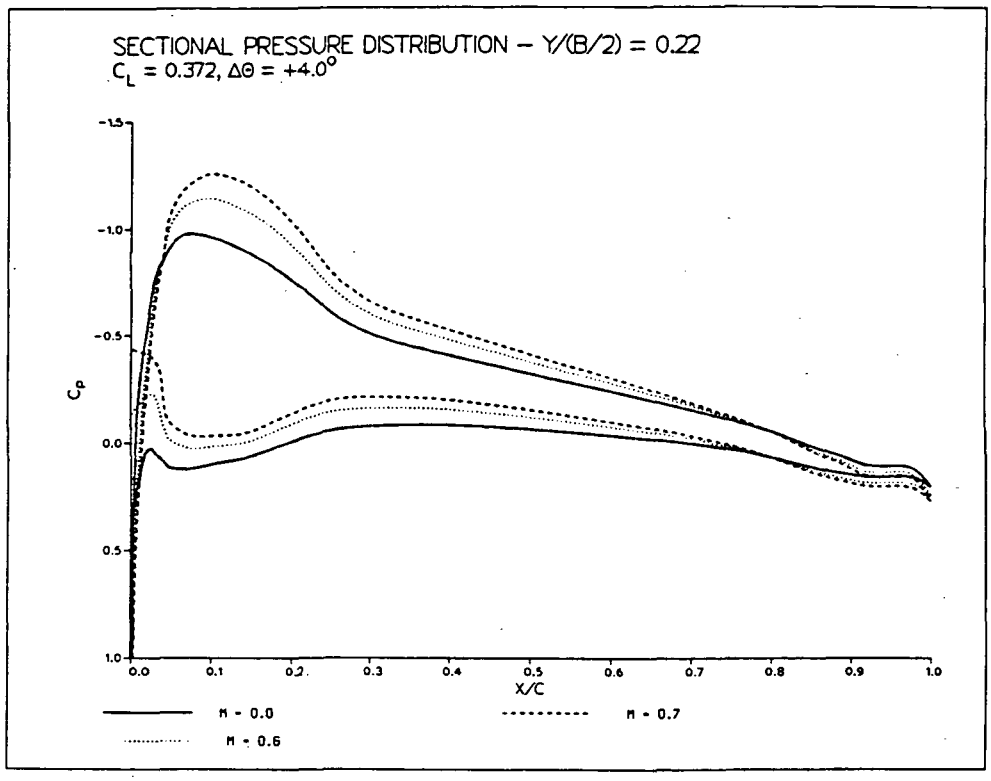

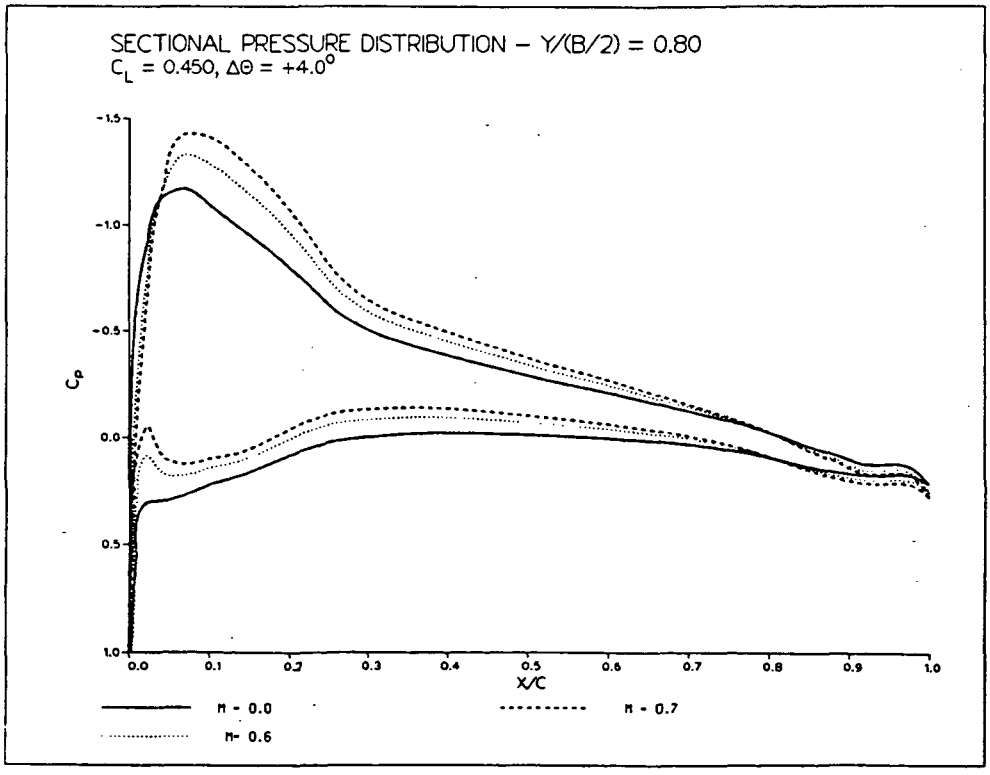

Figure 3.6: Compressibility effects on sectional pressure distribution, V23010 airfoil--VSAERO data

constant for all three Mach numbers, this aft shift in the loading (along with an increase in $C_{m_{ac}}$) accounts for the negative increase in pitching moment. Also, notice that as M_∞ is increased, the gradients in C_p are steeper aft of the upper surface pressure peaks. This is where shocks would most likely occur if the sectional loading were increased. The small peaks in C_p on the lower surface at the leading edge are probably associated with the drooped nose of the V23010 airfoil. The undeflected trailing edge tab produces the flat C_p distribution over the last 10% of the chord.

The position of the A.C. of a three-dimensional surface is defined as the weighted average of the sectional aerodynamic center locations as follows:

$$X_{AC} = \frac{\int_{-b/2}^{b/2} c_{\ell_a} c x_{ac} dy}{\int_{-b/2}^{b/2} c_{\ell_a} c dy} \tag{3.4}$$

where C_{ℓ_a} is the sectional lift coefficient due to the local angle of attack, c is the local chord length, and b is the lifting surface span. In Table 3.4, the surface A.C. locations as a fraction of the inboard wing chord are listed. By comparing the 3-D shifts between M_∞ = 0.5 and 0.7, it can be seen that the A.C. travels aft by 1.7 to 3.2% of the inboard wing chord length for the four tips shown. This seems to be reasonable in view of the calculated sectional AC shift for TIP 6.

The data presented in this section were obtained through the use of the maximum capabilities of the VSAERO code in compressible flow analysis. Because of the limitations of subsonic lifting surface theory and the approximation of compressibility effects, some uncertainty is associated with these results. In addition, many of the predicted parameters only have limited ranges of application. For example, the $(C_{L_\alpha})_T$ and $(C_{m_\alpha})_T$ slopes of Table 3.4 are valid only for a small range of tip angles of attack or lift coefficients. Nonetheless, the computed data show good consistency with sectional and three-dimensional compressible flow theory. These results can be taken into account in the design process of tip planforms for the free-tip rotor.

3.3 DRAG POLARS OF NEW TIP DESIGNS

The drag of a semi-span wing with a structurally decoupled tip is important in this analysis because of its relationship to the power requirement of a helicopter rotor. In rotary wing vehicles, the power requirement is directly related to the torque created by the drag of the blades. The tip region of the blade is of primary interest because of its longer moment arm to the helicopter hub and associated high dynamic pressures which increase the drag considerably. In this section, the drag polars of two representative tip planforms will be presented and analyzed. The effect of tip drag on the complete semi-span configuration will also be investigated.

The configuration is modeled as a single component with a step change in incidence at the tip. The skin friction drag is estimated empirically and added to the induced drag predicted by VSAERO. The reader is once again reminded of the main assumption in this analysis, in that despite the constant spanwise dynamic pressure limitation of VSAERO, there exists a relationship between the data produced for a semi-span wing and the performance of a free-tip on a helicopter rotor blade in forward flight.

3.3.1 Tip Planform Drag Polars

The drag polars for TIP 2 and TIP 6 are shown in Figure 3.7. The tip planform areas were used to normalize the calculated lift and drag. Fewer data points were computed for $\Delta\theta = +5.0°$ to remain within the linear range of the lift curve.

The data are presented for three values of $\Delta\theta$ to illustrate the beneficial aspects of the free-tip concept in incompressible flow. Clearly, the drag produced in the tip region is substantially reduced for negative tip incidence angles. During the rotor tests of Reference 2, power reductions were recorded for tip Mach numbers up to $M_T \approx 0.85$ for $\Delta\theta < 0°$. Due to the limitations in compressible drag prediction, this cannot be verified for the semi-span wing and tip configuration with the VSAERO theoretical model.

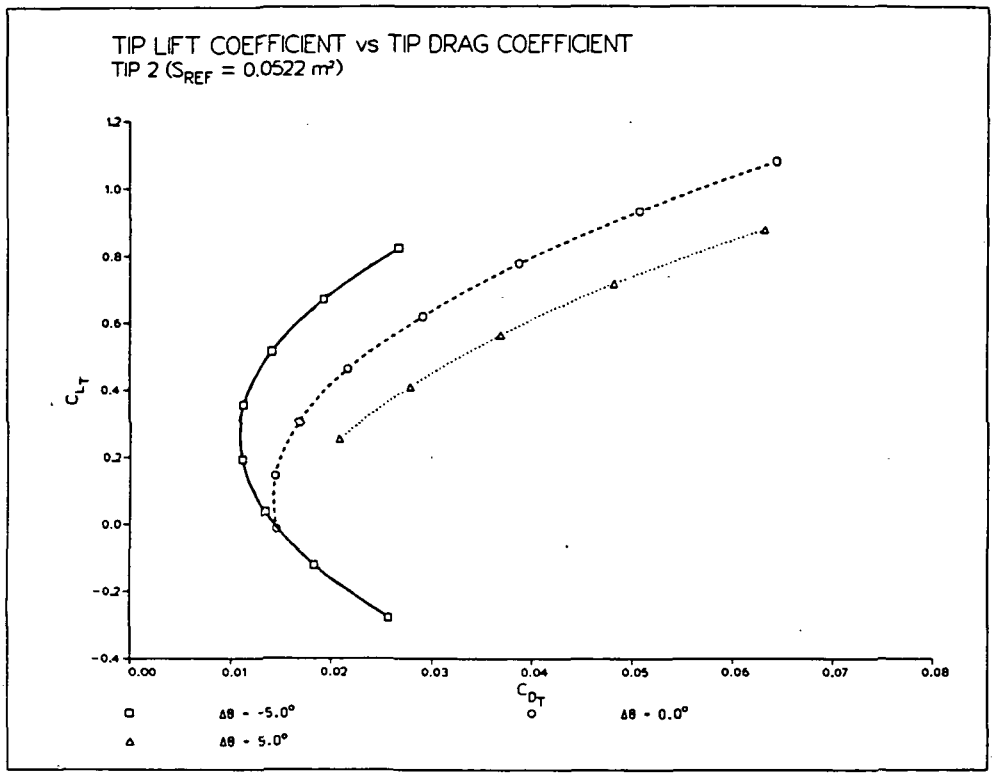

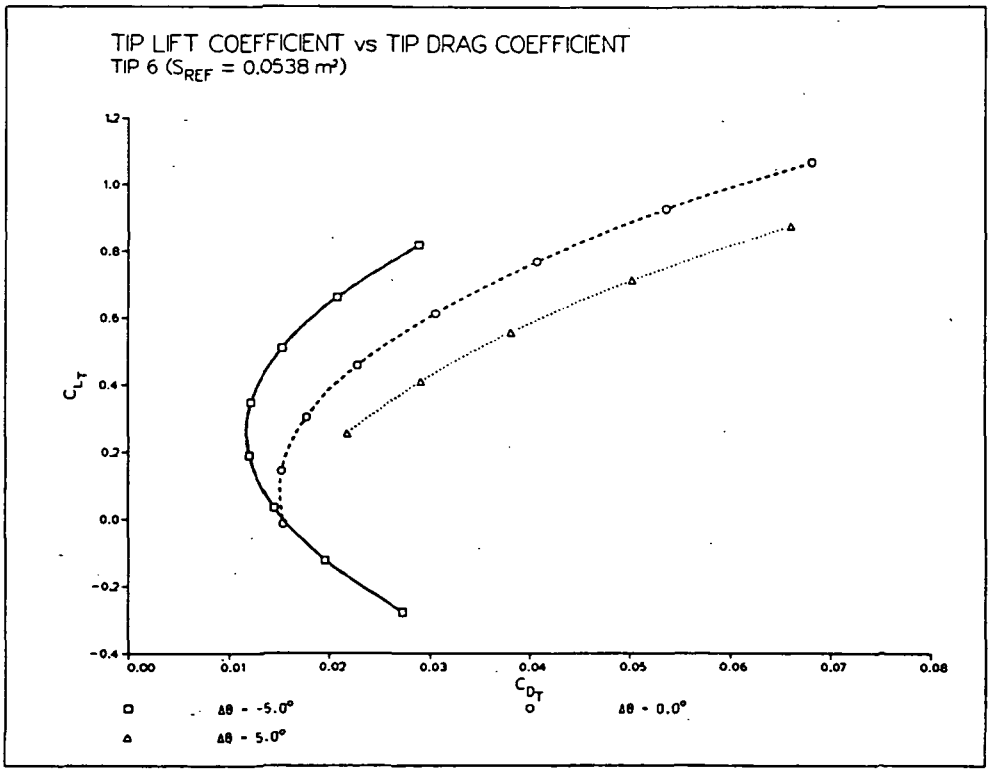

Re# = 0.867 million

Figure 3.7: TIP 2 and TIP 6 drag polars for $\Delta\theta$ = -5°, 0°, +5°

However, in incompressible flow, the drag reduction effect may be explained by considering a 2-D section cut of the tip surface. As shown in Figure 3.8, when the tip is undeflected, the downwash induced at the quarter chord by the semi-span wing tip vortex reduces the effective angle of attack of the section under consideration. The free-stream component of the resultant force (parallel to the onset velocity V_∞) is the induced drag contribution of the section. Now consider the case where the tip has an incidence of -5 degrees relative to the inboard section. A strong vortex is shed at the structural discontinuity due to the large spanwise lift gradient there. For a positive inboard loading which yields exactly the same sectional lift as for the $\Delta\theta = 0.0$ case, the velocities induced by the inboard vortex will reduce the magnitude of the downwash at the section. As illustrated in the bottom portion of Figure 3.8, this will result in a lower $\Delta\alpha$ and hence, less induced drag produced at the section under consideration. When the drag components of each section are integrated, the induced drag of the tip at $\Delta\theta = -5.0°$ is below the computed value for $\Delta\theta = 0.0°$.

The effects illustrated in Figure 3.8 thus verify the tip drag reductions measured during the first semi-span test (Reference 1) as reported in Reference 2. The semi-span wing and flow conditions modeled in the present study differ from those of the experimental rotor configuration used previously (Reference 2); also, as mentioned earlier, compressibility effects are not taken into account in the present drag prediction process. Despite this,

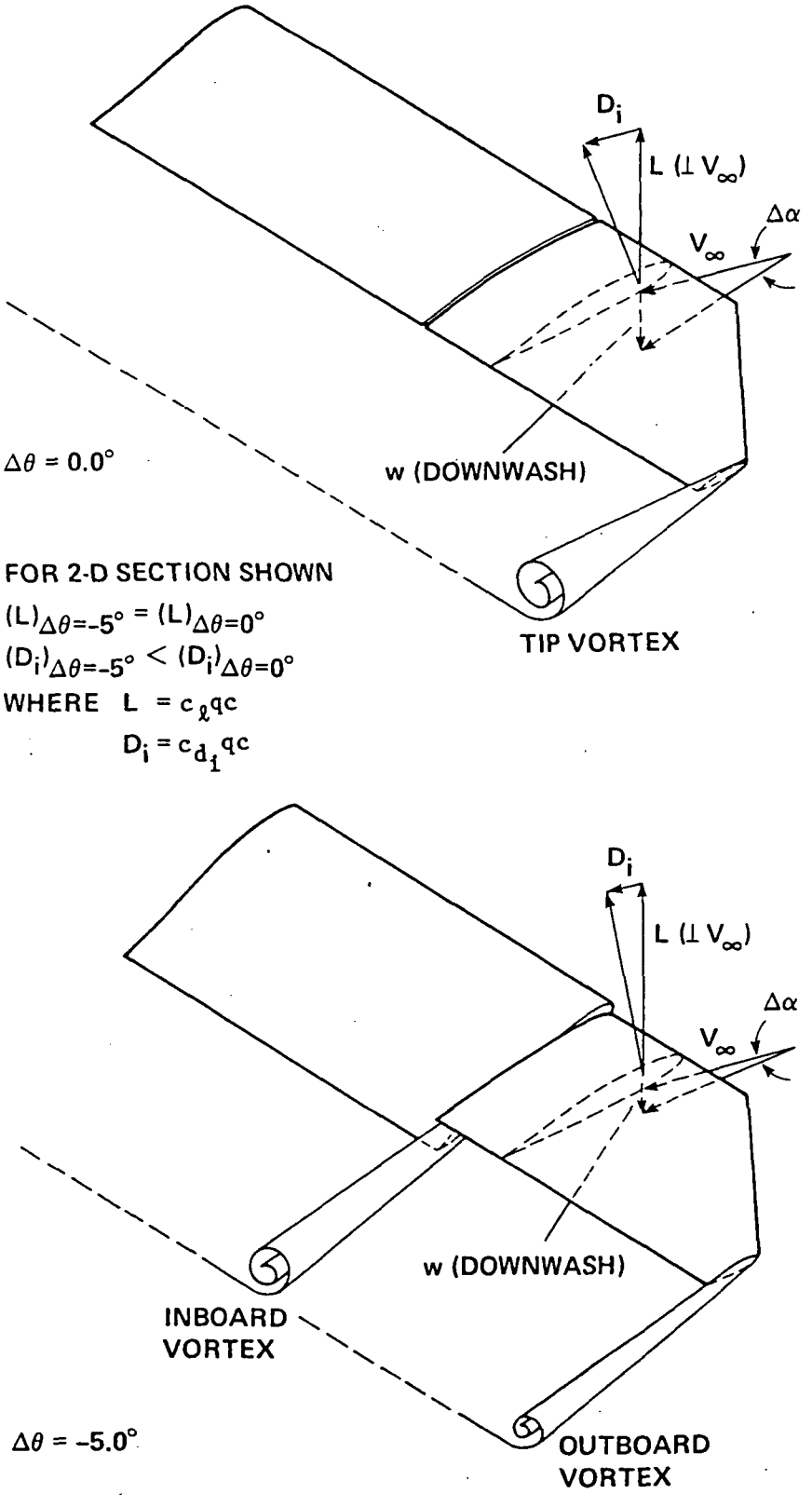

Figure 3.8: Sectional induced drag contributions at $\Delta\theta = 0°, -5°$

the induced drag reduction effect is believed to contribute significantly to the power reductions observed during the tests of Reference 2, even at high tip Mach numbers.

Since the analyses of TIP 2 and TIP 6 yielded equivalent drag polars (almost point for point), it was not judged necessary to produce similar data for TIP 3 and TIP 4 which are geometrically similar. This also shows that the tip geometry may be tailored to given performance requirements (i.e. a target value of C_{m_α}) without affecting the trends observed in the drag polar of the new baseline configuration (TIP 2).

3.3.2 Semi-Span Wing Drag Polars

Figure 3.9 shows the semi-span drag polars with different tip planforms as predicted by the method outlined previously (VSAERO and empirical data). The first effect which is readily apparent is that the drag polars are all identical; this follows from the results of Section 3.3.1, which showed little difference in drag behavior between the various tip planforms. Also, the tips contribute a fraction of the drag, due to the normalization of the integrated drag force by the total reference area of the semi-span wing. A slightly higher ratio of S_{WET}/S_{REF} (i.e. higher skin friction drag) accounts for the drag increase of TIP 6 (Figure 3.9).

The wing drag polars are plotted separately in Figure 3.10 for each tip planform with $\Delta\theta = -5°$, $0°$, $+5°$. These illustrate a point of major interest when one considers the differences in C_{D_W} with tip

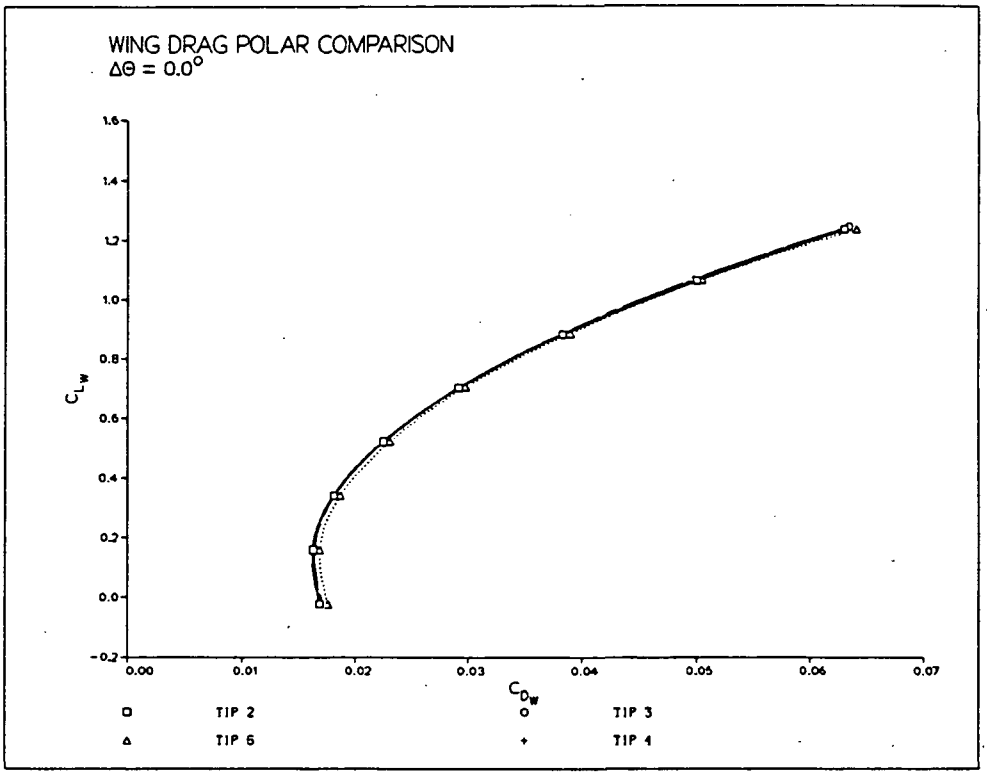

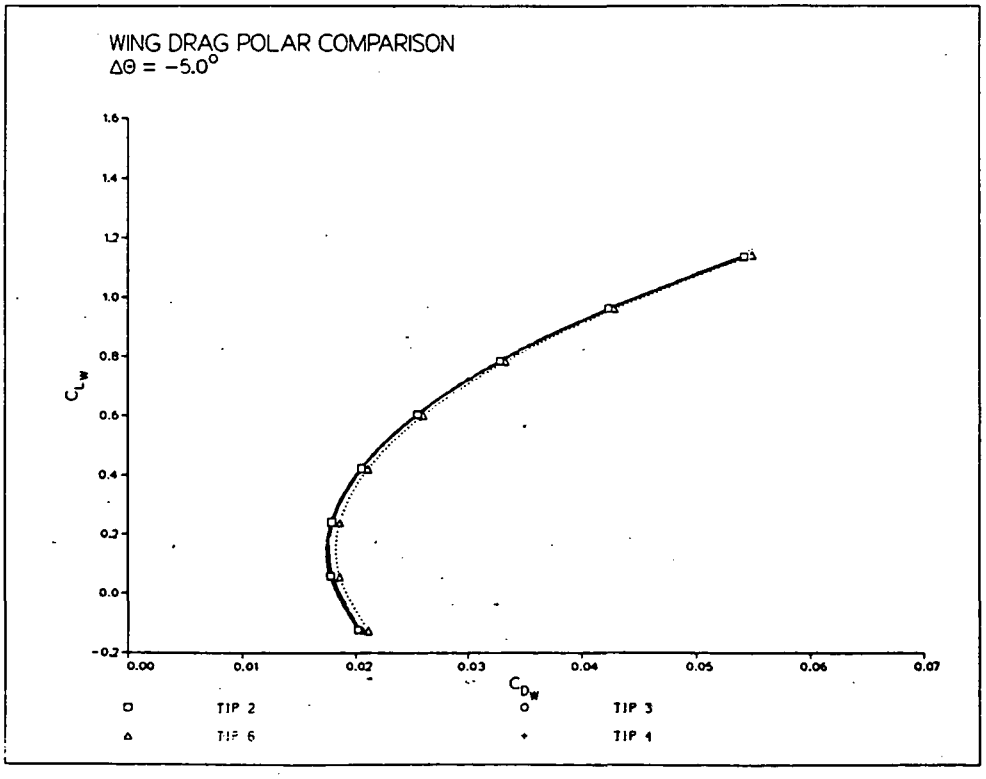

Re# = 0.867 million

Figure 3.9: Semi-span wing drag polars with new tips at $\Delta\theta = 0°, -5°$

C-2

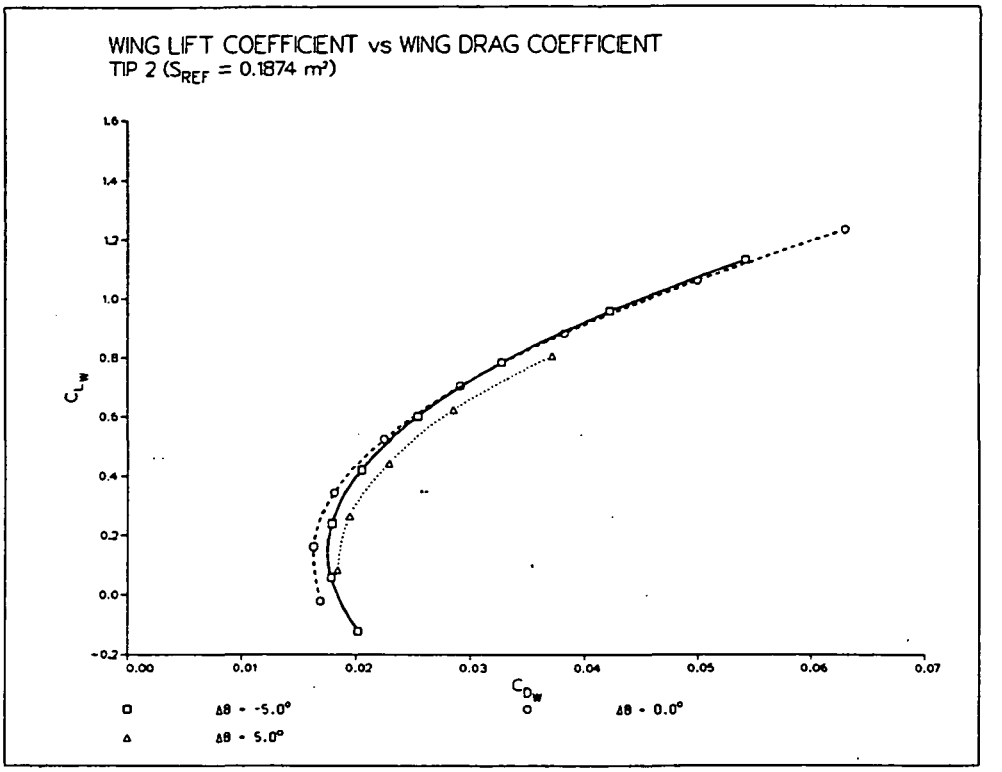

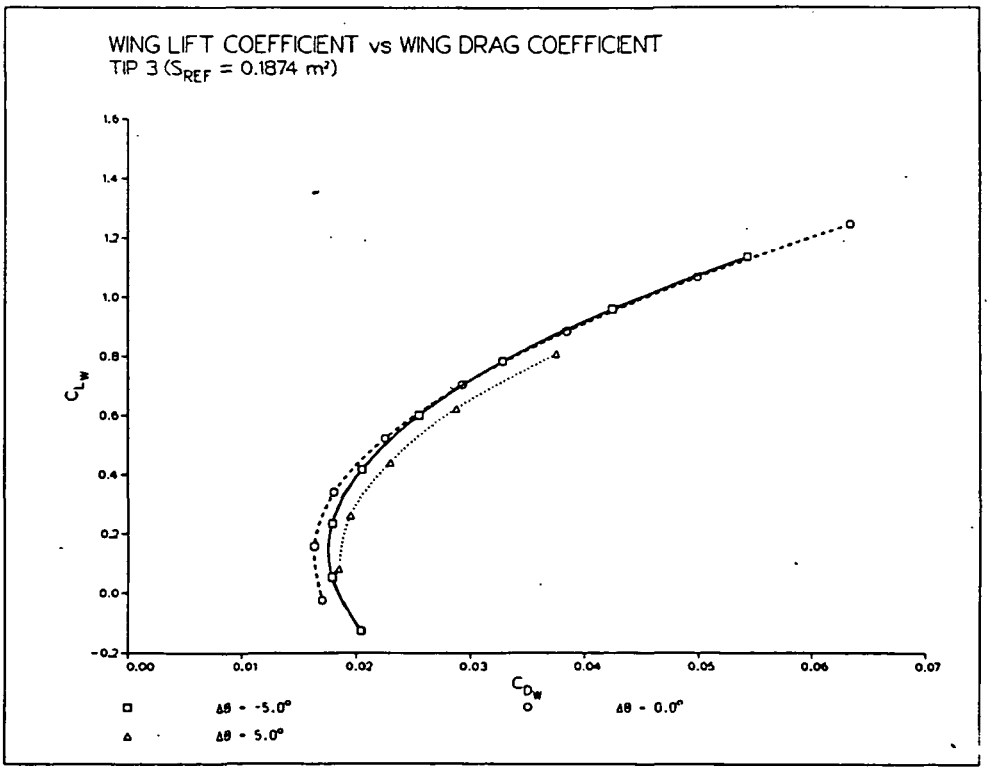

Re# = 0.867 million

Figure 3.10: Semi-span wing drag polars with new tips (continues)

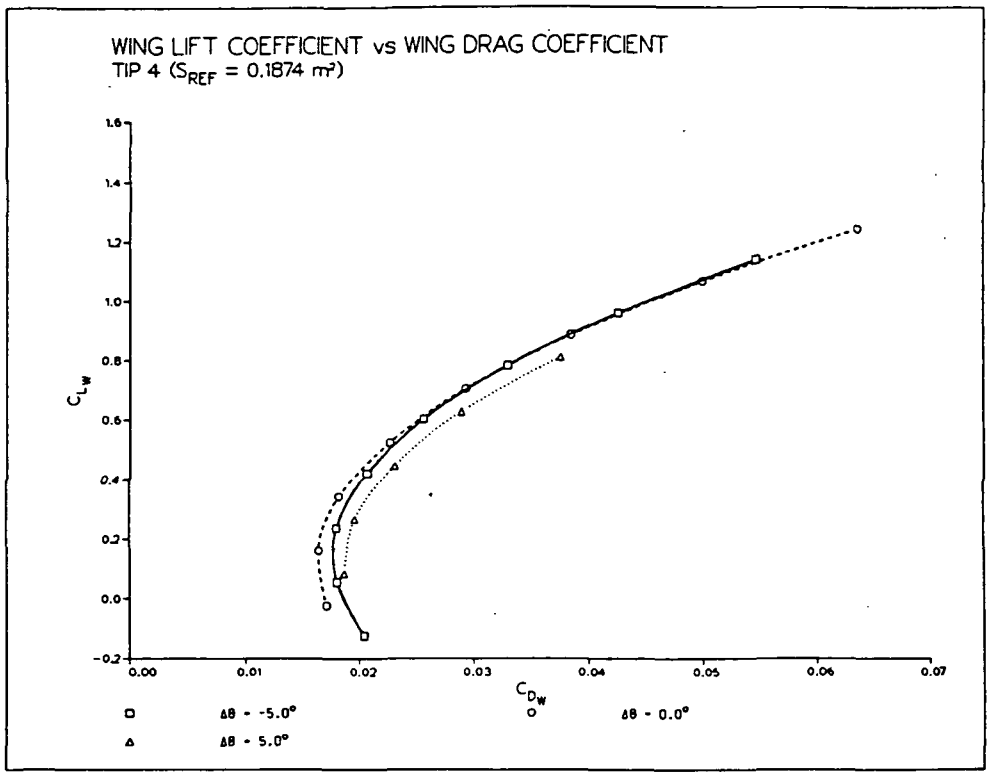

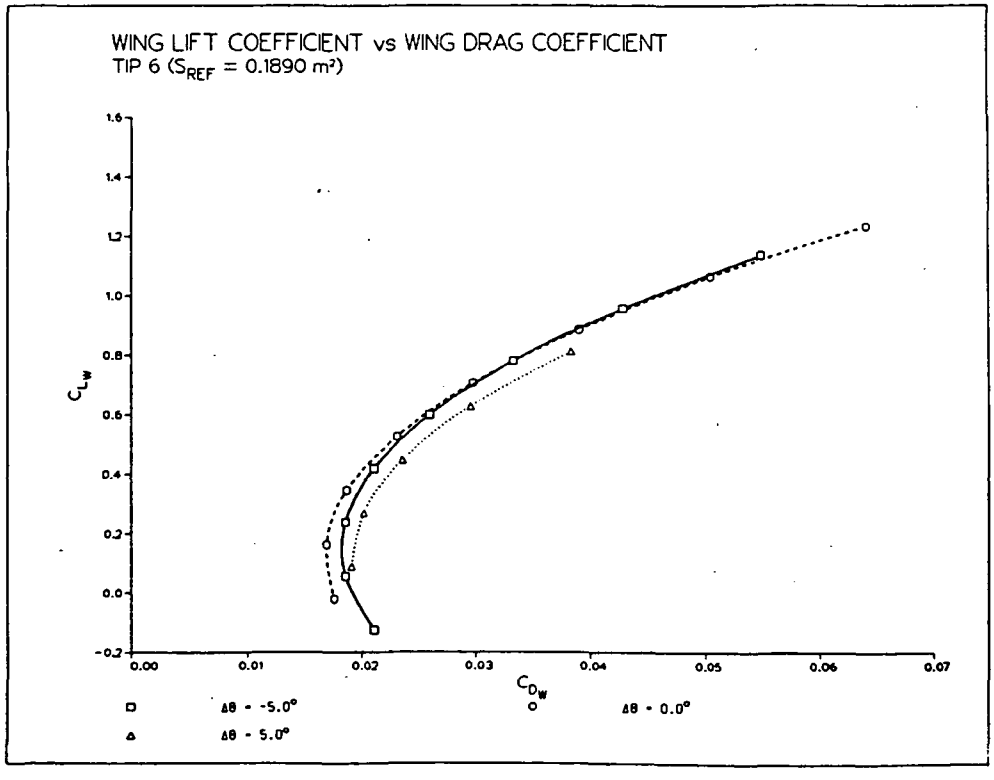

Re# = 0.867 million

Figure 3.10: Semi-span wing drag polars with new tips (concluded)

incidence angle. Observe that at low wing C_L's, the undeflected tip configuration produces less drag than with the tip at negative incidence angles. Since it was shown in Section 3.3.1 that negative tip deflections yield less tip drag than zero-incidence configurations, it is apparent that a sharp increase in the semi-span's drag occurs for negative values of $\Delta\theta$.

These observations, although difficult to quantify, may be described qualitatively. When the tip is undeflected, the effective aspect ratio of the wing is greater than at $\Delta\theta = -5.0$; therefore, the induced drag of the semi-span wing at $\Delta\theta = 0°$ will be at a minimum. When the tip has a finite deflection angle, the vortex is shed at the tip junction (increasing the induced drag of the wing) rather than at the outboard extremity. From Figure 3.10, for negative $\Delta\theta$'s at low values of C_{L_W} (and thus, low C_{L_T}) the reduction in tip drag is not sufficient to overcome the increase in C_D of the wing. However, note from Figure 3.7 that at higher C_{L_T}, the gap between tip C_D's increases (at constant C_{L_T}). Therefore, a point is reached where the drag reduction in the tip region balances the increase in wing drag; this is illustrated in Figure 3.10, where the curves for $\Delta\theta = -5.0°$ and $0.0°$ merge.

Since this approach does not account for the radial variation of dynamic pressure, one can only speculate about the resulting drag of a free-tip equipped helicopter rotor. In numerical analyses which use blade element theory, the sectional drag coefficients vary radially, as they are a function of local angle of attack, Reynolds

number, and Mach number. Whatever the local value of C_d, the drag force computed for each blade element will increase in the outboard direction because of increasing dynamic pressure. Since the free-tip is located in the region of highest dynamic pressure, the drag reduction which takes place there for negative incidence angles is probably significant. This effect is the most probable cause for the drop in required power which was observed during the small-scale rotor test discussed in Reference 2.

4. CONCLUSIONS

The following conclusions can be made regarding the analysis of the semi-span wing with VSAERO:

- The VSAERO computer program has been used to model the characteristics of a semi-span wing with a deflected tip. The knowledge gained in using the code indicates that the best modeling techniques are as follows:
  - The open-tips at the gap method gives best C_{L_T} vs α_T correlation.
  - The continuous component with step change in incidence yields best C_{m_T} vs α_T and C_{m_T} vs C_{L_T} correlation.
  - The correlation of spanwise loading with experimental data is very satisfactory.
- Drag prediction is unacceptable, primarily due to poor skin friction drag estimation.
- The variation of C_{m_T} with α_T may be increased considerably with modifications to the tip planform geometry, as shown by the design of new tips.
- In shock-free compressible flow at $M_\infty = 0.70$, the VSAERO model predicts an average of 47% increase in $(C_{m_\alpha})_T$ from its incompressible value. None of the new tips stand out with larger increases in $(C_{m_\alpha})_T$ at a given Mach number. The predicted aerodynamic center travel is consistent with sectional and 3-D compressible flow theory.

- VSAERO analyses of a semi-span wing predict an increase in $(C_{m_\alpha})_T$ of 26% when M_∞ is increased from 0.49 to 0.70. These Mach numbers are representative of retreating and advancing side tip Mach numbers for the small-scale rotor of Reference 2.
- For negative tip incidence angles, it has been shown analytically that the tip drag is reduced. This confirms the experimental results of Reference 1.
- At higher wing C_L's, the tip drag reduction balances the increase in induced drag of the inboard blade.
- The drag polars of the semi-span configuration are not sensitive to planform geometry.

Recommendation:

For the next phase in the numerical analysis of the free-tip concept, consideration should be given to reproducing the exact conditions under which the free-tip should operate. This could be done by incorporating the equations of motion of the tip (including inertia effects, controller moment, and aerodynamic moment) to an existing rotor code which would account for the following effects:

- Transonic Mach numbers (up to $M_\infty = 0.9$)
- Unsteady aerodynamics and correction for viscous effects
- Free wake capability with blade vortex interaction modeling.

If a rotary wing code were used, a more accurate prediction of inboard blade effects induced on the tip would be possible.

REFERENCES

1. Van Aken, J. M. An Investigation of Tip Planform Influence on the Aerodynamic Load Characteristics of a Semi-span Wing and Wing-Tip. The University of Kansas Center for Research, Inc., Lawrence, Kansas, Report #5171-1, December 1985.

2. Stroub, R. H. Analysis of the Free-Tip Rotor Wind Tunnel Test Results. NASA TM 86751, May 1985.

3. Kumagai, H. A Feasibility Study of Free-Tip Rotor Application as a Passive Cyclic Control Device. D.E. Thesis, The University of Kansas Dept. of Aerospace Engineering, Lawrence, Kansas, February 1984.

4. Maskew, B. Program VSAERO--A Computer Program for Calculating the Non-Linear Aerodynamic Characteristics of Arbitrary Configurations (Theory Document). Analytical Methods, Inc., Redmond, Washington, December 1984.

5. Maskew, B. Program VSAERO--User's Manual. Analytical Methods, Inc., Redmond, Washington, April 1982.

6. Kumagai, H. Spanwise Lift Distribution and Wake Velocity Surveys of a Semi-Span Wing with a Discontinuous Twist. NASA report (to be published).

7. Roskam, J. Methods for Estimating Drag Polars of Subsonic Airplanes. Roskam Aviation and Engineering Corporation, Ottawa, Kansas.

8. Johnson, W. Helicopter Theory. Princeton University Press, Princeton, New Jersey, 1980.

9. U.S. Army. U.S. Army Helicopter Design DATCOM. USAAMRDL CR 76-2, 1976.

10. Roskam, J. Airplane Flight Dynamics and Automatic Flight Controls, Part I. Roskam Aviation and Engineering Corporation, Ottawa, Kansas, 1979.

11. Kuchemann, D. The Aerodynamic Design of Aircraft. Pergamon Press, Oxford, England, 1978.

12. Abbot, I. H., and Von Doenhoff, A. E. Theory of Wing Sections. Dover Publications, New York, 1959.

APPENDIX A:

VSAERO THEORETICAL FORMULATION

The theoretical formulation of the code is based on the computation of the velocity potential at a point P in the flow field under consideration. The governing equations are (Reference 4)

$$\nabla^2 \phi = 0$$

$$\nabla^2 \Phi_i = 0$$

$$\Phi_P = \frac{1}{4\pi} \iint_{S+W+S_\infty} (\Phi - \Phi_i)\mathbf{n} \cdot \nabla \left(\frac{1}{r}\right) dS$$

$$- \frac{1}{4\pi} \iint_{S+W+S_\infty} \frac{1}{r} \mathbf{n} \cdot (\nabla\Phi - \nabla\Phi_i) dS \qquad (A.1)$$

Where Φ and Φ_i are velocity potentials which exist outside and inside the region of interest, respectively, and "r" is the distance from the point P to the element dS on the surface; "n" is the unit normal vector to the surface pointing into the fluid (Figure A.1). The first integral represents the disturbance potential from a surface distribution of doublets with density $(\Phi - \Phi_i)$ per unit area while the second integral represents the contribution from a surface distribution of sources with density $-\mathbf{n} \cdot (\nabla\Phi - \nabla\Phi_i)$ per unit area. The doublet density accounts for the local jump in potential, and the source density is associated with the local jump in normal components of velocity.

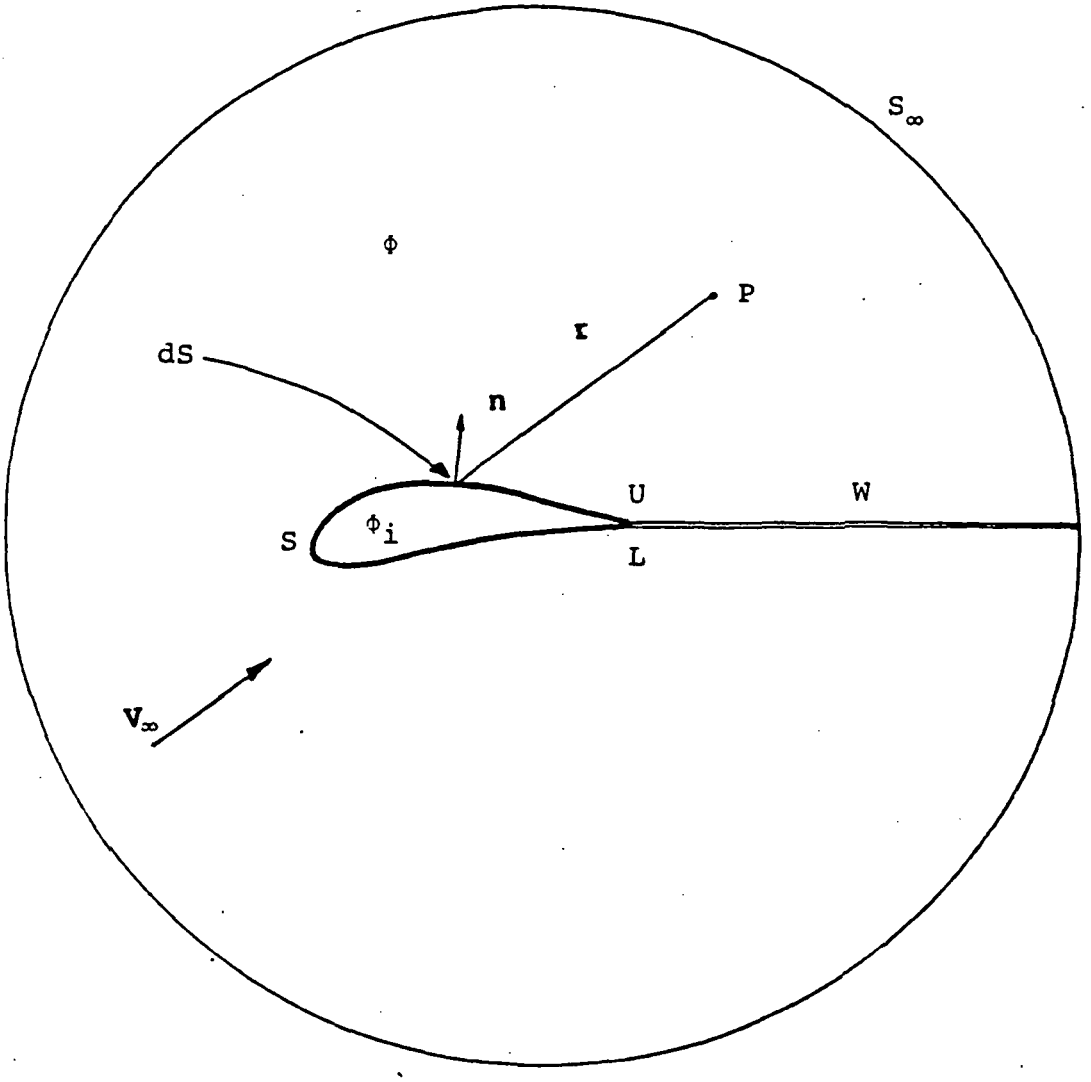

Figure A.1: VSAERO idealized flow model--plane cut through 3-D body

Since onset flow conditions are assumed to exist at S_∞, the integrals taken over this surface will reduce to ϕ_{∞_P}, the velocity potential at point P due to the onset flow. Also, the upper and lower wake surfaces are assumed to coincide into a thin wake, so the Φ_i term for that integral disappears. If entrainement into the wake surface is neglected, the jump in normal component $\mathbf{n} \cdot (\nabla\Phi_U - \nabla\Phi_L)$ vanishes so the source terms associated with the wake also disappear. Equation (A.1) above then becomes

$$\Phi_P = \frac{1}{4\pi} \int_S \int (\Phi - \Phi_i)\mathbf{n} \cdot \nabla(\frac{1}{r})dS$$

$$- \frac{1}{4\pi} \int_S \int \frac{1}{r} \mathbf{n} \cdot (\nabla\Phi - \nabla\Phi_i)dS$$

$$+ \frac{1}{4\pi} \int_W \int (\Phi_U - \Phi_L)\mathbf{n} \cdot \nabla(\frac{1}{r})dW + \phi_{\infty_P} \qquad (A.2)$$

If point P lies on the surface, the integral becomes singular there and the point must be avoided. This is easily achieved by locally modifying the path of integration around point P in the form of a hemisphere. In the limit as the sphere radius goes to zero, the local contribution to velocity potential is $1/2(\Phi - \Phi_i)_P$, which is half the local jump in potential across the surface at P. The first potential in the expression being on the side of the surface on which P is located, if P is on the inside surface then Equation (A.2) becomes

$$\Phi_P = \frac{1}{4\pi} \iint_{S-P} (\Phi - \Phi_i)\mathbf{n} \cdot \nabla(\frac{1}{r})dS - \frac{1}{2}(\Phi - \Phi_i)_P$$

$$- \frac{1}{4\pi} \iint_S \frac{1}{r} \mathbf{n} \cdot (\nabla\Phi - \nabla\Phi_i)dS$$

$$+ \frac{1}{4\pi} \iint_W (\Phi_U - \Phi_L)\mathbf{n} \cdot \nabla(\frac{1}{r})dW + \phi_{\infty_P} \qquad (A.3)$$

The external Neumann boundary condition is applied through the following relation:

$$\mathbf{n} \cdot \nabla\Phi = -\mathbf{V}_N \text{ on } S \qquad (A.4)$$

where V_N is the resultant normal component of velocity relative to the surface. Nonzero values of V_N are used to model boundary layer displacement effects.

The wake surface W does not support a load; the local vorticity vector (for an element dW) associated with the doublet distribution $(\Phi_U - \Phi_L)$ is given by

$$\gamma = -\mathbf{n} \times \nabla(\Phi_U - \Phi_L) \qquad (A.5)$$

From the Kutta-Joukowski law, the elementary force on dW, in the presence of the mean velocity V, is

$$\delta\mathbf{F} = \rho\mathbf{V} \times \gamma dW \qquad (A.6)$$

Since $\vec{V} \times \vec{\gamma} = 0$ must hold for the force to be zero, then from Equation (A.5)

$$\mathbf{V} \times \{\mathbf{n} \times \nabla(\Phi_U - \Phi_L)\} = 0 \qquad (A.7)$$

after expansion,

$$\mathbf{n}\mathbf{V} \cdot \nabla(\Phi_U - \Phi_L) - \mathbf{V} \cdot \mathbf{n}\nabla(\Phi_U - \Phi_L) = 0 \qquad (A.8)$$

This equation is satisfied when $\mathbf{V} \cdot \mathbf{n} = 0$, i.e. if the surface W is aligned with the local flow direction. Also, $\mathbf{V} \cdot \nabla(\Phi_U - \Phi_L) = 0$ must be satisfied, so that the gradient of the doublet distribution is zero along mean streamlines in the wake surface; therefore, the wake doublet distribution is constant along mean streamlines in the wake and is determined by the condition at the point where the streamline leaves the surface S. Throughout the iterative process, the Kutta condition is implied by shedding the trailing edge potential jump $(\Phi_U - \Phi_L)$ as a constant down each streamwise line on an initially prescribed wake surface. Once the solution has converged, the upstream edge of the wake (hence the trailing edge) will carry no load, satisfying the Kutta condition.

The application of an internal boundary condition is what makes the VSAERO approach accurate, convenient to use, and robust (relatively insensitive to bad paneling schemes). The essence of the procedure is to ensure that when passing through the boundary S, the jump in potential from the internal flow to the external flow should be small. This requires a minimum of perturbation from the singularities and is achieved by specifying that the internal flow potential be equal to the onset flow potential. Writing the total potential as the sum of the onset and perturbation potentials $\Phi = \phi_\infty + \phi$, and applying the internal Dirichlet boundary condition $\Phi_i = \phi_\infty$, Equation (A.3) becomes (with $\Phi_P = \phi_\infty$)

$$\iint_{S-P} \phi \mathbf{n} \cdot \nabla\left(\frac{1}{r}\right) dS - \frac{1}{2}\phi_P + \int_W \int (\Phi_U - \Phi_L)\mathbf{n} \cdot \nabla\left(\frac{1}{r}\right) dW$$

$$- \int_S \int \frac{1}{r} \mathbf{n} \cdot (\nabla\Phi - \nabla\phi_\infty) dS = 0 \qquad \text{(A.9)}$$

Comparing the above expression with Equation (A.3), it is observed that now the doublet density may be expressed as

$$4\pi\mu = \phi = \Phi - \phi_\infty \qquad \text{(A.10)}$$

while the source distribution is

$$4\pi\sigma = - \mathbf{n} \cdot (\nabla\Phi - \nabla\phi_\infty) \qquad \text{(A.11)}$$

The first term in Equation (A.11) may be replaced by the Neumann boundary condition (Equation 2.4) to obtain

$$4\pi\sigma = V_N - \mathbf{n} \cdot \mathbf{V}_\infty \qquad \text{(A.12)}$$

For the first potential flow solution, no boundary layer parameters are available; and since the boundary is solid, $V_N = 0$. With the panel geometry already established, the terms $\mathbf{n} \cdot \mathbf{V}_\infty$ may be computed easily so the source distribution is known at the outset. Once the first potential solution is determined, the pressure distributions are transferred to the boundary layer routine. In subsequent potential flow calculations, the source distribution is given by

$$4\pi\sigma = \frac{\partial}{\partial s}(V_e \delta^*) + V_{NORM} - \mathbf{n} \cdot \mathbf{V}_\infty \qquad \text{(A.13)}$$

where the first term on the RHS is obtained from boundary layer calculations.

The integral relation (Equation A.9) may be solved for the unknown velocity potential distribution over the body surface. In the numerical procedure, the equation is satisfied at a finite number of points on the surface (one control point on each body panel with the doublet and source distributions assumed constant on each panel). The surface integrals therefore become summations over all panels, and the integral relation (Equation A.9) is transformed into a set of simultaneous linear algebraic equations where the unknowns are the doublet strength on each body panel μ_K (recall that the source strengths σ_K are known--Equations 2.12 and 2.13):

$$\sum_{K=1}^{N_S} (\mu_K C_{JK}) + \sum_{L=1}^{N_W} (\mu_{W_L} C_{JL}) + \sum_{K=1}^{N_S} \sigma_K B_{JK} = 0; \; J = 1, \; NS \tag{A.14}$$

At the outset, the wake panel doublet strengths μ_{W_L} are not known and the second summation is not required. For subsequent iterations, the computed trailing edge potential jump $\mu_W = \Phi_U - \Phi_L$ is shed as a constant down each wake column, as discussed before. In the code, the system of equations above is solved by a direct method for a moderate number of unknowns and by a blocked Gauss-Seidel iterative procedure for larger numbers of panels. Note that since $\phi_P = 4\pi\mu_P$, $C_{JJ} = -2\pi$ accounts for the $-1/2\phi_P$ term when the point P is on the surface. N_S and N_W are the number of surface and wake panels, respectively. B_{JK} and C_{JK} are the perturbation velocity potential influence coefficients for the constant source

and doublet distribution of panel K acting on the control point of panel J. From Equations (A.9) and (A.14) it is seen that

$$B_{JK} = \int\int_{\text{Panel K}} \frac{1}{r}\, dS \tag{A.15}$$

and

$$C_{JK} = \int\int_{\text{Panel K}} \mathbf{n} \cdot \nabla\left(\frac{1}{r}\right) dS \tag{A.16}$$

The vectors $\mathbf{n} = \mathbf{n}_K$ are established by the local geometry and are constant for each panel; r is the length of the vector from the surface elements of dS of panel K to the control point of panel J. When the doublet solution is known, Equation (A.3) can be rewritten as

$$\Phi_P = \int_S\int \mu\, \mathbf{n} \cdot \nabla\left(\frac{1}{r}\right) dS + K\mu_P + \int_S\int \frac{\sigma}{r}\, dS$$

$$+ \int_W\int \mu_W\, \mathbf{n} \cdot \nabla\left(\frac{1}{r}\right) dW + \phi_{\infty_P} \tag{A.17}$$

where μ and σ are defined by Equations (A.10) and (A.12) and $\mu_W = \Phi_U - \Phi_L$ are the wake doublet values (constant for each wake column). If point P is off the surface, K = 0; if P lies on the inside of the surface, $K = -2\pi$; and $K = 2\pi$ if P is on the outside of the surface. The velocity field may be computed at specified mesh points by taking the gradient $V_P = -\nabla\Phi_P$

$$\mathbf{V}_P = -\int_S\int \mu\nabla[\mathbf{n} \cdot \nabla\left(\frac{1}{r}\right)]dS - \int_S\int \sigma\, \nabla\left(\frac{1}{r}\right) dS$$

$$- \int_W\int \mu_W \nabla[\mathbf{n} \cdot \nabla\left(\frac{1}{r}\right)]dW + \mathbf{V}_\infty \tag{A.18}$$

To compute the forces and moments due to the body pressure distribution, the local velocity at each panel must be determined. The following relationships are used:

$$\mathbf{V} = \mathbf{V}_\infty + \mathbf{v} \tag{A.19}$$

$$\mathbf{v} = VL\boldsymbol{\ell} + VM\mathbf{m} + VN\mathbf{n} \tag{A.20}$$

where "v" is the perturbation velocity and $[\boldsymbol{\ell},\mathbf{m},\mathbf{n}]$ are unit vectors in the local panel coordinate system. The normal velocity component is obtained directly from the source strength $VN = 4\pi\sigma$, while the tangential components VL and VM are evaluated from the gradient of μ. The gradient is based on an assumed quadratic doublet distribution between three adjacent panels in a given direction centered on the panel under consideration. Once the total velocity at the center of the panel is known, the force coefficient contribution from panel K is

$$\frac{\Delta F_K}{q_\infty} = -C_{p_K} * AREA_K * \mathbf{n}_K + C_{f_K} * AREA_k * (\mathbf{t}_k) \tag{A.21}$$

where

$$C_{p_K} = 1 - V_K^2 / V_\infty^2 \tag{A.22}$$

and the pressure coefficient is evaluated at the panel center. C_{f_K} is the local skin friction coefficient and is zero during the first potential solution; $\mathbf{n}_k$ and $\mathbf{t}_k$ are unit vectors normal to the panel's mean plane and in the direction of the local velocity ($\mathbf{t}_k = \mathbf{V}_k / |\mathbf{V}_k|$). Now if K_1 and K_2 are the first and last panels on a component (for example, the free-tip), then the component force vector is

$$\frac{\mathbf{F}_p}{q_\infty} = \sum_{K=K_1}^{K_2} \frac{\Delta \mathbf{F}_K}{q_\infty} \tag{A.23}$$

and the force coefficient vector is computed as

$$\mathbf{C}_{F_p} = \mathbf{F}_p / q_\infty S_{REF} = \sum_{K=K_1}^{K_2} \frac{\Delta \mathbf{F}_K}{q_\infty} / S_{REF} \tag{A.24}$$

where S_{REF} is a user-specified reference area. The contribution of panel K to the moment coefficient vector is

$$\Delta \mathbf{C}_{M_K} = \frac{\mathbf{R}_K \times \Delta \mathbf{F}_K}{q_\infty \cdot S_{REF} \cdot L} \tag{A.25}$$

where $\mathbf{R}_K$ is the position vector of the control point on the panel K, relative to the moment reference point; for calculation of pitching moment coefficient L = CBAR, the reference chord specified by the user. Coordinate transformations are then applied to the force and moment coefficient vectors to obtain C_L, C_D, and C_m in wind axes.

PAGE B-1 INTENTIONALLY BLANK

(4) If $M_{LOCAL} < 1.20$ everywhere, a check was done to verify whether the highest predicted sectional C_ℓ value of the tip or inboard section was in the linear range of the 2-D experimental lift curve (Figure B.1). Both cases, M_∞ = 0.70 and M_∞ = 0.49, were verified in this manner.

(5) If nonlinear characteristics were encountered, α_T was reduced gradually until maximum C_ℓ values were within the linear range for the specified Mach numbers.

The procedure outlined above is based on the assumption that VSAERO predicts the spanwise loading distribution with good accuracy, since it is the maximum predicted sectional C_ℓ which is checked against the data of Figure B.1. Also, even if some local Mach numbers are greater than one, then the calculated sectional lift may still lie in the linear range (as long as the supersonic flow region is not too large). This is based on the fact that even after sonic flow is encountered over an airfoil, M_∞ may be increased appreciably before the onset of nonlinear effects due to compressibility (Reference 12).

Because of the comparisons with 2-D experimental data, three-dimensional viscous effects which may cause separation cannot be taken into account using this approach. However, the final selection of α_w and α_T are believed to be sufficiently conservative to justify its use.

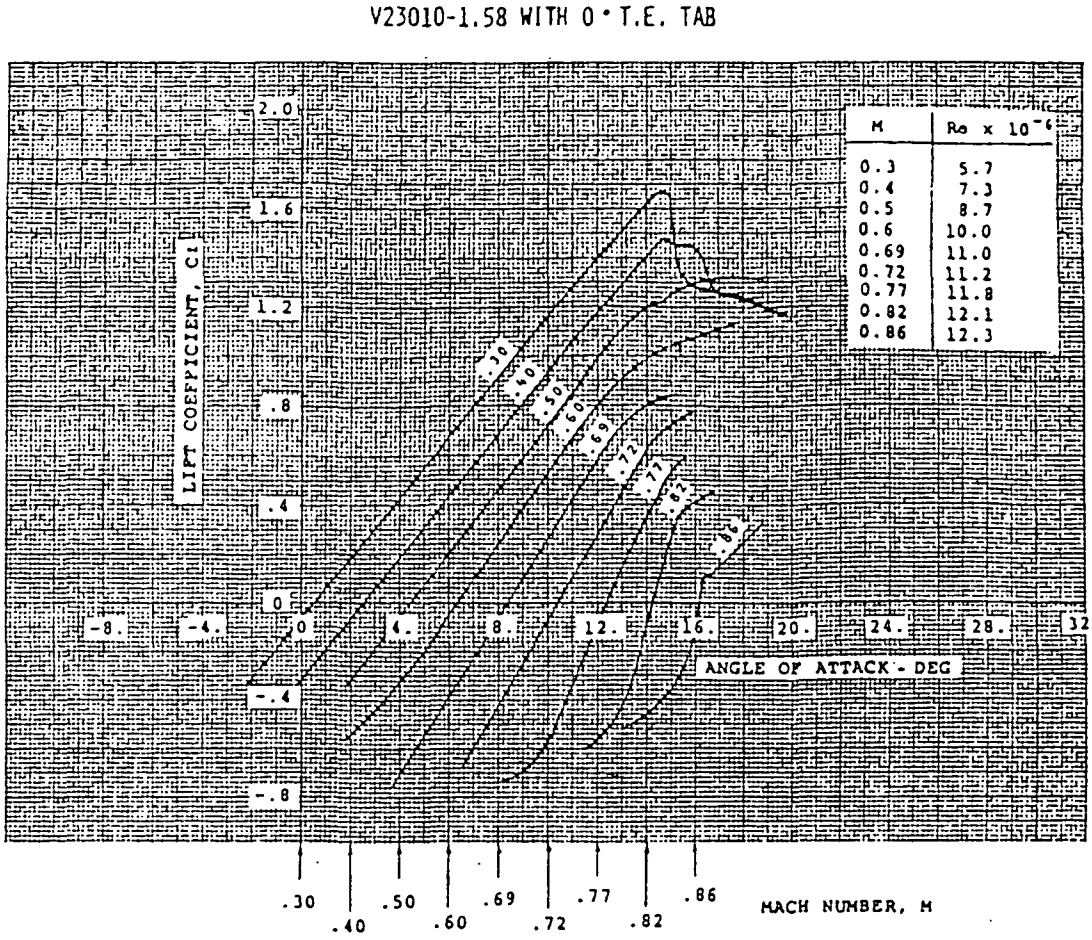

Figure B.1: 2-D lift characteristics of the V23010-1.58 airfoil in compressible flow (taken from Reference 9)

APPENDIX C:

COMPUTED LIFT AND PITCHING MOMENT COEFFICIENTS AT $M_\infty = 0.70$ and $M_\infty = 0.49$ for TIP 2, TIP 3, TIP 4 AND TIP 6

The data in the following tables follow from the incidence angle limits specified in Table 3.3. Observe that generally, the predicted growth of the separated flow region agrees with corresponding increases in the tip angle of attack. In some cases, however, there may be sudden increases in the size of the separated flow region, or there may be irregularities in the trends. For example, in Table C.1 at $\Delta\theta = -5°$ ($M_\infty = 0.70$), as α_T varies from -1° to -5°, the separated flow region on the lower surface increases to 14.9% and then decreases to 9.0%. These discrepancies are associated with the fact that these data are initial estimates only and do not represent converged solutions (see Section 3.2.1).

The asterisks indicate the points which were not used to calculate local lift and pitching moment slopes. These did not fall within the linear range established by the two lowest values of C_{L_T} or C_{m_T}. Lift and pitching moment data were also produced for $\alpha_W = 6°$ to verify the trends in C_{L_T} and C_{m_T} established by the data points falling within the limits of Table 3.3; if within the linear range, this fourth point was then used to calculate the slope. At $M_\infty = 0.7$, VSAERO output showed some local Mach numbers (on the tip surface) exceeding 1.2 for $\alpha_W = 6°/\alpha_T = 4°$, at $M_\infty = 0.70$. Also, for tip angles of -5° and -8°, the lift deviates from the linear range

due to separation, so those points were also not used in the slope computations. The final value of the C_{L_T} and C_{m_T} slopes were obtained by taking the average of the slopes for each $\Delta\theta$ at the given Mach number. When data points in the nonlinear range were eliminated, the slopes were always in good agreement with each other.

Note that at $M_\infty = 0.70$, the combination of high Reynolds number and large compressibility effects (although subcritical) results in chordwise pressure gradients that cause larger regions of separated flow than at $M_\infty = 0.49$. This normal trend further indicates that converged solutions in the nonlinear range could probably be obtained with further use of the wake stitching procedure. Observe from Table 3.1 and the separation patterns of Tables C.1-C.4 that as $\Lambda_{c/4}$ of the outboard half of the tip decreases (consider tips 2, 3, and 6), the size of the separated flow regions also decrease as expected. This is a critical observation, since $(C_{m_\alpha})_T$ would decrease at the onset of stall, thereby illustrating the need for compromise between high sweep angles [high negative $(C_{m_\alpha})_T$ at low Mach numbers] and a decrease in response [loss of $(C_{m_\alpha})_T$ at high M_∞ and Reynolds numbers] associated with these higher sweep angles.

Table C.1: Predicted Compressible Lift and Pitching Moment for TIP 2

(1) $M_\infty = 0.70$, Re# = 3.390×10^6

α_W	α_T	$\Delta\theta$	$(C_L)_T$	$(C_{m_{0.25}})_T$	% Separated Flow Upper	Lower
0	-8	-8	-0.5169	0.1129*	0.0%	10.5%
2	-6	-8	-0.3549	0.0704*	0.0%	9.24%
4	-4	-8	-0.1616	0.0271	1.2%	9.0%
6	-2	-8	0.0486	-0.0194	--	--
0	-5	-5	-0.3589	0.0691*	0.0%	9.0%
2	-3	-5	-0.1595	0.0237	1.4%	14.9%
4	-1	-5	0.0558	-0.0248	2.2%	2.4%
6	+1	-5	0.3030	-0.0746*	--	2.4%
0	-2	-2	-0.1602	0.0213	1.6%	16.7%
2	0	-2	0.0576	-0.0285	2.4%	2.2%
4	+2	-2	0.3063	-0.0786*	6.6%	1.5%
6	+4	-2	0.5532	-0.1295*	--	--

(2) $M_\infty = 0.491$, Re# = 2.378×10^6

α_W	α_T	$\Delta\theta$	$(C_L)_T$	$(C_m)_T$	% Separated Flow Upper	Lower
6	-8	-14	-0.3556	0.0662*	--	--
8	-6	-14	-0.1784	0.0345*	0.0%	13.8%
10	-4	-14	0.0031	-0.00048	0.0%	11.2%
12	-2	-14	0.1878	-0.0370	1.4%	0.75%
6	-5	-11	-0.1604	0.0267	--	--
8	-3	-11	0.0238	-0.0098	0.96%	13.5%
10	-1	-11	0.2095	-0.0471	1.73%	0.87%
12	+1	-11	0.3991	-0.0856	2.33%	0.0%
6	-2	-11	0.0357	-0.0158	--	--
8	0	-8	0.2201	-0.0530	1.8%	0.27%
10	+2	-8	0.4139	-0.0933	2.7%	0.0%
12	+4	-8	0.6150	-0.1357	7.5%	0.0%

Table C.2: Predicted Compressible Lift and Pitching Moment for TIP 3

(1) $M_\infty = 0.70$, Re# = 3.390×10^6

α_W	α_T	$\Delta\theta$	$(C_L)_T$	$(C_{m_{0.25}})_T$	% Separated Flow Upper	Lower
0	-8	-8	-0.5175	0.0974*	0.0%	8.5%
2	-6	-8	-0.3583	0.0603*	0.0%	6.8%
4	-4	-8	-0.1639	0.0210	0.0%	12.4%
6	-2	-8	0.0474	-0.0207	--	--
0	-5	-5	-0.3610	0.0588*	0.0%	6.6%
2	-3	-5	-0.1611	0.0183	0.0%	13.4%
4	-1	-5	0.0544	-0.0248	1.3%	1.6%
6	+1	-5	0.3034	-0.0686*	--	--
0	-2	-2	-0.1611	0.0166	0.0%	2.6%
2	0	-2	0.0571	-0.0277	1.6%	1.1%
4	+2	-2	0.2074	-0.0716*	2.5%	0.0%
6	+4	-2	0.5576	-0.1174*	--	--

(2) $M_\infty = 0.491$, Re# = 2.378×10^6

α_W	α_T	$\Delta\theta$	$(C_L)_T$	$(C_m)_T$	% Separated Flow Upper	Lower
6	-8	-14	-0.3600	0.0556*	--	--
8	-6	-14	-0.1828	0.0276	0.0%	9.9%
10	-4	-14	-0.0019	-0.0026	0.0%	3.9%
12	-2	-14	0.1855	-0.0343	0.0%	0.0%
6	-5	-11	-0.1643	0.0206	--	--
8	-3	-11	0.0206	-0.0108	0.0%	0.0%
10	-1	-11	0.2076	-0.0436	0.0%	0.0%
12	+1	-11	0.3975	-0.0767	1.1%	0.0%
6	-2	-8	0.0338	-0.0164	--	--
8	0	-8	0.2191	-0.0488	0.0%	0.0%
10	+2	-8	0.4132	-0.0838	0.0%	1.5%
12	+4	-8	0.6188	-0.1226*	2.7%	0.0%

Table C.3: Predicted Compressible Lift and Pitching Moment for TIP 4

(1) $M_\infty = 0.70$, $Re\# = 3.390 \times 10^6$

α_W	α_T	$\Delta\theta$	$(C_L)_T$	$(C_{m_{0.25}})_T$	% Separated Flow Upper	Lower
0	-8	-8	-0.5104	0.0800*	0.0	6.21%
2	-6	-8	-0.3526	0.04721	0.0	3.55%
4	-4	-8	-0.1630	0.0142	0.0	3.47%
6	-2	-8	0.0454	-0.0210	--	--
0	-5	-5	-0.3562	0.0469*	0.0	2.96%
2	-3	-5	-0.1604	0.0125	0.0	1.89%
4	-1	-5	0.0536	-0.0251	0.0	0.0
6	+1	-5	0.3043	-0.0633*	--	--
0	-2	-2	-0.1601	0.0116	0.0	0.91%
2	0	-2	0.0564	-0.0269	0.0	0.0
4	+2	-2	0.3093	-0.0656*	1.6%	0.0
6	+4	-2	0.5595	-0.1052*	--	--

(2) $M_\infty = 0.491$, $Re\# = 2.378 \times 10^6$

α_W	α_T	$\Delta\theta$	$(C_L)_T$	$(C_m)_T$	% Separated Flow Upper	Lower
6	-8	-14	-0.3556	0.0419*	--	--
8	-6	-14	-0.18452	0.0200*	0.0	12.1%
10	-4	-14	-0.0008	-0.0058*	0.0	0.0
12	-2	-14	0.1755	-0.0300*	0.0	0.0
6	-5	-11	-0.1675	0.0145*	--	--
8	-3	-11	0.0132	-0.0108	0.0	0.0
10	-1	-11	0.1993	-0.0385	0.0	0.0
12	+1	-11	0.3881	-0.0669	0.0	0.0
6	-2	-8	0.0324	-0.0173	--	--
8	0	-8	0.2189	-0.0455	0.0	0.0
10	+2	-8	0.4127	-0.0758	0.0	0.0
12	+4	-8	0.6198	-0.1095	0.99%	0.0

Table C.4: Predicted Compressible Lift and Pitching Moment for TIP 6

(1) $M_\infty = 0.70$, Re# = 3.390×10^6

α_W	α_T	$\Delta\theta$	$(C_L)_T$	$(C_{m_{0.25}})_T$	% Separated Flow Upper	% Separated Flow Lower
0	-8	-8	-0.5069	0.0715*	0.0%	2.0%
2	-6	-8	-0.3514	0.0409	0.0%	1.0%
4	-4	-8	-0.1614	0.0096	0.0%	0.0%
6	-2	-8	0.0445	-0.0225	--	--
0	-5	-5	-0.3537	0.0407*	0.0%	0.8%
2	-3	-5	-0.1586	0.0085	0.0%	0.0%
4	-1	-5	0.0516	-0.0254	0.0%	0.0%
6	+1	-5	0.2986	-0.0592*	--	--
0	-2	-2	-0.1575	0.0080	0.0%	0.0%
2	0	-2	0.0546	-0.0267	0.0%	0.0%
4	+2	-2	0.3050	-0.0612	0.0%	0.0%
6	+4	-2	0.5521	-0.0969*	--	--

(2) $M_\infty = 0.491$, Re# = 2.378×10^6

α_W	α_T	$\Delta\theta$	$(C_L)_T$	$(C_m)_T$	% Separated Flow Upper	% Separated Flow Lower
6	-8	-14	-0.3561	0.0352*	--	--
8	-6	-14	-0.1867	0.0153*	0.0%	0.0%
10	-4	-14	-0.0057	-0.0093*	0.0%	0.0%
12	-2	-14	0.1726	-0.0296*	0.0%	0.0%
6	-5	-11	-0.1666	0.0095*	--	--
8	-3	-11	0.0137	-0.0132	0.0%	0.0%
10	-1	-11	0.1966	-0.0375	0.0%	0.0%
12	+1	-11	0.3800	-0.0617	0.0%	0.0%
6	-2	-8	0.0296	-0.0179	--	--
8	0	-8	0.2189	-0.0444	0.0%	0.0%
10	+2	-8	0.4075	-0.0706	0.0%	0.0%
12	+4	-8	0.6076	-0.0995*	0.0%	0.0%

NASA
National Aeronautics and Space Administration

Report Documentation Page

1. Report No.	2. Government Accession No.	3. Recipient's Catalog No.
NASA CR 177487		

4. Title and Subtitle	5. Report Date
VSAERO Analysis of Tip Planforms for the Free-Tip Rotor	June 1988
	6. Performing Organization Code

7. Author(s)	8. Performing Organization Report No.
Daniel M. Martin Paul E. Fortin	
	10. Work Unit No.

9. Performing Organization Name and Address	11. Contract or Grant No.
The University of Kansas Center for Research, Inc. Lawrence, KS	NCC 2-175
	13. Type of Report and Period Covered
12. Sponsoring Agency Name and Address	Contractor Report
National Aeronautics and Space Administration Washington, DC 20546	14. Sponsoring Agency Code

15. Supplementary Notes

Point of contact: R. H. Stroub, NASA Ames Research Center, M/S T-031
Moffett Field, CA 94035
(415) 694-6732
FTS 464-6732

16. Abstract

This report presents the results of a numerical analysis of two interacting lifting surfaces separated in the spanwise direction by a narrow gap. The configuration consists of a semispan wing with the last 32% of the span structurally separated from the inboard section. The angle of attack of the outboard section is set independently from that of the inboard section. In the present study, the three-dimensional panel code VSAERO is used to perform the analysis. Computed values of tip surface lift and pitching moment coefficients are correlated with experimental data to determine the proper approach to model the gap region between the surfaces. Pitching moment data for various tip planforms are also presented to show how the variation of tip pitching moment with angle of attack may be increased easily in incompressible flow. It is also shown that the induced drag of the tip surface is reduced for negative incidence angles relative to the inboard section. The results indicate that this local drag reduction overcomes the associated increase in wing induced drag at high wing lift coefficients.

17. Key Words (Suggested by Author(s))	18. Distribution Statement
Free-Tip Rotor VSAERO semispan wing induced drag	Unlimited Subject Category: 02

19. Security Classif. (of this report)	20. Security Classif. (of this page)	21. No. of pages	22. Price
Unclassified	Unclassified	124	A06

PREPARATION OF THE REPORT DOCUMENTATION PAGE

The last page of a report facing the third cover is the Report Documentation Page, RDP. Information presented on this page is used in announcing and cataloging reports as well as preparing the cover and title page. Thus it is important that the information be correct. Instructions for filling in each block of the form are as follows:

Block 1. Report No. NASA report series number, if preassigned.

Block 2. Government Accession No. Leave blank.

Block 3. Recipient's Catalog No. Reserved for use by each report recipient.

Block 4. Title and Subtitle. Typed in caps and lower case with dash or period separating subtitle from title.

Block 5. Report Date. Approximate month and year the report will be published.

Block 6. Performing Organization Code. Leave blank.

Block 7. Author(s). Provide full names exactly as they are to appear on the title page. If applicable, the word editor should follow a name.

Block 8. Performing Organization Report No. NASA installation report control number and, if desired, the non-NASA performing organization report control number.

Block 9. Performing Organization Name and Address. Provide affiliation (NASA program office, NASA installation, or contractor name) of authors.

Block 10. Work Unit No. Provide Research and Technology Objectives and Plans (RTOP) number.

Block 11. Contract or Grant No. Provide when applicable.

Block 12. Sponsoring Agency Name and Address. National Aeronautics and Space Administration, Washington, D.C. 20546-0001. If contractor report, add NASA installation or HQ program office.

Block 13. Type of Report and Period Covered. NASA formal report series; for Contractor Report also list type (interim, final) and period covered when applicable.

Block 14. Sponsoring Agency Code. Leave blank.

Block 15. Supplementary Notes. Information not included elsewhere: affiliation of authors if additional space is required for block 9, notice of work sponsored by another agency, monitor of contract, information about supplements (film, data tapes, etc.), meeting site and date for presented papers, journal to which an article has been submitted, note of a report made from a thesis, appendix by author other than shown in block 7.

Block 16. Abstract. The abstract should be informative rather than descriptive and should state the objectives of the investigation, the methods employed (e.g., simulation, experiment, or remote sensing), the results obtained, and the conclusions reached.

Block 17. Key Words. Identifying words or phrases to be used in cataloging the report.

Block 18. Distribution Statement. Indicate whether report is available to public or not. If not to be controlled, use "Unclassified-Unlimited." If controlled availability is required, list the category approved on the Document Availability Authorization Form (see NHB 2200.2, Form FF427). Also specify subject category (see "Table of Contents" in a current issue of STAR), in which report is to be distributed.

Block 19. Security Classification (of this report). Self-explanatory.

Block 20. Security Classification (of this page). Self-explanatory.

Block 21. No. of Pages. Count front matter pages beginning with iii, text pages including internal blank pages, and the RDP, but not the title page or the back of the title page.

Block 22. Price Code. If block 18 shows "Unclassified-Unlimited," provide the NTIS price code (see "NTIS Price Schedules" in a current issue of STAR) and at the bottom of the form add either "For sale by the National Technical Information Service, Springfield, VA 22161-2171" or "For sale by the Superintendent of Documents, U.S. Government Printing Office, Washington, DC 20402-0001," whichever is appropriate.